Optical gain and modal loss in AlGaN based deep UV lasers

vorgelegt von
Diplom-Physiker

Martin Georg Rudolf Martens

geb. in Berlin

von der Fakultät II - Mathematik und Naturwissenschaften
der Technischen Universität Berlin
zur Erlangung des akademischen Grades
Doktor der Naturwissenschaften
(Dr. rer. nat.)
genehmigte Dissertation

Promotionsausschuss:

Vorsitzender:	Prof. Dr. Michael Lehmann
Gutachter:	Prof. Dr. Michael Kneissl
Gutachter:	Prof. Dr. Russell D. Dupuis

Tag der wissenschaftlichen Aussprache: 2. März 2018

Berlin 2018

Contents

Chapter 1

Introduction

Recent progress in the fabrication of efficient deep ultraviolet (UV) light emitting diodes (LED) has encouraged research groups around the world putting tremendous effort into pushing the emission wavelengths of semiconductor based laser diodes further into the UV spectral region. The experiences gained from the development of (In)GaN based laser diodes for emission in the UVA to visible spectral range, which is ongoing since the first demonstration of a III-nitride based laser diode by Nakamura and coworkers in 1996 emitting at 417 nm [1], can be considered as an ideal basis for the exploration of new frontiers. Nowadays, highly efficient InGaN based laser diodes with low laser thresholds and high output powers are commercially available in wide spectral emission range.
This work deals with the scientific and technological challenges, which have to be faced before realizing deep UV lasing from semiconductor based laser diodes. In order to reach the target emission wavelength of sub-300 nm the AlGaN alloy system is the ideal candidate as it covers almost the entire UVA to UVC spectral range depending on the material composition. Along with the use of the AlGaN material as active region of deep UV lasers, however, new questions concerning optical and electrical issues as well as device fabrication techniques arise. This study provides a detailed analysis of the optical gain and loss processes in AlGaN active regions and gives an answer to the question of whether the AlGaN material system is suitable for the realization of current injection deep UV laser diodes.
This chapter provides a brief introduction to this work. First a motivation for the development of deep UV laser diodes is given before the state of the art is discussed. Last the outline of the work is introduced.

1.1 Motivation

Deep UV semiconductor laser diodes are of great interest for a wide range of applications including medical diagnostics, gas sensing, biochemical agent detection and materials processing [2–5]. The use of the AlGaN alloy system for the active region

allows to tailor the emission wavelength of the device for the target application. In terms of beam quality, spectral pureness and power density laser diodes are superior to LEDs and therefore preferable for numerous applications. Additionally, laser diodes have significant advantages compared to currently available UV laser sources like excimer lasers and frequency multiplied semiconductor lasers: Laser diodes are small, have considerably low power demands, and are robust. The fabrication of semiconductor wafers is scalable, which limits fabrication costs making those devices extremely interesting from a commercial point of view. Since processing techniques for InGaN based laser diodes emitting in the visible and UVA spectral range are well investigated and manageable in large scale, it can also be expected that this knowledge is somewhat transferable to the production of AlGaN based deep UV lasers, boosting further development and launching industrial production.

1.2 State of the art of AlGaN based UV laser diodes

Fig. 1.1 shows a collection of laser threshold current densities reported for UV laser diodes [6]. Several III-nitride based laser diodes have been demonstrated emitting in the UVA spectral region utilizing InGaN, AlGaN or InAlGaN quantum well (QW) active regions. In 2008 Yoshida and coworkers reported a record short wavelength of 336 nm at room temperature for current injection lasing from AlGaN QWs [7]. The threshold current density was 17.6 kA/cm^2 in pulsed operation (10 ns, 5 kHz), which is considerably higher compared to laser diodes emitting at 400 nm or longer (see

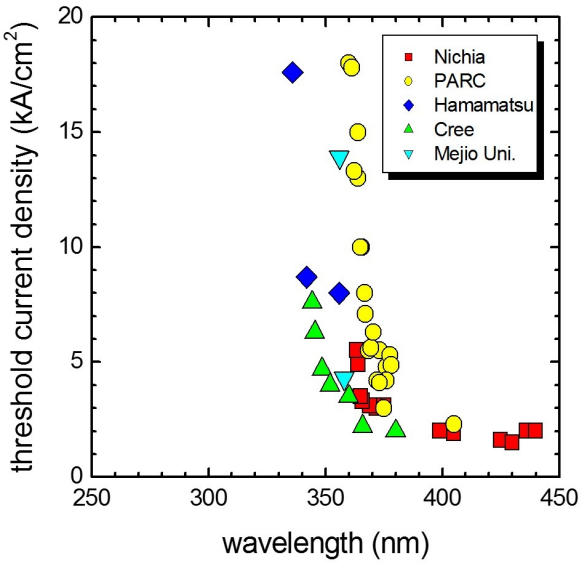

Figure 1.1 Threshold current densities of UV laser diodes published in recent years. [6]

Fig. 1.1). In 2015 Yoshida et al. presented an even shorter wavelength of 326 nm [8], which, however, has not been published yet. On the other hand, recently several optically pumped lasers pseudomorphically grown on AlN with emission wavelengths down to 237 nm were reported [9, 10]. However, low p-side conductivity and poor current injection efficiencies in combination with limited modal gain and elevated cavity losses still hinder the development of current injection laser diodes in the deep UV spectral range.

1.3 Outline of this work

This work guides through the development of UV laser diodes from crystal growth to heterostructure design to current injection. Each step is based on the previous one, but still addressed individually. A physical analysis with respect to the influence of the different issues on the laser performance is conducted leading to suggestions for further progress.

Chapter 2 introduces experimental methods used in this work for fabrication and optical characterization of deep UV lasers. Crystal growth, formation of laser cavities and basic luminescence characteristics of AlGaN based optically pumped lasers are discussed. The used setups for optical pumping experiments as well as the analysis methods are described. Additionally, absorption processes and the influence of the excitation wavelength in optical pumping experiments are discussed.

Based on this, chapter 3 addresses material quality related aspects. The influence of the threading dislocation density as well as the surface morphology and luminescence homogeneity on laser threshold and internal losses of optically pumped lasers are discussed. In this context, bulk AlN substrates, planar AlN/sapphire templates and defect reduced epitaxially laterally overgrown (ELO) AlN/sapphire templates for growth of AlGaN MQW laser heterostructures are compared. As ELO process can trigger specific morphology features like V-pit formation and step bunching, those influences on the optically pumped laser threshold are discussed. The presented results show that the defect density and the morphology of the semiconductor crystal have a major effect on the threshold.

Chapter 4 focuses on the heterostructure design. Effects of composition and design parameters of the active region, emission wavelengths, and the optical polarization of the spontaneous as well as laser emission of the present deep UV optically pumped lasers for different wavelengths are discussed. It is shown that the use of AlGaN based multiple quantum well active regions embedded in an $Al_xGa_{1-x}N/Al_yGa_{1-y}N$ separate confinement heterostructure can provide sufficient material gain as well as

optical confinement in order to achieve optically pumped lasing.
Finally, in chapter 5, the suitability of these results for current injection in high optical confinement heterostructures is discussed. For the high carrier densities necessary to reach transparency condition and eventually lasing, highly conductive n- as well as p-AlGaN layers with high aluminum mole fractions are needed. This, however, is due to the large ionization energies especially for magnesium acceptors in AlGaN with high aluminum mole fractions a critical issue. One approach suggested in literature to overcome the high activation energy is to use AlGaN short period super lattices (SPSLs) instead of single thick AlGaN layers. The suitability of this approach for current injection in high optical confinement heterostructures is discussed. Furthermore, the influence of magnesium acceptors on optical losses in AlGaN based waveguide structures for deep UV lasing is addressed. By quantifying the magnesium absorption it is possible to perform reliable calculations of modal losses in deep UV separate confinement heterostructures and suggest heterostructure designs which combine high optical confinement, high modal gain, and efficient carrier injection.

Chapter 2

Optical pumping of AlGaN multiple quantum well lasers

This chapter focuses on experimental aspects of the optical characterization of deep UV lasers. As the electrical injection of carriers into the AlGaN MQW active region is challenging, e.g. due to high ionization energies of available dopants for high Al content AlGaN or the difficulties of realizing ohmic contacts (see chapter 5), it is desirable to investigate the suitability of AlGaN based MQW active regions for UV lasing independently from electrical issues. By optical excitation carriers can be directly generated within the semiconductor material without the necessity of introducing doping or metal contacts to the heterostructure. In section 2.1 the fabrication including the crystal growth and the formation of laser cavities of AlGaN based optically pumped lasers is discussed. Additionally, basic luminescence characteristics will be discussed. For the optical characterization of the optically pumped lasers an experimental setup was designed and installed in order to determine the laser threshold and optical gain characteristics. The setups as well as the analysis methods are introduced in section 2.2 before absorption processes and the influence of the excitation wavelength is discussed at last in this chapter.

2.1 Fabrication of optically pumped lasers

Compared to current injection laser diodes optically pumped lasers require a rather simple heterostructure design and limited processing steps. As the carriers are photogenerated within the semiconductor layers, doping or metal contacts for current injection are not necessary. The heterostructure has to be designed to provide electrical and optical confinement as well. For the prior a potential profile has to be created which forces the carriers into a well defined region, in order to reach high carrier densities. For this, the fact can be used, that the band gap energy of $Al_xGa_{1-x}N$ depends on the material composition, as shown in Fig. 2.1(a). With increasing Al content the band gap energy of the ternary semiconductor increases. This allows to form a multiple quantum well (MQW) active region where carriers are well confined

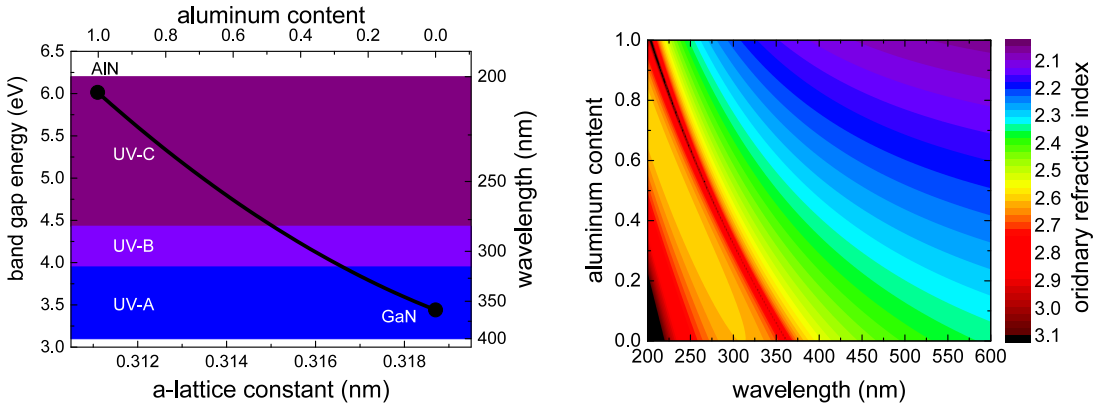

(a) band gap energy (b) refractive index

Figure 2.1 Calculated band gap energy of $Al_xGa_{1-x}N$ for different Al contents (bowing parameter $b = 1\,eV$)(a) and ordinary refractive indices for different wavelengths calculated according to a model by [11] with experimental data from [12–14]).

within the QWs due to the potential barrier to the quantum barriers formed by AlGaN layers with higher Al content compared to the QWs. Consequently, the AlGaN layers building the QWs need to have the lowest Al content of all AlGaN layers in the laser heterostructure.

As the band gap energy of $Al_xGa_{1-x}N$ increases with increasing Al content, the refractive index decreases for a given wavelength longer than the wavelength corresponding to the band gap energy of the AlGaN layer (see Fig. 2.1(b)). This can be used to design a waveguiding structure which confines the optical mode to the MQW active region where amplification can take place, as the optical mode tends to propagate in the layer with highest refractive index [15]. While for high efficiencies the carriers need to be confined in comparably thin layers in the range of a few nanometers (see section 4.2.2), the optical mode is best confined in a waveguide with thickness in range of the wavelength. Therefore, the carriers are confined to different layers than the optical mode. An example for such a separate confinement heterostructure (SCH) designed for laser emission of 270 nm is shown in Fig. 2.2. The heterostructure consists of an $Al_xGa_{1-x}N/Al_{0.70}Ga_{0.30}N$ MQW active region, $Al_{0.70}Ga_{0.30}N$ waveguide layers, and a lower $Al_{0.80}Ga_{0.20}N$ cladding layer. The middle graph in Fig. 2.2 shows the band gap energy profile of the SCH with values from Fig. 2.1(a). It needs to be mentioned, that this is a simplified schematic with the interpolated band gap energies of relaxed bulk layers and a band offset of 70:30 (conduction to valance band) [16] without any internal nor external fields considered. However, it clearly illustrates the idea of carrier confinement within the MQW active region. The carriers tend to accu-

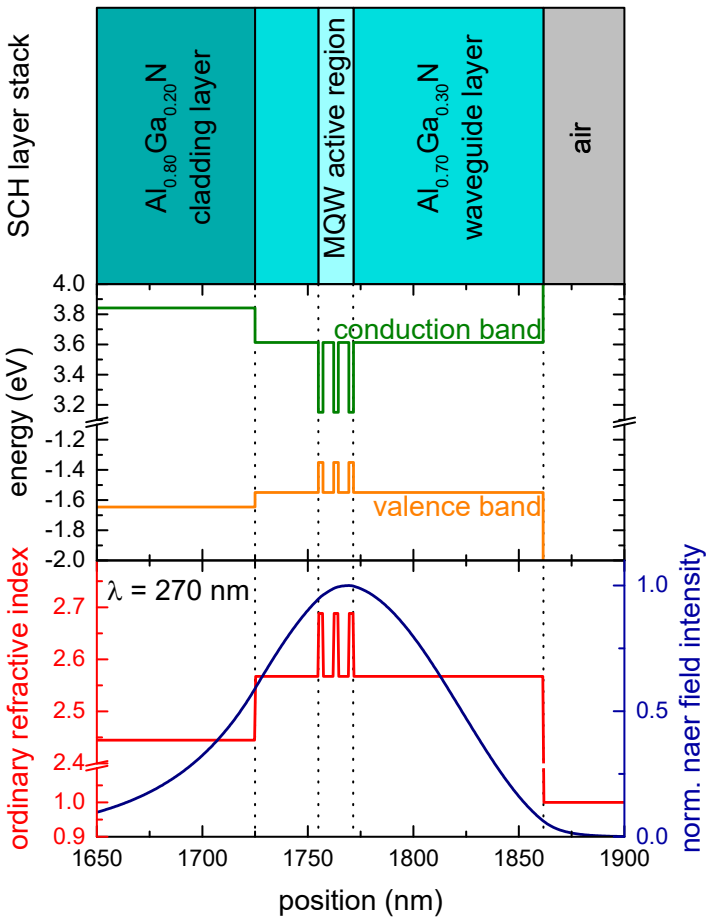

Figure 2.2 Schematic of the layer stack, simplified band gap energy profile, and refractive index profile as well as calculated mode distribution of an optically pumped SCH design for 270 nm laser emission.

mulate in the QWs as they present potential minima within the heterostructure. This applies to carriers photogenerated in QWs and photogenerated in the surrounding layers eventually relaxing into the QWs in case of optically pumped laser as well as to carriers injected through n- or p-side, respectively in case of current injection laser diodes.

The bottom graph in Fig. 2.2 shows the refractive index profile as well as the calculated optical mode of the laser heterostructure. All calculations of the mode distribution in this work were performed using the commercial simulation software SiLENSe [17]. The optical mode is confined within the waveguide layers which have a higher refractive index compared to the cladding below and the surrounding atmosphere ($n \approx 1$). The higher the refractive index contrast between the waveguide layers and the surrounding media, the better the mode is confined to the waveguide. Therefore, the MQW active region is asymmetrically positioned within the waveguide as the refractive index contrast to the air on top is higher than the contrast to the $Al_{0.80}Ga_{0.20}N$ cladding layer on the bottom and the mode peak is shifted towards the bottom cladding. As a re-

sult the positions of the mode maximum and QWs match quite well, which eventually leads to optimized amplification of the laser mode.

2.1.1 Pseudomorphic growth of laser heterostructures by MOVPE

There are different methods available for epitaxial growth of the III-nitride semiconductor crystals used for opto electronic devices (e.g. metal organic vapor phase epitaxy (MOVPE), molecular beam epitaxy (MBE), hybrid vapor phase epitaxy (HVPE), physical vapor transport (PVT)). The laser heterostructures discussed in this work are grown by MOVPE as this method combines advantages like excellent material quality and high throughput. By this method layer thickness can be controlled down to monolayer scale. This way layer stacks with high precision in terms of layer thickness and material composition can be produced. In this process the group-III precursors Trimethylgallium (TMGa) and Trimethylalluminum (TMAl) as well as Ammonia (NH_3) as nitrogen source are led into the reactor, where the precursors are thermally decomposed and the material is deposited by chemical reactions on the hot substrate. The growth process can be controlled by changing gas flow rates, pressure and temperature. As carrier gas nitrogen or hydrogen is used. For implementing the n- (Si) and p-doping (Mg) silane (SiH_4) and cyclopentadienylmagnesium (Cp_2Mg) are used, respectively. Detailed information about the crystal growth by MOVPE can be found elsewhere [18–20]

All laser heterostructures discussed here are grown in [0001] direction on either sapphire or free standing AlN substrates at TU Berlin (Thomas Swan CCS MOVPE reactor) or at the Ferdinand-Braun-Institut, Leibniz-Institut für Höchstfrequenztechnik (Aix2400G3HT). The choice of substrate can influence the morphology of the heterostructure inter- and surfaces as well as the defect density. The influence of those parameters on the laser performance is discussed in chapter 3. Independent of the choice of substrate the laser heterostructure is deposited on relaxed AlN layers. The large lattice mismatch between the $Al_xGa_{1-x}N$ of the laser heterostructure and the underlying AlN (compare Fig. 2.1(a)) results in compressive strain within the heterostructures' layers. When the strain increases with decreasing Al content it may be reduced by strain relaxation. This, however, may result in generation of dislocations and consequently high non radiative recombination rates [21]. Therefore, in order to produce highly efficient, low threshold lasers, the epitaxial layers need be pseudomorphically grown to the underlying AlN, which limits the thickness and the compositional range used for the laser heterostructure design. Fig. 2.3 shows x-ray diffraction reciprocal space maps of the 10.5 reflex of optically pumped MQW laser heterostructures designed for $\sim$ 270 nm emission with an $Al_{0.80}Ga_{0.20}N$ cladding layer and different

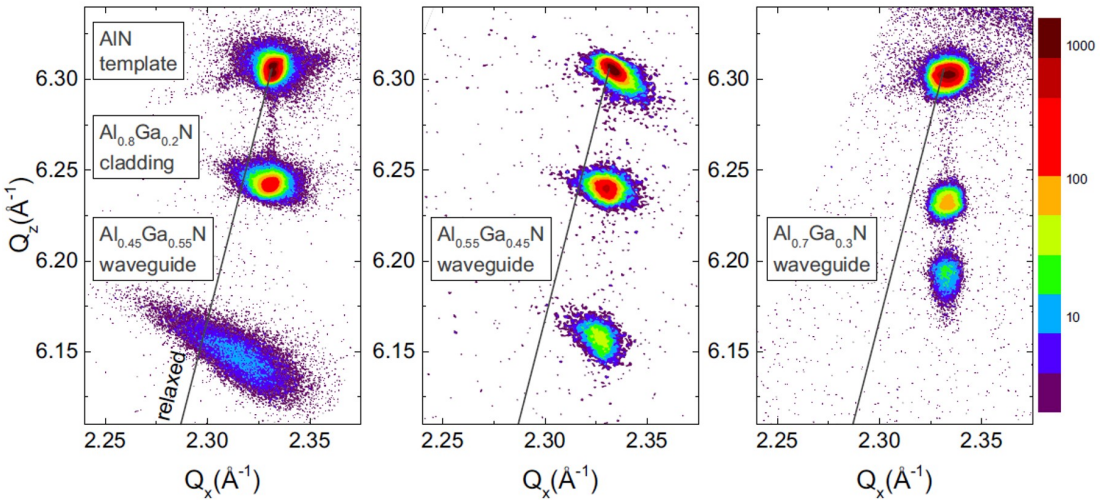

Figure 2.3 Reciprocal space maps of optically pumped laser heterostructures with a threefold $Al_{0.42}Ga_{0.58}N$ MQW active region, $Al_{0.80}Ga_{0.20}N$ cladding layers and $Al_xGa_{1-x}N$ quantum barriers and waveguide layers with different composition. (measurement by C. Kuhn (TU Berlin) [22])

Al contents in the $Al_xGa_{1-x}N$ waveguide layer ranging from 45 % to 70 %. As the lattice constant and the dislocation density in the strained layers can vary for different substrates, the state of relaxation may also depend on the choice of substrate. The data shown here is obtained from heterostructures grown on defect reduced epitaxially laterally overgrown (ELO) AlN/sapphire templates (see section 3.1). The 1 µm $Al_{0.80}Ga_{0.20}N$ cladding is psudomorphically strained in all laser heterostructures. This is clearly illustrated by the fact that in the reciprocal space maps in Fig. 2.3 the diffraction peak of this layer is at the same Q_x position as the one of the relaxed AlN layer indicating that the a-lattice constants are identical. The signal resulting from the 30 nm thick lower and 85 nm thick upper $Al_{0.45}Ga_{0.55}N$ waveguide layer is slightly shifted to smaller Q_x values, which is a result from relaxation setting in. The theoretical position of completely relaxed $Al_xGa_{1-x}N$ layers is marked by the diagonal line originating from the center of the AlN diffraction peak. The $Al_{0.45}Ga_{0.55}N$ peak also exhibits a strong broadening indicating an increased defect density or other mechanisms of inhomogeneous relaxation [22]. Also the peak of the $Al_{0.55}Ga_{0.45}N$ waveguide layers of the same thickness (middle graph in Fig. 2.3) is partially relaxed despite the larger Al content and resulting lower lattice mismatch. Only for heterostructure with the $Al_{0.70}Ga_{0.30}N$ waveguide layers the compressive strain is small enough that the layers of the total thickness of 115 nm do not relax, as derived from the identical Q_x position of the corresponding diffraction peaks in the reciprocal space map in Fig. 2.3. Therefore, this AlGaN composition and layer thickness represent a lower and upper

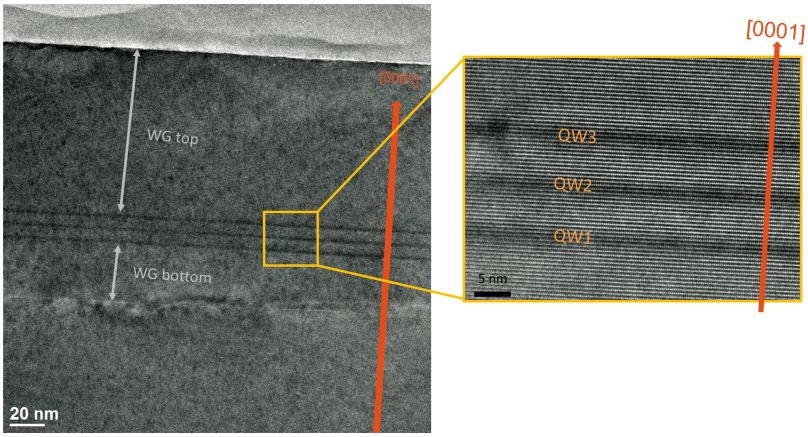

Figure 2.4 TEM image of a pseudomorphically strained optically pumped laser heterostructure with $Al_{0.80}Ga_{0.20}N$ cladding cladding and $Al_{0.70}Ga_{0.30}N$ waveguide layers. (measurement by J. Park (TU Berlin))

limit, respectively, for heterostructures with moderate dislocation densities. However, as shown above this SCH design can provide mode and carrier confinement.
Fig. 2.4 shows transmission electron microscopy (TEM) images in cross section of an optically pumped laser heterostructure with a threefold $Al_{0.42}Ga_{0.58}N/Al_{0.70}Ga_{0.30}N$ MQW active region, an $Al_{0.80}Ga_{0.20}N$ cladding layer and $Al_{0.70}Ga_{0.30}N$ waveguide layers pseudomorphically grown on ELO AlN/sapphire substrate. The heterostructure exhibits smooth and homogeneous interfaces. Also the well defined QWs are visible with homogenous thickness of 2.4 nm $\pm$ 0.4 nm which matches the target thickness of 2.2 nm.

2.1.2 Fabrication of laser cavities on sapphire and AlN substrate

For laser operation resonator mirrors are required. In case of edge emitting semiconductor based laser diodes the crystal facets can be used as resonator mirror. For normal incident the reflectivity of the crystal facet is according to the Fresnel equation given by the difference of effective refractive index of the laser mode propagating in the semiconductor crystal (n_{eff}) and the refractive index of the surrounding air ($n_{air} = 1$):

$$R = \left(\frac{n_{eff} - n_{air}}{n_{eff} + n_{air}}\right)^2 = \left(\frac{n_{eff} - 1}{n_{eff} + 1}\right)^2 \tag{2.1}$$

The portion of light transmitted through the crystal facets is lost for amplification. The so called mirror losses α_m for a given cavity length of l can be described by

$$\alpha_m = -\frac{1}{L} ln\left(\frac{1}{R}\right). \tag{2.2}$$

The calculated reflectivity of uncoated facets of laser heterostructure emitting in the deep UV spectral range is $\sim$ 0.18 (n_{eff} $\sim$2.5). This translates into mirror

losses of - 17 cm^{-1} for a cavity length of 1 mm. The calculated reflectivity of 0.18, however, can only be reached for high quality smooth facets. Once steps or any other roughness is present light scattering can significantly lower the reflectivity, which results in increased mirror losses and consequently increased laser threshold.

In order to obtain smooth crystal facets the as grown wafers are laser scribed with a commercial laser work station [23–25]. By this method smooth resonator facets with roughnesses of less than 2 nm were obtained for GaN based laser diodes grown on sapphire substrates [23]. The system uses a frequency-tripled Nd:YAG laser with an wavelength of 355 nm and 5 ns pulse length. The beam is focused onto the backside of the substrate. The UV irradiation is absorbed by mutliphonon processes and a groove is formed by evaporation in the substrate as shown in the microscope image in Fig. 2.5. The depth of the groove can be controlled by the energy of the scribing laser or the scribing rate. The groove needs to be deep enough that the crystal can be easily broken along the scribed line in order to produce high reflective facets. On the other hand, if the groove is to close to the epitaxial layers, the laser heterostructure may be damaged resulting in poor device performance. A groove depth of 300 µm to 350 µm in the 430 µm thick sapphire substrate was found to be a suitable compromise. The laser scribing lines need to be precisely aligned along the a- or m-plane of the semiconductor crystal in order to obtain best results. In this work laser heterostructures grown on sapphire and freestanding AlN substrates are studied. However, only lasers grown on sapphire substrates are cleaved subsequent to prior laser scribing. In case of heterostructures grown on bulk AlN substrates the substrate was scribed manually with a diamond scriber into the substrate. As the crystal planes of the AlN substrate and the laser heterostructure are identical the material can be broken more easily than the sapphire substrate. This method can also produce highly reflective facets. However, there are ongoing studies on further improving the laser facets of lasers grown on bulk AlN substrates including laser scribing and thinning of

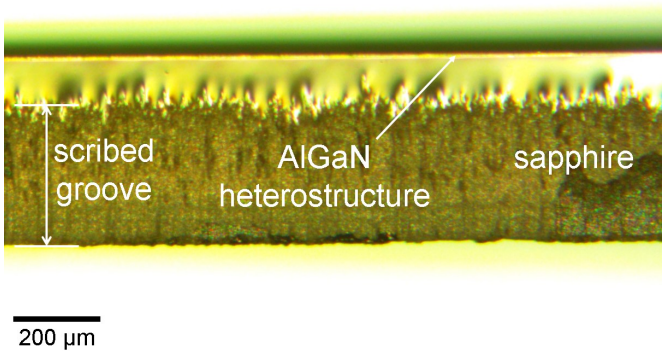

Figure 2.5 Opitcal microscope image of scribed laser bar facet. A 300 µm to 350 µm grove is scribed into the 430 µm thick sapphire substrate.

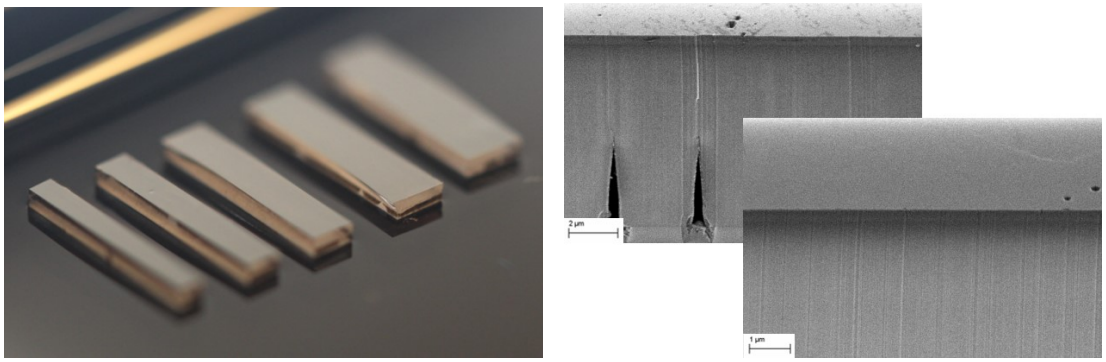

(a) photograph (b) SEM

Figure 2.6 Photograph of cleaved optically pumped deep UV laser bars with a length of 5 mm and widths of 600 µm, 800 µm, 1000 µm, 1200 µm, and 1400 µm (a). Scanning electron microscopy (SEM) images of cleaved facets parallel end perpendicular to the stripes of the ELO AlN/sapphire template (b)

the substrate.

Subsequent proper laser scribing the wafers can be easily broken by applying little mechanical pressure on the wafer surface directed in the vicinity of the scribed lines. Fig. 2.6(a) shows a photograph of cleaved optically pumped deep UV laser bars with a length of 5 mm and different widths between 600 µm and 1400 µm. The crystal facets of the long side of the laser bar is used as resonator mirrors. The laser bar width represents the cavity length.

The crystal facets of optically pumped lasers grown on ELO AlN/sapphire substrates are shown in the scanning electron microscopy (SEM) images in Fig. 2.6(b). As the image was taken with an inclined angle in respect to the facet, the crystal facet as well as the crystal surface can be seen. The left SEM image shows resonator mirrors cleaved along the a-direction forming an m-plane facet. Clearly visible are the trenches edged into the sapphire substrate for the ELO process and the voids before coalescence resulting from the subsequent lateral growth (compare section 3.1). The right image shows an a-plane facet aligned along the ELO pattern. Both facets exhibit high quality and reflectance. However, some steps on the facet are present in both cases. On the m-plane facet steps tend to bundle at coalescence lines from the lateral overgrowth. Between those lines, however, smooth facet are obtained.

Two different designs for laser scribing of optically pumped lasers grown on quarters of 2-inch sapphire wafers were used (see Fig. 2.7). Both designs provide laser bars with a length of 5 mm and widths of 600 µm, 800 µm, 1000 µm, 1200 µm, and 1400 µm with resonator aligned along a- and m-direction. Using a first generation design 15 laser bars with description P1 to P15 and 20 bars with the description S1 to S10 and T1

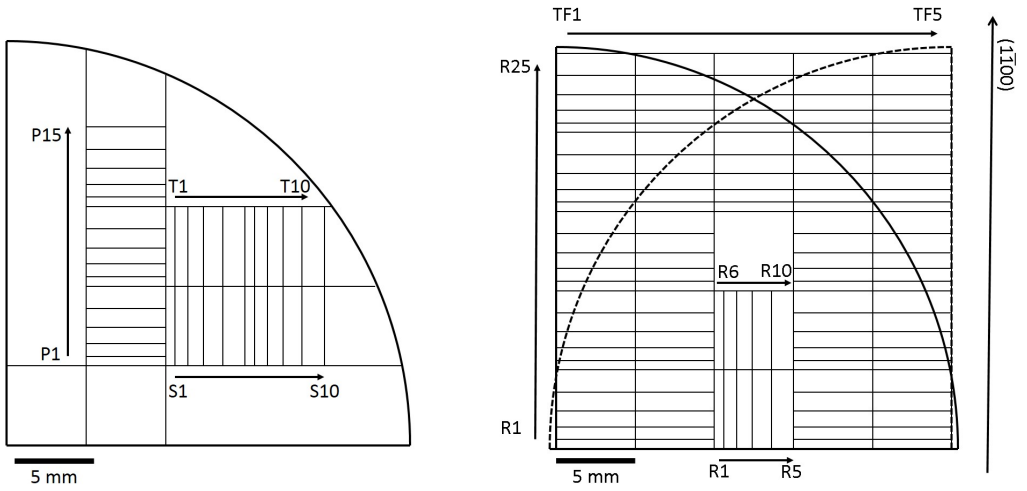

(a) generation 1 (b) generation 2

Figure 2.7 Designs for laser scribing of optically pumped laser heterostructures grown on a quarter of 2-inch wafers.

to T10 with resonator facet perpendicular to the one of the P set can be cleaved. For processing different quarters of the same wafer the design is rotated. Therefore, the orientation of laser bars in respect with the crystal planes depends on which quarter of the wafer is used. For the A and C quarter wafers the bars from the S and T set have m-plane mirror facets, for B and D quarters the P set has m-plane mirror facets. Since m-plane facets are expected to be more suitable as resonator mirrors as they can be more easily cleaved [23], a second generation laser scribing design was developed, which provides a larger number of laser bars with m-plane facets independent of the wafer quarter used. This design is shifted for processing different wafer quarter rather than rotated. As consequence the laser exhibit the same orientation in respect with the crystal planes. The laser can be identified by the number of column (TF1 to TF5) and the number of bar (R1 to R25). All laser bars except for the ones from TF3 have m-plane resonator mirrors. Additionally, a 5 mm by 5 mm wafer piece from the center of the quarter wafer is available for additional material characterization. As the design is shifted for different quarters the position of the laser bar with respect to the 2-inch wafer varies, e.g. the laser bar TF1R1 is either positioned right at the center of the 2-inch wafer or at the wafer edge. The description of the laser bar is either laser scribed in the backside of the substrate or marked by metalization on the surface of the heterostructure.

2.1.3 Luminescence characteristics and homogeneity

The different laser scribing designs used to fabricate optically pumped lasers provide laser bars from different regions of the wafer. This allows to investigate the dependence of the laser performance on its position. The heterostructure itself is expected to exhibit inhomogeneities throughout the wafer. This can result from different incorporation of atoms onto the semiconductor surfaces due to morpholigic fluctuations. This kind of inhomogeneity is in µm scale and sub-µm scale and will be discussed in section 3.2. Additional to the micsocopic fluctuation macroscopic variations throughout the wafer have to be taken into account, which can be observed in larger scale. The origin of those fluctuation can be found in variations of growth parameters along the wafers. Slight variation in gas flows or growth temperature can result in altered Ga or Al incorporation or different growth rates which affects the thickness of the epitaxial layers.

Fig. 2.8 shows room temperature photoluminescence (PL) maps of an optically pumped laser grown on a quarter of a 2-inch ELO AlN/sapphire wafer. The heterostructure consists of a threefold 1.1 nm $Al_{0.47}Ga_{0.53}N$ / 5 nm $Al_{0.70}Ga_{0.30}N$ MQW active region embedded in an $Al_{0.70}Ga_{0.30}N/Al_{0.80}Ga_{0.20}N$ mode guiding structure. For the PL map spectra from different spots on the wafer with a distance of 500 µm were taken with an 193 nm ArF excimer laser as excitation source. Each spectrum was analyzed to provide a peak wavelength of the QW emission and an integrated peak intensity. In Fig. 2.8(a) the maps for the peak wavelength of the MQW emission is shown. A clear wavelength shift towards longer wavelength from the quarter wafer tip to the wafer edge can be observed. This shift covers about 8 nm. However, a

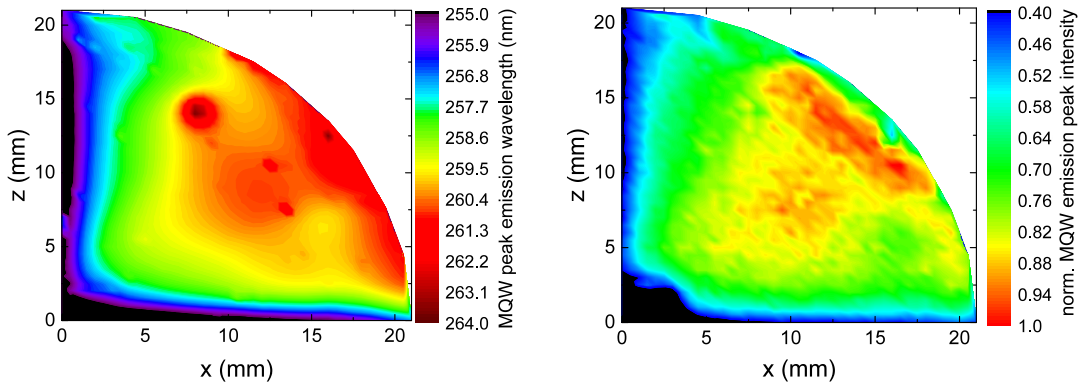

(a) MQW emission wavelength

(b) MQW emission intensity

Figure 2.8 Room temperature photoluminescence (PL) emission maps of an optically pumped laser heterostructure grown on a quarter of a 2-inch ELO AlN/sapphire wafer (measurement by C. Reich (TU Berlin)).

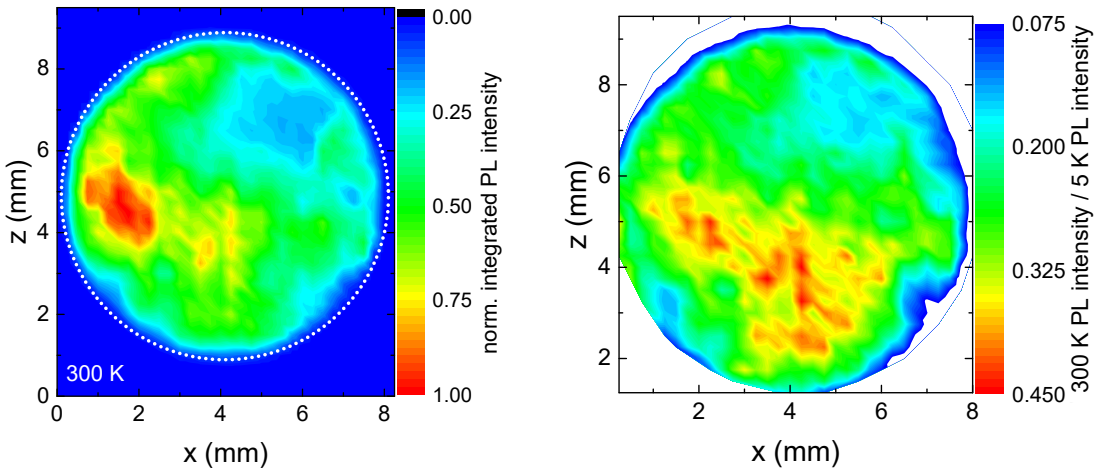

(a) PL intensity (b) IQE

Figure 2.9 Photoluminescence (PL) emission maps of an optically pumped laser heterostructure grown on a quarter of a freestanding AlN wafer with a diameter of 8 mm (measurement by C. Reich (TU Berlin)).

center region of the wafer of about 10 mm by 10 mm shows quite stable emission of $\sim 260.5\,\text{nm} \pm 0.5\,\text{nm}$. The integrated PL peak intensity shows a similar behavior as the wavelengths (see Fig. 2.8(b)). The intensity increases by a factor of two from spots near the quarter wafer tip to the wafer edge. However, in the region where homogenous wavelengths distribution is observed also high relative intensity is obtained. In Fig. 2.9(a) the PL intensity map of an optically pumped laser grown on a bulk AlN substrate with a diameter of 8 mm is shown. For this map PL spectra with a spacing of 250 µm were measured and analyzed. The dotted round line marks the edges of the wafer. Contrary to the laser heterostructure grown ELO AlN/sapphire discussed above, this structure contains a threefold 2.2 nm $Al_{0.47}Ga_{0.53}N$ / 5 nm $Al_{0.70}Ga_{0.30}N$ MQW active region while the mode guiding structure is the same. At the extreme edges the intensity dramatically drops which is attributed to edge effects during growth or PL measurements. The intensity distribution on the wafer is quite inhomogeneous. A region with comparably high intensity can be seen on the left of the image where intensity increases by a factor of two within less than 1 mm spacing while a region in the upper right of the wafer exhibits a strong drop of intensity. For this laser heterostructure a low temperature (5 K) PL map was acquired additionally. This allows to compare room temperature and low temperature PL intensity and estimate the internal quantum efficiency (IQE) (Fig. 2.9(b)), which provides a quantitative value for the efficiency of radiative recombination. The regions with high IQE do not completely match the regions with high room temperature intensity, which may be

attributed to different light extraction due to morphologic variations. The region on the left side of the wafer with high intensity exhibits also high IQE of more than 0.3. However, also a region with high IQE can be found where room temperature intensity is significantly lower (bottom part). The region with low room temperature intensity on the upper right side also exhibits the lowest IQE of ~ 0.15.
The presented measurements show that laser heterostructures grown on sapphire as well as bulk AlN substrate exhibit wavelength and intensity variations along the wafer in mm-scale. This fact needs to be considered when comparing results from different wafers. Additionally, fluctuation in sub mm-scale, which can also not be excluded, may affect the characterization of the lasers, when wavelength or intensity varies within the excited cavity region.

2.2 Optical excitation in stripe geometry

For the characterization of the AlGaN based deep UV lasers an experimental setup was designed and established at TU Berlin, which provides different characterization methods, especially optical gain spectroscopy by variable stripe length method (see section 2.2.1), laser threshold measurements (section 2.2.2) and optical polarization selective spectroscopy (section 2.2.3). The produced results can either be used to gain deeper understanding of the physical processes in deep UV MQW lasers or for feedback within an optimization circle targeting the development of efficient deep UV laser diodes. As explained in the previous sections the laser heterostructures can provide vertical mode guiding by the waveguide and cladding layer and therefore defines the cavity dimension in growth direction. The cavity length is defined by the cleaved crystal facets acting as resonator mirrors and therefore by the laser bar width. The vertical cavity dimensions needs to be defined by the excitation source. In case of current injection laser diodes this can be done by the the metal contact and optional additional ridge etching defining the current path and consequently the pumped volume. For optical excitation this can be done by realizing a well defined excitation stripe (Fig. 2.10). The excitation laser beam is shaped into stripe geometry and focused onto the semiconductor surface covering the complete cavity length from facet to facet. The excitation volume can then be well controlled by the width of the excitation stripe. The emission extracted through either facet can be collected and analyzed.
In order to obtain reliable results from the optical pumping experiments the excitation needs to be as homogenous as possible, i.e. the optical power density needs to be constant throughout the excitation area. This means that the excitation stripe needs

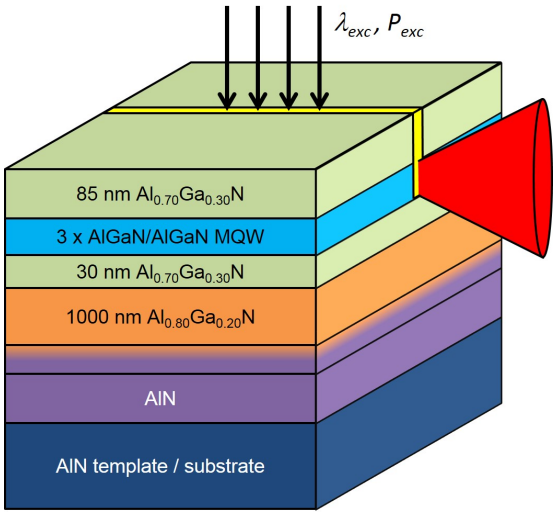

Figure 2.10 Schematic of optical excitation for laser characterization.

to be well defined and homogeneous. Additionally, as a one-dimensional approach is applied to determine the optical gain, the excitation stripe needs to be thin. Since no suitable excitation laser with those beam characteristics is available, this is a technical challenge. Therefore the excitation laser beam shaping is first addressed in this section before the used measurement methods are explained.

As excitation source an ArF excimer laser with a wavelength of 193 nm, a pulse width of 5 ns and repetition rates up to 500 Hz is used. Pulse energies up to 5 mJ can be used, which corresponds to an optical power of 1 MW in one pulse and an averaged optical power of 2.5 W for the highest available duty cycle. The beam profile of the ArF laser in a distance of 400 mm is shown in Fig. 2.11. The beam has a rectangular shaped profile with a full width at half maximum (FWHM) of $\sim$2 mm in horizontal and $\sim$6 mm in vertical direction with strong inhomogeneities in horizontal direction.

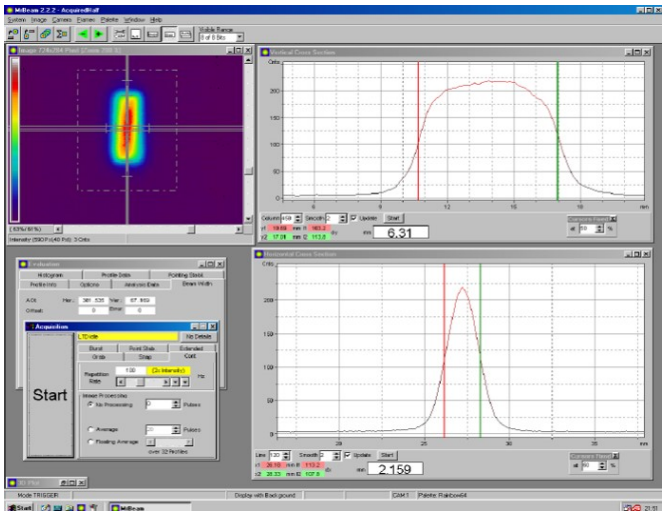

Figure 2.11 Beam profile of the ArF excimer laser in a distance of 400 mm used for optical excitation [26].

Therefore, the beam is expanded by a factor of ten using a diverging ($f = -50\,\text{mm}$) and a converging ($f = 500\,\text{mm}$) lens. A 11 mm by 15 mm aperture is used to extract the flat top of the extended beam and form a rectangular shaped excitation spot with homogeneous power distribution and sharp edges. In order to obtain a thin excitation stripe this parallel beam is focused by a cylindrical lens ($f = 300\,\text{mm}$) in vertical direction as shown in Fig. 2.12. The resulting stripe is imaged onto the sample by an additional converging lens ($f = 75\,\text{mm}$) with a ratio of $\sim$10:3. The stripe length can be controlled by a motorized slit, which is positioned between both lenses. Since the stripe at one side needs to be positioned right at the facet of the sample from which the emission is collected the length of the stripe is only varied at one side. Therefore, one edge of the slit is kept constant while the opposite edge is moved. This way the length of excitation on the sample can be varied, which can be used to determine the optical gain by the variable stripe length method (VSLM) (see section 2.2.1).
The power distribution within the excitation stripe was tested by moving an additional blade into the beam path. The pulse energy is measured between the slit and the imaging lens for different excitation areas (see Fig. 2.13). The pulse energy increases linearly with increasing area. This clearly illustrates the homogeneous power distribution with the excitation spot in the dimension of the stripe (y direction). This allows homogenous pumping along the entire cavity length and ensures reliable optically pumped laser threshold power densities (see section 2.2.2). The power distribution vertical to the stripe direction (z direction) was not tested, as the sample is positioned

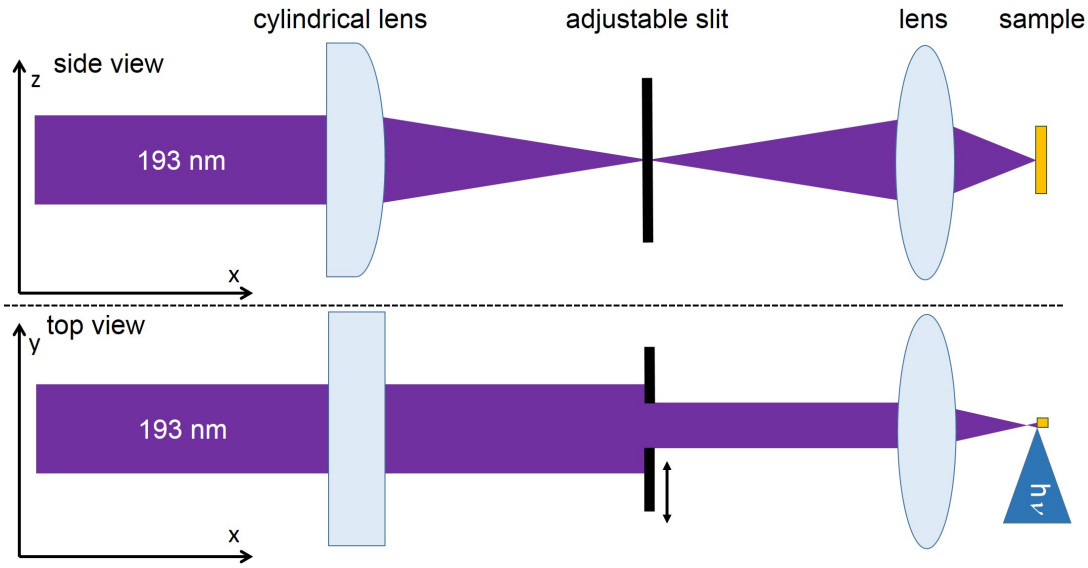

Figure 2.12 Schematic of the beam shaping for optical excitation in stripe geometry in side view (top) and top view (bottom).

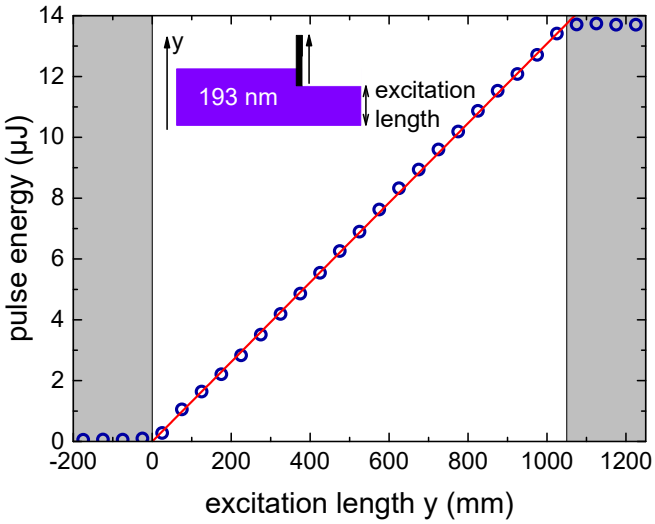

Figure 2.13 Pulse energy in dependence of the stripe length.

in the focal point of this dimension. Therefore, the entire power distributed within the z direction is bundled and the power density within the stripe is homogeneous independent of the power distribution along the z direction in the excitation area.
The stripe shape and dimensions are frequently checked by burning the excitation stripe into a 100 nm thick gold coating deposited on a silicon wafer at the position of the sample (see Fig. 2.14). The left image shows 1.5 mm long stripes for different x positions, i.e. varying focal distance between imaging lens and sample. The variation of x position is 10 µm between each stripe. The shape of and the power distribution in the stripe strongly depend on the position relative to the focal point of the imaging

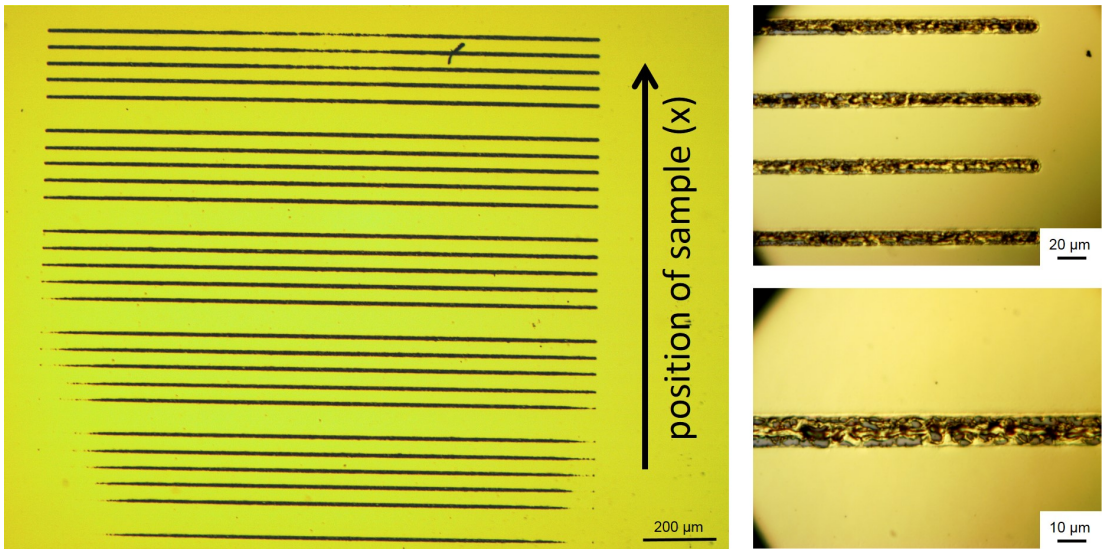

Figure 2.14 Optical microscope images of the excitation stripe burned into gold coated silicon wafers at the position of the sample.

lens. If the sample is not in focus of the last lens the stripe is not only widened but also diffuse in the center region (top set of stripes) or at the edges of the stripe (bottom sets of stripes). The second set of stripes, however, exhibits homogeneous power distribution, sharp edges and constant thickness. This can be clearly seen in the microscope images with larger magnification on the right hand side of Fig. 2.14. The stripe width was determined to be $\sim 15\,\mu m$. With the stripe dimension and the measured pulse energy the power density can then be easily calculated by:

$$P_{exc} = \frac{E_{pulse}}{\tau_{pulse} \cdot A_{exc}}. \tag{2.3}$$

E_{pulse} represents the measured pulse energy, τ_{pulse} the pulse width, which is in this case 5 ns, and A_{exc} the determined area of the excitation stripe. Depending on where the pulse energy is measured, the incident power density is additionally scaled by a factor of 0.876 due to absorption of the imaging lens. Reflection of the excitation laser on the crystal surface is not taken into account. Therefore, the numbers for optical excitation discussed in this work represent the power incident on the crystal surface and not the power penetrating the laser heterostructure.
Fig. 2.15 shows a schematic of the experimental setup for characterization of opti-

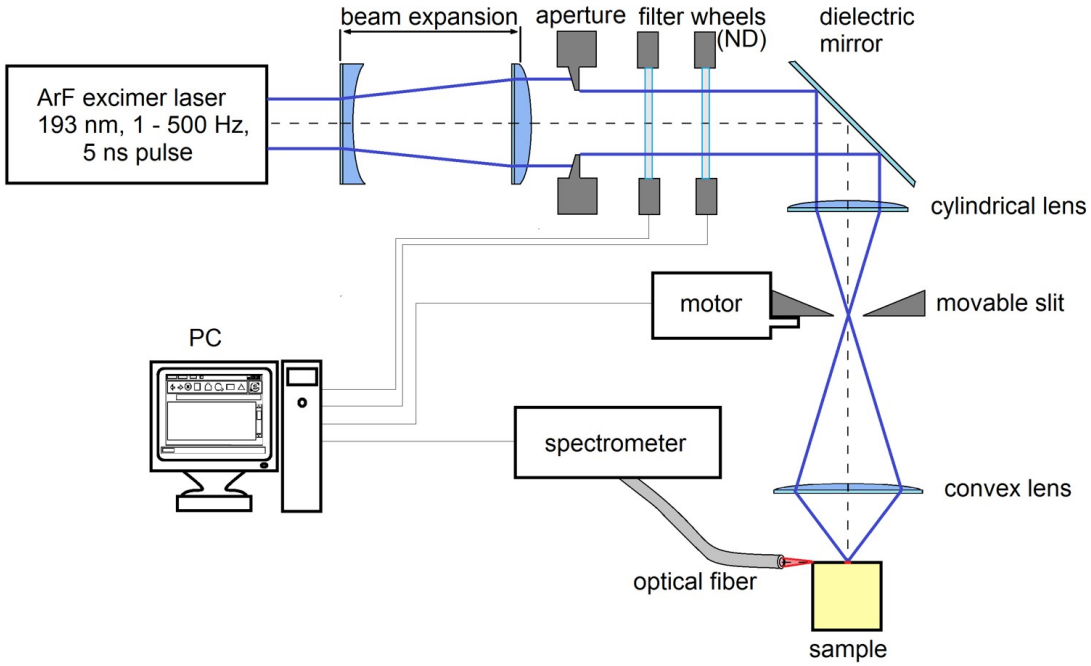

Figure 2.15 Schematic of the setup used for optical pumping of AlGaN based deep UV lasers. The pulse energy is usually measured between the slit and imaging lens and scaled by a factor of 0.876 taking into account the absorption of the lens.

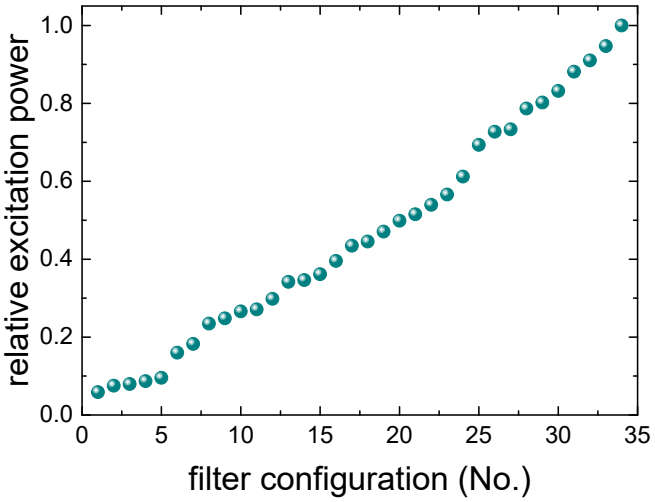

Figure 2.16 Relative excitation power varied by choosing different neutral density filter combinations.

cally pumped deep UV lasers. The MQW emission from the sample is collected by an optical fiber and analyzed by a spectrometer. In order to be able to vary the excitation power in larger range two filter wheels equipped with neutral density filters are installed. Each filter wheel provides six positions. This allows to attenuate the excitation power from the laser in 36 steps by combining both filter wheels. Ten neutral density filters with nominal optical densities ranging from OD = 0.04 to OD = 0.9 were used. One position each is not equipped with a filter. This leads to a combined maximum attenuation of OD = 1.4, which translates into a nominal transmission of $\sim 4\,\%$. Since the nominal optical density of the filters is given for the visible spectrum the filters are individually calibrated in the setup to determine the actual transmission of the each filter combination for the excitation wavelength of 193 nm. The calibration is frequently checked in order to include possible degradation of the optical elements due to the high energy and power of the excitation laser used. Fig. 2.16 shows the measured transmission of the filter combinations for 193 nm, which are commonly used in the experiment. Additionally, filter combinations are available providing optical densities of ~ 1.5 and ~ 1.7. Those, however, are usually not used since the step to the previous powers is comparably large. As initial pulse energy exiting the ArF excimer laser values in the range between 1 mJ and 3 mJ are preferred, which is a reasonable compromise between pulse stability and moderate operation voltage of the laser tube. By this excitation power densities of up to 50 MW/cm^2 incident on the sample can be reliably used. A repetition rate of 50 Hz was found to be favorable for the stability of the laser sample and usually provides enough signal.

2.2.1 Optical gain by variable stripe length method

The optical gain describes the amplification of photons within a material. Considering amplification of a one dimensional light beam within the material without additional losses one refers to the material gain. The amplification of an initial light intensity I_0 in dependence of the traveled path x can then be described by

$$I(x) = I_0 e^{g_{mat} \cdot x} \tag{2.4}$$

equivalent to Lambert-Beer's law for absorption with the absorption coefficient α. The material gain is a fundamental material property which depends on the photon energy of the amplified photons and the carrier density. However, in MQW based lasers the QWs act as active medium. Since the field intensity in the laser is confined into a mode propagating within the waveguide, only a small portion of the optical mode overlaps with the QWs and can eventually be amplified by the material gain of the QWs. Therefore, the material gain is scaled by the confinement factor Γ, which gives the spatial overlap of the optical mode with the QWs. This results in the modal gain:

$$g_{mod} = \Gamma \cdot g_{mat} \tag{2.5}$$

Additionally, internal losses α_{int}, originating from e.g. scattering processes or parasitic absorption of the light, can counteract the material gain resulting in a net gain, which can be experimentally observed:

$$g_{net} = \Gamma \cdot g_{mat} - \alpha_{int} = g_{mod} - \alpha_{int} \tag{2.6}$$

When the modal gain is greater than the internal losses, i.e. the net gain is positive, the mode is amplified by the material. This can be observed by an exponential increase of emission power with increasing pumping power. Fig. 2.17(a) shows the integrated MQW emission extracted through the facet from an optically pumped laser structure for emission at 270 nm. In this case not the complete cavity is pumped in order to inhibit lasing (see section 2.2.2). In the pumping regime shown the exponential increase of the emission can be clearly observed. Once the threshold condition of $g_{net} = 0$ is reached, amplified spontaneous emission (ASE) becomes the dominant process. The ASE threshold can be defined by the crossing of linear fits applied to the regions below and above threshold. The transition to ASE has also an effect on the emission spectra. Fig. 2.17(b) shows emission spectra for excitation below and above the ASE threshold. The ASE peak is with a FWHM of 2.8 nm significantly narrower than the emission peak below threshold.

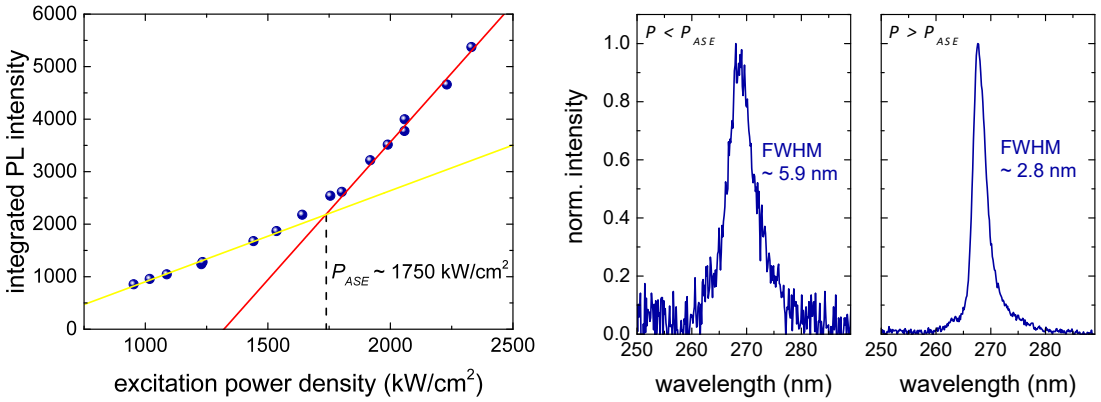

(a) ASE threshold (b) spectra

Figure 2.17 Integrated emission from the facet in dependance of excitation power density (a) and spectra below and above ASE threshold (b).

The optical gain of optically pumped structures can be derived from the variable stripe length method (VSLM) [27]. This method uses the fact, that the intensity extracted from a gain medium depends on the length as well as the gain of the medium (compare equation 2.4). In case of optical pumping of semiconductors the dimensions of the gain medium can be very well defined by the geometry of the optical excitation. Therefore, by altering the length of the excitation stripe on the semiconductor surface the length of the gain medium is varied. Fig. 2.18(a) shows emission spectra in the

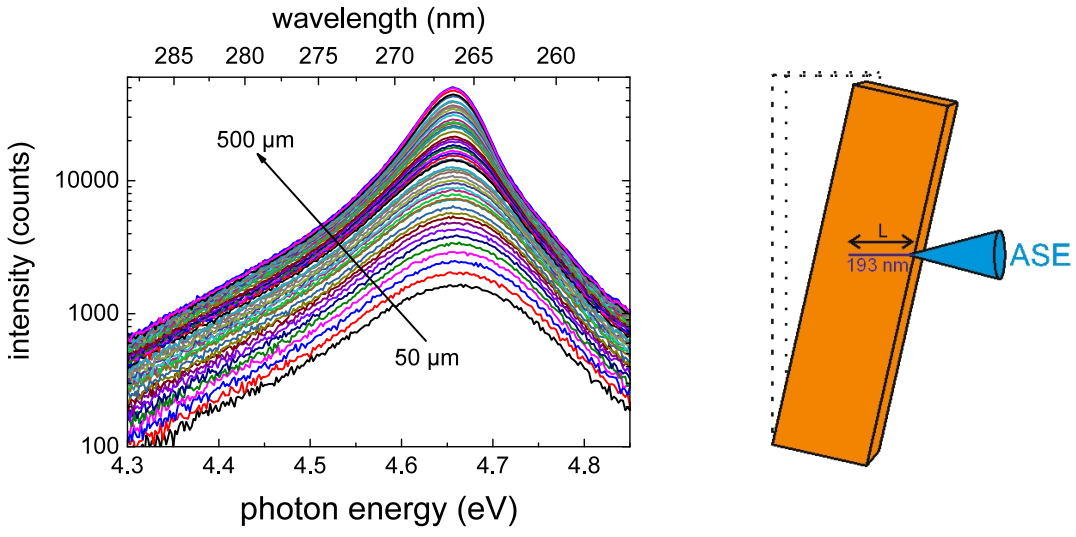

(a) emission (b) excitation geometry

Figure 2.18 Emission spectra collected from the facet of an optically pumped laser for different excitation stripe lengths ranging from 50 µm and 500 µm (a) and schematic of the excitation geometry used for VSLM experiments (b).

range of the ASE threshold from the facet of an optically pumped AlGaN MQW based laser with emission between 265 nm and 270 nm for different excitation stripe lengths ranging from 50 µm and 500 µm. The emission is collected using an optical fiber positioned at the laser facet. In order to inhibit feedback from the reflective facet back into the cavity, which is not considered in the analysis used for determining the optical gain, the laser bar is slightly tilted in respect with the excitation stripe as depicted in the schematic in Fig. 2.18(b). Since the method can only be applied for one dimensional propagation of the optical mode, the width of excitation needs to be small compared to the length (compare section 2.2).
With increasing excitation stripe length the intensity of the emission increases, which can simply be attributed to an increase of the excitation volume and therefore larger number of electron hole pairs generated. However, the increase of intensity depends on the emission energy. While the intensity on the lower energy side seems to saturate with increasing stripe length, the increase at the peak energy seems rather to accelerate. This becomes obvious by simply comparing the peak shape of spectra with lowest and highest excitation stripe length. This effect can not be explained by the higher number of carriers and therefore higher number of radiative recombination processes, but by an energy sensitive amplification process. By analyzing the behavior of the intensity with increasing stripe length for each emission energy (i.e. each pixel of the CCD array used for data acquisition) it is possible to extract this energy dependent gain coefficient g_E. Fig. 2.19(a) shows the measured intensity in dependance of the stripe length for three different representative photon energies within the emission peak. The behavior of the emission intensity extracted through the facet of the excitation stripe length L can be described by the differential equation

$$\frac{dI_E(L)}{dL} = g_E(L)\, I_E(L) + J_{spon}\, \Omega\,, \tag{2.7}$$

with J_{spon} representing the spontaneous emission density and Ω the solid angle along the stripe [28]. If the gain coefficient is assumed to be independent of the stripe length, equation 2.7 can be solved by

$$I_E(L) = \frac{J_{spon}\, \Omega}{g_E} \left(e^{g_E\, L} - 1\right)\,. \tag{2.8}$$

The experimental data in Fig. 2.19(a) is fitted with equation 2.8 using $C = J_{spon}\, \Omega$ and g_E as fitting parameters. The topmost graph shows the intensity for emission energies in the range of the emission peak maximum. The intensity follows a clear exponential increase with increasing stripe length. This results in a gain coefficient

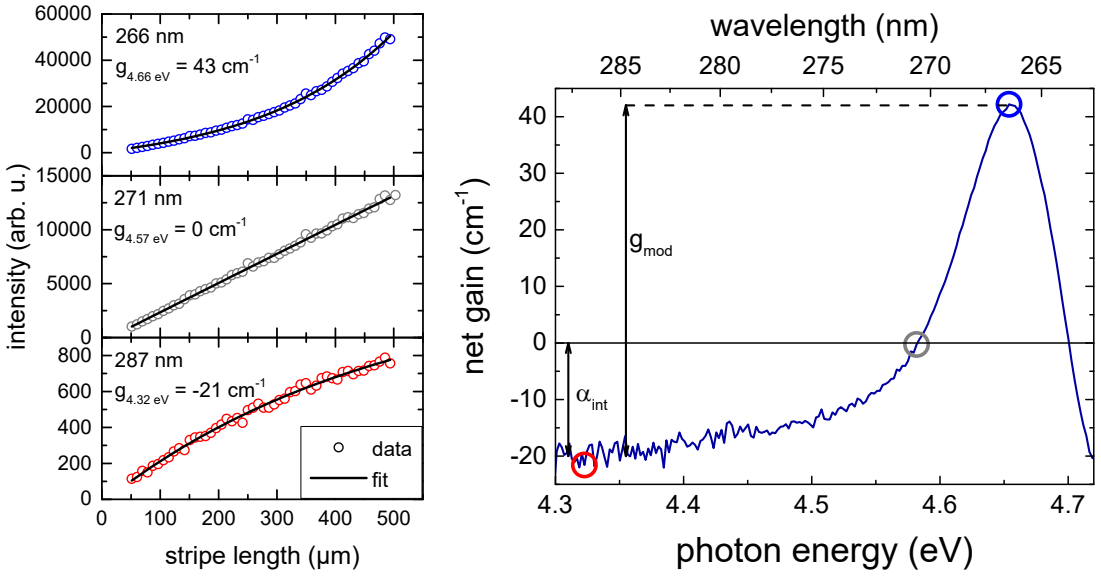

(a) gain fit (b) gain spectrum

Figure 2.19 Emission intensity in dependance of the excitation stripe length as well as the fit used to determine the gain coefficient for three different wavelengths (a) and gain spectrum of an optically pumped laser determined by the VSLM (b).

of 43 cm^{-1} for the corresponding photon energy. In the mid graph the intensity is plotted for lower energies. Here the intensity increases linearly with increasing stripe width, which corresponds to a gain coefficient of 0 cm^{-1}. For this energy the modal gain equals the internal losses. Consequently, the medium is transparent for photons with this energy. For even lower energies the intensity exhibits a saturation with increasing excitation length (see bottom graph in Fig. 2.19(a)), indicating that the optical mode is rather absorbed by the medium than amplified. The calculated gain coefficient is - 21 cm^{-1}. Following this procedure for each photon energy, a complete net gain spectrum can be derived (see Fig. 2.19(b)). The peak gain of more than 40 cm^{-1} is reached for photon energies in the range of 4.65 eV. For higher energies the gain rapidly drops below zero. This energy range corresponds to transitions of electrons and holes far beyond the band edge in the conduction band and valance band, respectively, where carrier populations are too low for positive gain and consequently band to band absorption is dominant. Moving to energies slightly below bandgap, which corresponds to transitions originating from tails of the conduction or valence band into the band gap, the net gain saturates at a value of $\sim$ - 20 cm^{-1}. As for this energy range the optical mode is assumed to be unaffected by band to band transition processes, this value represents the internal losses of the optical mode caused by e.g. mode scattering or parasitic absorption. The modal gain can then be

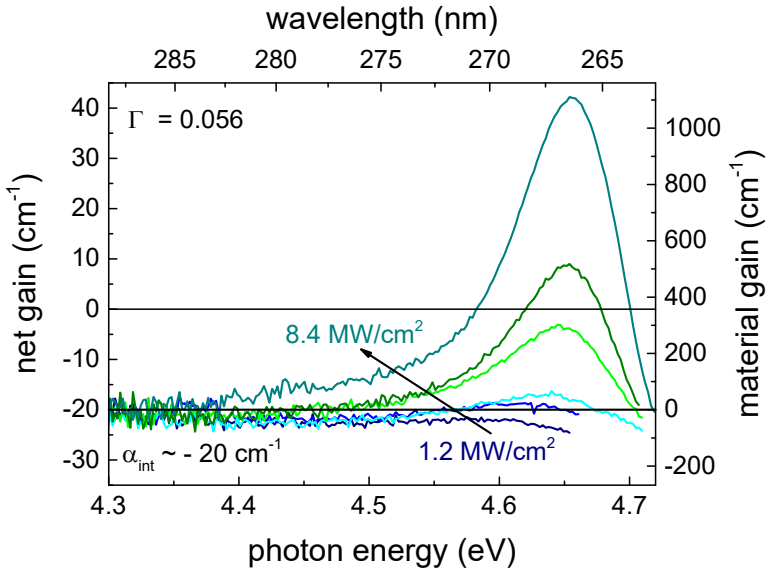

Figure 2.20 Gain spectra derived from the VSLM for different excitation power densities of an optically pumped laser.

understood as the gain from the internal losses taken as onset.

Fig. 2.20 shows gain spectra of the optically pumped laser for different excitation power densities around the ASE threshold. With the confinement factor Γ and the internal losses α_{int} the net gain determined by the VSLM can be translated into a material gain using equation 2.6. The confinement factor can be derived from numerical simulations of the optical mode and the internal losses are drawn from the gain spectra as discussed above. For the lowest excitation power density of 1.2 MW/cm^2 the gain does not exceed the value of the internal losses. With increasing excitation power a gain peak develops which eventually crosses transparency overcoming the internal losses. Also, the gain peak broadens spreading into higher energy regions. This illustrates the filling of higher energy states within the conduction and valence band with increasing number of excess carriers and shows the shift of the quasi Fermi level towards higher energies. Additionally, the gain peak shifts to higher energy, which can be attributed to band filling and screening of the quantum confined Stark effect (QCSE). For lower energies all gain spectra saturate at the level of the internal losses, as those are independent of the carrier density.

2.2.2 Optically pumped laser threshold

In order to determine the optically pumped laser threshold the emission spectra need to be measured in dependance of the excitation power density. For laser emission the complete cavity needs to be pumped. Therefore, an excitation stripe with the length of at least the laser bar width is required. Additionally, the excitation stripe needs to be carefully aligned perpendicular to the laser facets. During laser operation the

field oscillates in the cavity between the crystal facets used as resonator mirrors. The emission extracted through the facet is considered as additional loss of the system as it cannot participate to further amplification. Those mirror losses α_m depend on the cavity length and the reflectivity of the crystal facets. E.g. mirror losses of - 17 cm^{-1} can be calculated for a cavity length of 1 mm with uncoated facets for emission wavelength around 270 nm (compare section 2.1.2). Those losses have to be additionally compensated by the optical net gain in order to achieve lasing, which leads to the following laser threshold condition:

$$g_{net} + \alpha_m = 0 \tag{2.9}$$

Fig. 2.21 shows the emission spectra of an optically pumped laser for emission around 270 nm for different excitation power densities. For low excitation a comparably broad emission with rather low signal is detected. With increasing excitation power the signal significantly increases and a narrow emission line is formed indicating laser operation.

In order to determine the laser threshold power density the integrated peak intensity is plotted versus the excitation power density (Fig. 2.22(a)). For low excitation the integrated emission increases linearly. In this excitation regime spontaneous emission processes are dominant, which is consistent with the broad emission peak observed. At an excitation power density of $\sim$1.0 MW/cm^2 the linear increase turns into an exponential increase. In this region transparency condition is reached and ASE becomes dominant. Once the net gain is high enough to overcome the mirror losses the exponential increase eventually turns back into a linear increase. The dominant recombination process is then stimulated emission and the emission spectrum width is significantly reduced (0.8 nm at 268.6 nm as shown in the inset of Fig. 2.22(a)). The

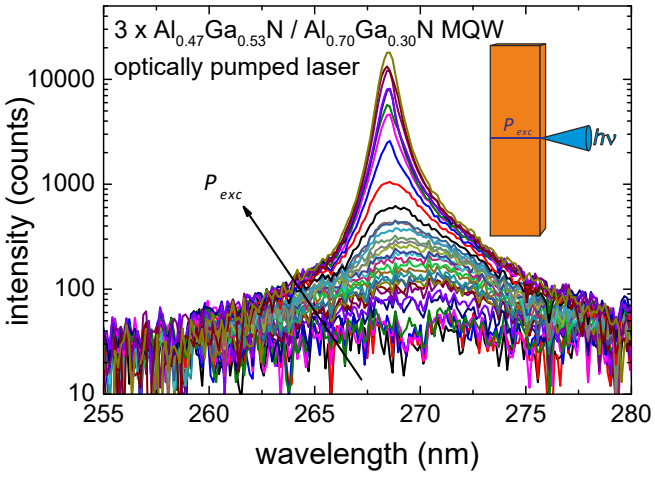

Figure 2.21 Emission spectra collected from the facet of an optically pumped deep UV laser for different excitation power densities. The excitation stripe is carefully aligned perpendicular to the laser facets and covers the entire cavity

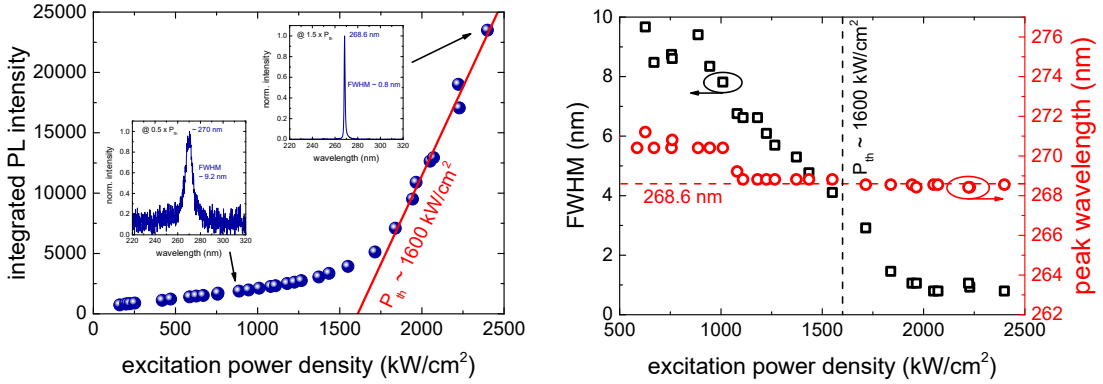

(a) integrated emission (b) FWHM and peak wavelength

Figure 2.22 Integrated emission (a) and FWHM as well as peak wavelength (b) of the emission from an optically pumped AlGaN based laser collected from the facet for different excitation power densities.

laser threshold power density of 1.6 MW/cm^2 is defined by the intersection point of a linear fit applied in the region of laser emission with the x-axis. The FWHM as well as the peak wavelength of the emission is plotted in Fig. 2.22(b) versus the pumping power density. For low excitation the FWHM is in the range of 9 nm. In the regime of ASE the FWHM continuously drops reaching the constant value in the range of 1 nm above the laser threshold. During laser operation the laser peak wavelength is constant at about 269 nm.

2.2.3 Optical polarization selective spectroscopy

In order to investigate the polarization of the MQW emission, polarization selective spectroscopy is performed. Analogously to the experiments described above the sample is excited in stripe geometry from top and emission from the facet is collected. As polarization selective element a Glan-Taylor prism is used. This, however, requires a parallel beam path of the analyzed emission, in order to obtain high polarization selectivity. Therefore, an additional collimating lens is positioned between crystal facet and polarizer as schematically shown in Fig. 2.23. The polarized signal is then focused by a second lens onto the facet of an optical fiber and analyzed by a grating monochromator. Two irises in the beam path ensure that only strongly parallelized emission is detected. The detected polarization can be altered by rotating the polarization prism.

Fig. 2.24(a) shows polarized spectra of an optically pumped laser heterostructure consisting of a threefold 2.2 nm $Al_{0.47}Ga_{0.53}N$ / 5 nm $Al_{0.70}Ga_{0.30}N$ MQW embedded in an $Al_{0.70}Ga_{0.80}N$ / $Al_{0.80}Ga_{0.20}N$ mode guiding structure for excitation below

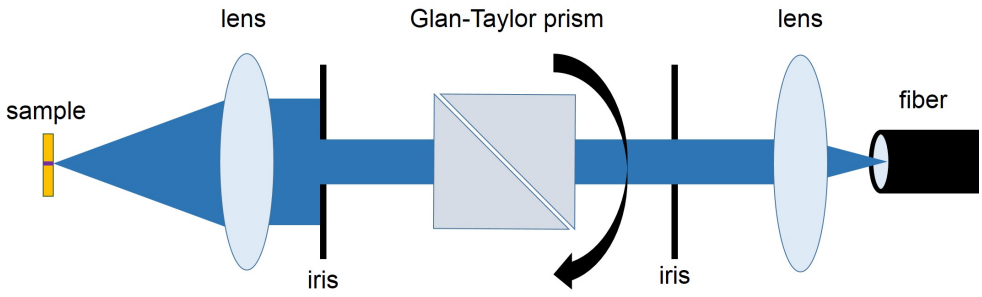

Figure 2.23 Schematic of the setup used for polarization dependent detection of emission from optically pumped lasers.

laser threshold. The transverse electric (TE) emission is inplane polarized and the transverse magnetic (TM) emission is polarized parallel to the c-axis of the crystal (see section 4.1). The emission peaks exhibit significant difference in intensity and a slight spectral shift depending on the polarization. The normalized integrated MQW emission peak in dependance of the polarization angle is shown in Fig. 2.24(b). The polarization angle is defined relative to the growth direction, i.e. TM polarization is at 0° , 180°, and 360° and TE polarization is at 90° and 270° polarization angle. The integrated intensity versus the polarization angle follows a clear sin^2 behavior as shown by the fit and is strongly symmetric. The degree of polarization can be determined by comparing the polarized signals. The polarization dependent spectra exemplary shown is strongly TE polarized with a degree of polarization of 0.74.

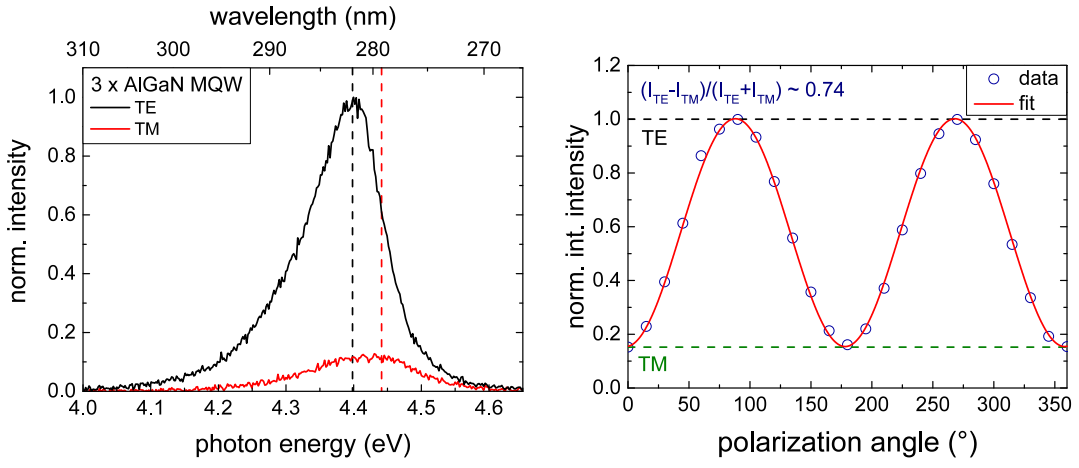

(a) polarization resolved spectra

(b) integrated intensity vs. polarization angle

Figure 2.24 Polarization resolved spectra (a) and integrated intensity in dependance of the polarization angle (b) of a threefold 2.2 nm $Al_{0.47}Ga_{0.53}N$ / 5 nm $Al_{0.70}Ga_{0.30}N$ MQW embedded in an $Al_{0.70}Ga_{0.80}N$ / $Al_{0.80}Ga_{0.20}N$ mode guiding structure.

2.3 Absorption and carrier transport into the active region

The incident excitation power density in optical pumping experiments cannot be easily translated into a carrier density in the active region as this depends on different aspects concerning the heterostructure design and material properties. The excitation wavelength of 193 nm is absorbed by all $Al_xGa_{1-x}N$ layers independent of the composition. Therefore, the highest number of carriers is generated in the topmost layers with an exponentially decreasing generation rate towards the active region. The initial depth distribution of carriers depends on the incident intensity and the absorption coefficient of the material. The carriers generated in the upper layers eventually relax into the MQW active region. The efficiency of this process is described by the excitation efficiency η_{exc}, which gives the number of carriers reaching the MQW by the total number of carriers photogenerated. This efficiency depends on the length of the path to travel by the carriers and therefore on the heterostructure design and the diffusion length of the carriers in the respective layers. The diffusion length is a material property and a function of the temperature. It is affected by the recombination rates in the material and the presence of scattering centers and therefore different for different material qualities (i.e. defect densities, interface roughness). As those issues cannot be easily evaluated, the excitation efficiency is rather understood as an empirical scaling factor than a calculated value.

The excitation pulse width is with 5 ns long compared to the expected carrier life time in the MQW. Therefore, the carrier density can be calculated by comparing the generation and the recombination rate. The carrier life time depends on defect densities, carrier densities and QW design issues like QW thickness, which may affect radiative recombination rates and can significantly vary for different structures. However, effective carrier life times of well less than 1 ns are expected for the investigated

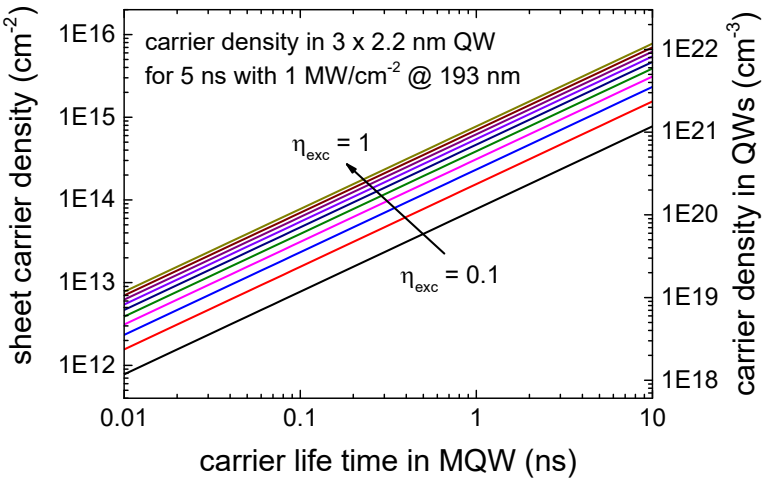

Figure 2.25 Calculated carrier density for 1 MW/cm^{-2} excitation at 193 nm of a threefold 2.2 nm MQW in dependance of the carrier life time in the QW for different excitation efficiencies η_{exc}.

emission wavelengths in the deep UV spectral range.
Fig. 2.25 shows the calculated carrier density for an excitation power density of 1 MW/cm^2 exemplary in a threefold MQW with a QW thickness of 2.2 nm in dependance of the carrier life time for different excitation efficiencies η_{exc} between 0.1 and 1. It is assumed that 80 % of the incident optical power penetrates the semiconductor taking into account the reflectivity of the crystal surface. This translates into a total photon number of $\sim 10^{12}$ and a photon density of $\sim 4 \cdot 10^{15}$ cm^{-2} penetrating the heterostructure per pulse. For the calculation it is assumed that each photon generates an electron hole pair.

2.4 Influence of excitation wavelength on optical pumping

Most spectroscopic data discussed in this work is obtained from optical pumping experiments using a 193 nm ArF excimer laser for excitation (see section 2.2). However, additionally experiments were performed using a 266 nm frequency quadrupled Nd:YAG laser with a pulse length of 5 ns and a repetition rate of 15 Hz as excitation source. The excitation beam is similarly formed as discussed for the ArF laser for excitation in stripe geometry and emission from the semiconductor facets. For different excitation wavelengths the generated carrier density can significantly vary. In case of optically pumped AlGaN based lasers the excitation of 193 nm is absorbed by the complete laser stack, especially in the topmost $Al_{0.70}Ga_{0.30}N$ waveguide layer which is commonly used for laser heterostructures with emission wavelengths below 300 nm. This layer as well as the cladding layer with higher Al content, however, is transparent for the excitation with 266 nm and the excitation laser power can depending on the QW composition only be absorbed by the QWs (resonant pumping). This drastically limits the absorption volume and therefore the number of generated carriers. Depending on the excitation efficient for 193 nm this can lead to significantly different carrier concentrations for the different excitation wavelengths.
In order to compare non resonant pumping with the different excitation wavelengths, the laser threshold of a violet optically pumped laser emitting at 405 nm is determined at each setup. The laser heterostructures consists of a threefold 3.5 nm $In_{0.06}Ga_{0.94}N$ / 7 nm $In_{0.01}Ga_{0.99}N$ MQW embedded in 75 nm $In_{0.03}Ga_{0.97}N$ / 75 nm GaN waveguide layers and a lower 1000 nm $Al_{0.07}Ga_{0.93}N$ cladding layer. The heterostructure is caped by a 20 nm thick $Al_{0.06}Ga_{0.94}N$ layer (see Fig. 2.26(a)). All layers of the heterostructure are absorptive for 193 nm and 266 nm as well. Fig. 2.27(a) shows the threshold power densities of different laser bars cleaved from the same wafer for the different excitation wavelengths. For excitation with 266 nm laser the threshold

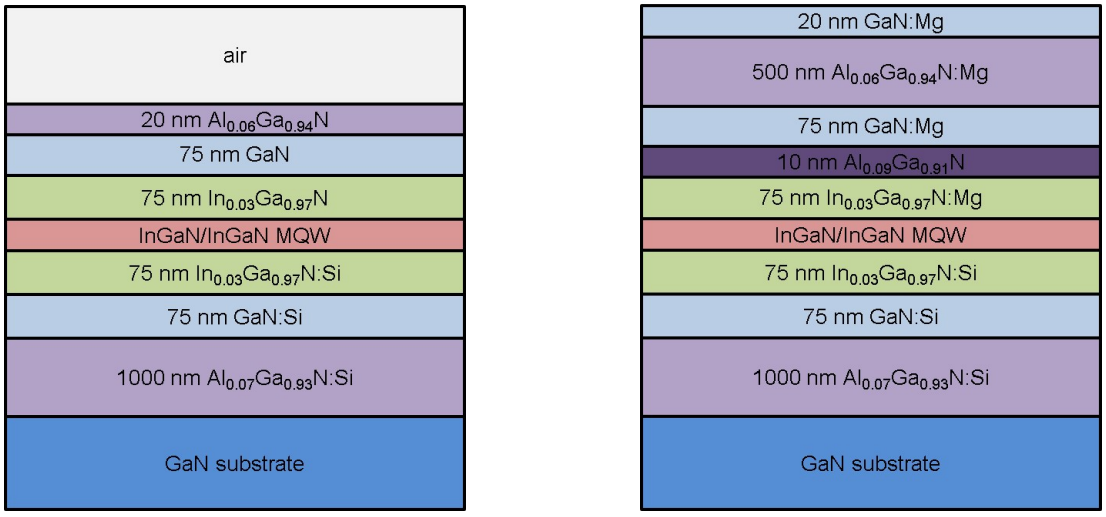

(a) 405 nm optically pumped laser (b) 405 nm laser diode

Figure 2.26 Schematic of the heterostructures of the optically pumped laser (a) and current injection laser diode (b) for 405 nm emission.

power density is quite constant at $\sim 100\,\mathrm{kW/cm^2}$. For excitation with 193 nm the laser threshold is increased by a factor of two to three and shows larger scattering. This instability may be attributed to the larger intensity instability of the 193 nm excimer laser compared to the solid state laser or possible degradation of the semiconductor for the high excitation energy. The increased laser threshold power density for the shorter excitation wavelength can partially be explained by the fact that for the same pulse power the number of photons is higher for lower photon energies,

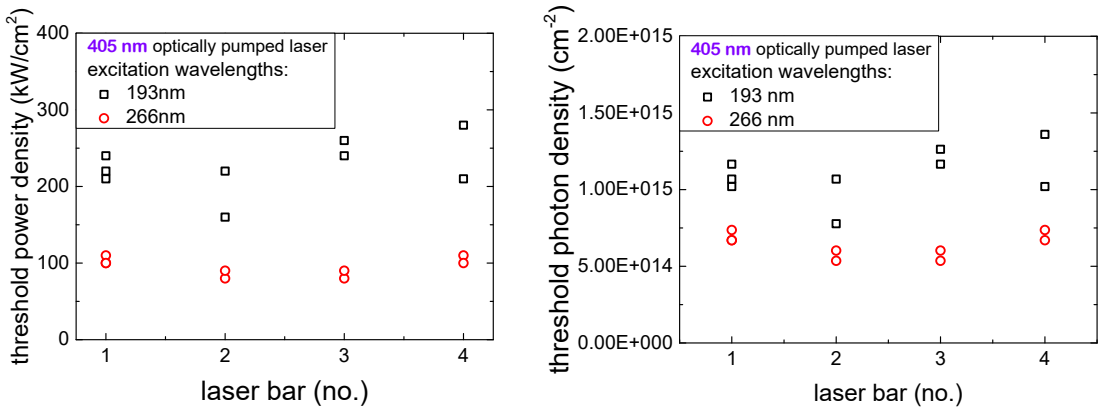

(a) threshold power density (b) threshold photon density

Figure 2.27 Optically pumped threshold power density (a) and threshold photon density (b) of an optically pumped laser with emission at 405 nm for different excitation wavelengths.

i.e. higher excitation wavelength. Therefore, the laser threshold photon density is compared in Fig. 2.27(b). Here, the difference of laser threshold for both setups is smaller but still present. This may be caused by the different penetration depth ($d_{193\,nm} = 1/\alpha_{193\,nm} \approx 38$ nm and $d_{266\,nm} = 1/\alpha_{266\,nm} \approx 57$ nm [29]) as well different surface reflectivity ($R_{193\,nm} = 34\,\%$ and $R_{266\,nm} = 21\,\%$ [11]) of the excitation lasers and resulting difference in excitation efficiency. However, it needs to be noticed that also slight variations in the excitation geometry can significantly influence the carrier density in the active region and consequently the determined laser threshold. The laser threshold of the optically pumped laser emitting in the violet spectral range can be compared to the laser threshold current density of an equivalent current injection laser diode. The laser diode heterostructure consists of the identical layers as the optically pumped laser with Mg doping in the upper GaN waveguide layer (compare Fig. 2.26). Additionally a 10 nm $Al_{0.09}Ga_{0.91}N$:Mg electron blocking layer is positioned between upper $In_{0.03}Ga_{0.97}N$ and GaN:Mg waveguide layer and a 500 nm thick $Al_{0.06}Ga_{0.04}N$:Mg upper cladding layer which is caped by a 20 nm GaN:Mg layer is introduced. The laser heterostructure is processed into gain guided laser diodes with 40 µm by 1300 µm cavities. This laser diode has typical laser threshold current densities in the range of 2 kA/cm^2 (Fig. 2.28). The comparison of this laser threshold current density with optically pumped laser threshold can be used as a benchmark in order to interpret the laser threshold power densities obtained from the setups.

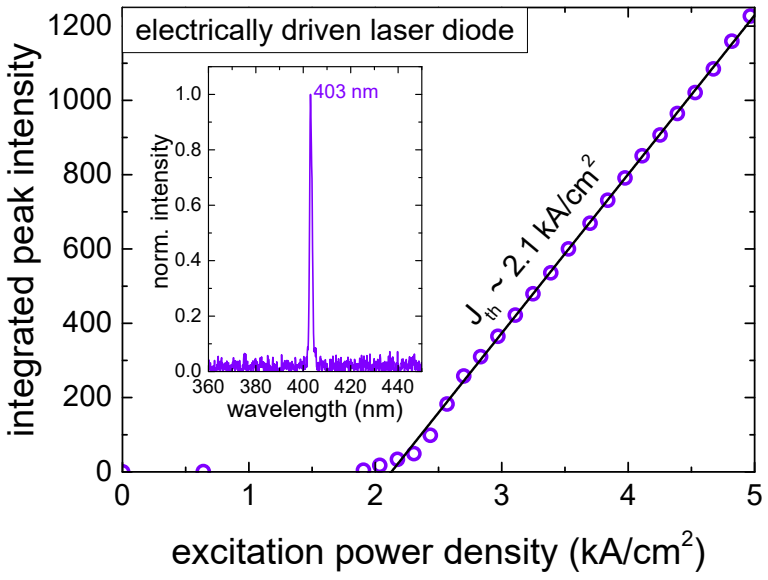

Figure 2.28 Laser threshold of a 405 nm electrically driven laser diode for comparison with optically pumped laser thresholds. The inset shows the emission spectrum above threshold. (measurement by FBH Berlin)

Chapter 3

Impact of threading dislocation density and morphology on laser performance

In order to achieve high modal gain and low threshold lasing the epitaxial layers of the laser heterostructures need to meet certain requirements in terms of material quality, homogeneity and morphology. Those aspect can be intentionally addressed by the choice of substrate or choosing proper parameters during epitaxial growth. This chapter discusses the influence of the threading dislocation density as well as the surface morphology and luminescence homogeneity on laser threshold and internal losses of optically pumped lasers.

3.1 Optically pumped lasers on sapphire and AlN substrates

The choice of substrate used for the epitaxial growth of the laser heterostructures can significantly affect the strain state, the defect density and the morphology of the epitaxial layers. So far optically pumped deep UV lasing obtained from AlGaN based MQW heterostructures grown on free standing bulk AlN [3,5,9,30], SiC [31–33], and sapphire substrates [4,10,30,34] has been demonstrated. In this chapter the suitability of bulk AlN and sapphire substrates for AlGaN based deep UV lasers is discussed. The ideal choice of substrate for the growth of AlGaN layers would be lattice matched, free standing AlGaN. This way the strain in the epitaxial layers can be minimized, which allows to grow thick layers without the formation of additional threading dislocations. However, so far bulk AlGaN substrates suffer from poor material quality, which makes them unsuitable for laser heterostructure growth [35]. Free standing AlN and GaN substrates on the other hand are commonly available in reasonable size and high material quality. Single crystalline bulk GaN substrates have proven to be ideal for the fabrication of low threshold GaN based laser diodes for the blue violet spectral range [36]. Due to the large lattice mismatch between GaN and the high Al content AlGaN layers needed for deep UV laser heterostructures (see section 2.1.1), which introduces high tensile strain within the epitaxial layers resulting in cracking of the layers [37], GaN cannot be used as substrate for growth of UVC laser heterostructures.

However, by choosing the proper heterostructure design, AlGaN based UVC lasers can be pseudomorphically grown on relaxed AlN avoiding strain relaxation, which ensures the high material quality (compare section 2.1.1) needed for low threshold lasing.
The bulk AlN substrates used for laser heterostructure growth in this study were grown by physical vapor transport (PVT) at the Leibniz Institute for Crystal Growth Berlin (IKZ) [38]. Fig. 3.1 shows an as grown single crystalline AlN boule, from which wafers are obtained by slicing along the c-plane and subsequent polishing. The circular bulk AlN substrates are 8 mm in diameter and exhibit threading dislocation densities (TDD) of less than $10^4\,\mathrm{cm}^{-2}$ as determined by defect selective etching.
As an alternative for bulk AlN as substrate for UVC heterostructure growth sapphire substrates can be used. For fabrication of AlN/sapphire templates thick relaxed AlN layers are grown on commercial 2-inch sapphire wafers. Due to the large lattice mismatch between the sapphire substrate and AlN layer, high numbers of dislocations are formed resulting in significantly higher TDD in the range of $2 \cdot 10^{10}\,\mathrm{cm}^{-2}$ [30, 39] compared to bulk AlN substrates. In terms of commercial availability, wafer size, and costs, however, sapphire is superior to bulk AlN substrates.
A method to reduce the TDD in AlN/sapphire substrates was found to be lateral overgrowth of patterned templates, which have already proven to be ideal for the growth of deep UV light emitters [40–42]. For this technique stripes with a width of 1.5 µm and a period of 3 µm are etched into planar AlN/sapphire templates described above. The structured templates are overgrown with AlN. Due to lateral growth of epitaxial layers eventually coalescence takes place in regions above the trenches of the patterned template. As a result smooth surfaces are formed. The lateral growth causes threading dislocations to bend. This way dislocations terminate at the semipolar facets formed or may cross at a certain point which can result in annihilation of the dislocations. Consequently, the TDD in regions above the trenches of patterned templates in those epitaxially laterally overgrown (ELO) AlN/sapphire templates is drastically reduced as shown in the transmission electron microscope (TEM) image in Fig. 3.2. The average TDD was determined to be as low as $5 \cdot 10^8\,\mathrm{cm}^{-2}$ [43].

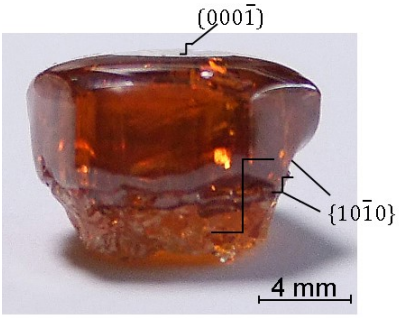

Figure 3.1 Optical microscope image of an AlN crystal grown by PVT at the Leibniz Institute for Crystal Growth. High quality wafers are obtained by slicing along the c-plane and subsequent polishing of the wafer surface. [38]

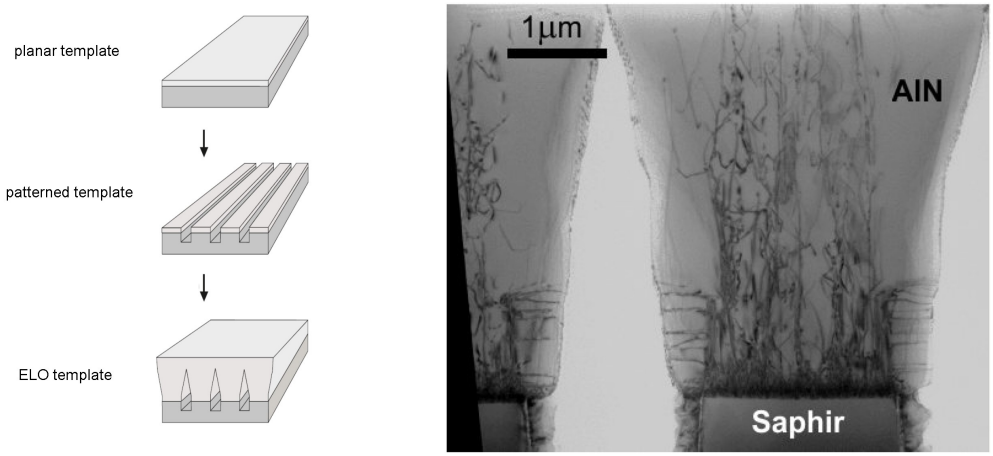

(a) schematic (b) TEM

Figure 3.2 Schematic of the ELO AlN/sapphire template fabrication [44] (a) and cross section transmission electron microscope image of an ELO AlN/sapphire template [45] (b).

In order to evaluate the suitability of the above described templates for growth of AlGaN MQW lases, identical laser heterostructures are grown on the tempates and experimentally compared. For this, on the AlN templates a 400 nm thick homoepitaxial AlN layer and a 25 nm thick transition layer from AlN to $Al_{0.80}Ga_{0.20}N$ was deposited. The active region consists of a threefold 2 nm $Al_xGa_{1-x}N$ / 4 nm $Al_{0.70}Ga_{0.30}N$ MQW for emssion around 270 nm and mode guiding is provided by $Al_{0.70}Ga_{0.30}N$ waveguide layers and an $Al_{0.70}Ga_{0.30}N$ lower cladding layer. HRXRD reciprocal space maps show that independent of the substrate the waveguide layers and the cladding layer are pseudomorphically strained with respect to the underlying AlN layers as discussed in section 2.1.1. In order to perform optical pumping experiments to determine the laser threshold, facets were cleaved along the $[11\bar{2}0]$ a-direction to form m-plane mirrors for the laser resonators as describe in section 2.1.2. No additional facet coating was applied. The resonator length of the laser structures was between 1 mm and 2 mm.
The PL spectrum of the AlGaN MQW structure grown on ELO AlN/sapphire is exemplarily shown in Fig. 3.3(a) for low temperature (5K) and room temperature (300K). As excitation source a 193 nm ArF excimer laser was used (see section 2.1.3). Independent of the choice of substrate the structures exhibit a PL peak at around 4.5 eV corresponding to the $Al_xGa_{1-x}N$ / 4 nm $Al_{0.70}Ga_{0.30}N$ MQW emission and a peak at around 5.0 eV corresponding to emission from the $Al_{0.70}Ga_{0.30}N$ waveguide layers. While the intensity of both peaks is comparable for low temperatures the waveguide peak decreases more rapidly with increasing temperature. The stronger intensity decrease of the waveguide emission originates not only from stronger nonradiative

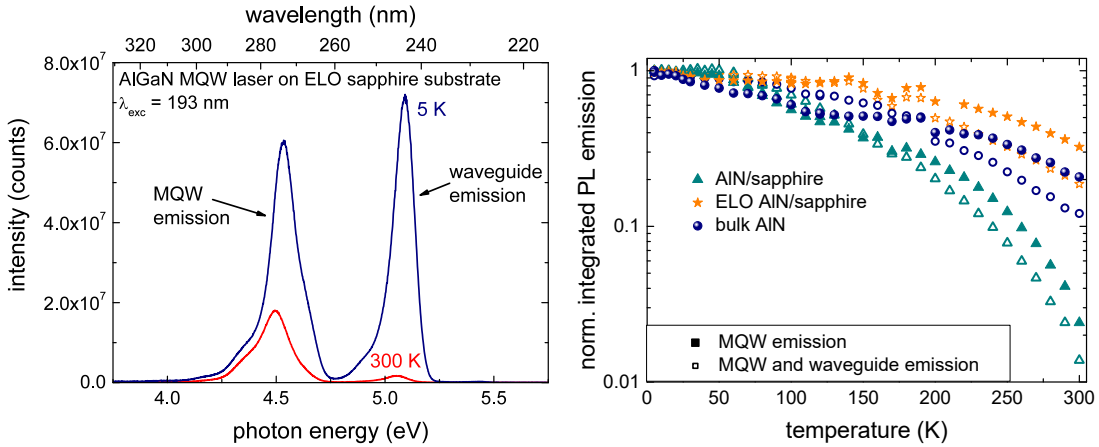

(a) PL spectra (b) intergrated PL emission

Figure 3.3 Low and room temperature PL spectra below laser threshold of laser heterostructures grown on ELO AlN/sapphire templates (a) and integrated PL intensity versus temperature of deep UV lasers grown on different substrates. [30]

recombination, but also from thermally activated redistribution of carriers into the MQW. Consequently the carrier density within the MQW is not independent of the temperature. Since a stable carrier concentration is required in order to determine the IQE by comparing room temperature and low temperature PL, this method can only be applied to provide an upper limit of the IQE. Nevertheless, it allows us to compare the efficiencies of structures grown on the different substrates. Fig. 3.3(b) shows the normalized integrated PL intensity of the MQW emission and the combined MQW and waveguide emission for the laser structures grown on the different substrates for different temperatures between 5 K and 300 K. By comparing room temperature and low temperature PL intensities, the IQE of the AlGaN MQW laser structures grown on low defect ELO AlN/sapphire and bulk AlN substrates was estimated to be in the range of 20 % to 30 % and 10 % to 20 %, respectively. The PL intensity of the layers grown on planar AlN/sapphire, however, drops drastically with increasing temperature reaching only 1 % to 3 % of the low temperature intensity. These results show that the high defect density in the MQW grown on planar AlN/sapphire substrate leads to an IQE about one order of magnitude lower compared to the structures grown on the low defect density material.

When optically pumped in stripe geometry (compare section 2.2) the laser structure grown on bulk AlN exhibits lasing at 279 nm with a threshold power density of 10 MW/cm^2 (see Fig. 3.4(a)). Fig. 3.4 shows the integrated room temperature emission peak intensity measured at one facet for different excitation power densities. For the here used excitation wavelength of 266 nm all layers except for the

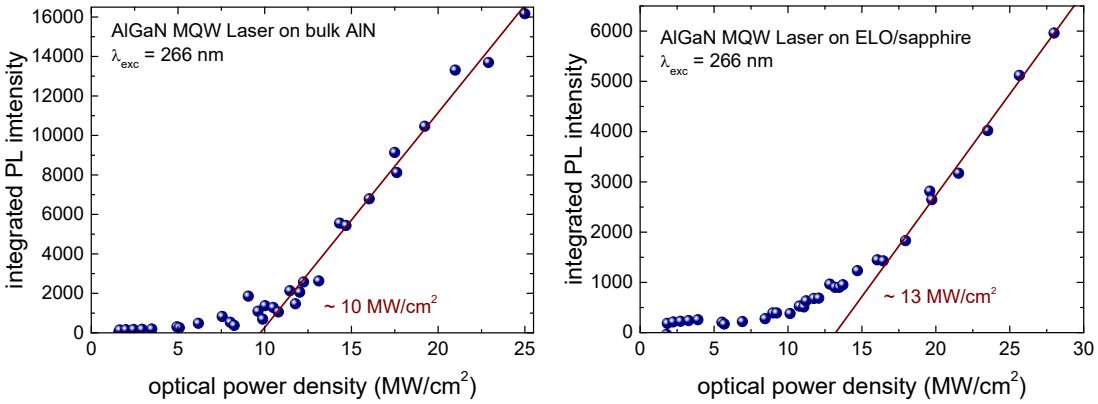

(a) bulk AlN substrate (b) ELO AlN/sapphire template

Figure 3.4 Integrated peak intensity collected from cleaved facets of laser heterostructures emitting around 275 nm grown on bulk AlN substrate (a) and ELO AlN/sapphire template (b). [30]

MQWs are transparent. Consequently only approximately one tenth of the excitation power is absorbed resulting in a lower carrier concentration compared to shorter wavelength pumping. Therefore, the laser threshold is considerably higher compared to reported values obtained by non-resonant pumping [5, 9, 34]. However, due to the lack of knowledge regarding the absorbed pump power, the diffusion length for photogenerated carriers in the studied structures and hence the unknown carrier density within the quantum well active region, a quantitative comparison is difficult as discussed in sections 2.3 and 2.4. This also applies to all laser threshold values discussed in the following that were determined by pumping with 193 nm ArF excimer laser.

The AlGaN MQW heterostructures grown on ELO AlN/sapphire templates exhibit lasing at a wavelength of 272 nm and a threshold power density of 13 MW/cm^2 (see Fig. 3.4(b)). This was the first demonstration of laser emission from AlGaN based MQWs grown on sapphire substrate in this wavelength range [30]. The AlGaN MQW structures grown on planar AlN/sapphire templates exhibit no lasing for excitation power densities of up to 50 MW/cm^2. This can be attributed to the low IQE of the lasers grown on planar AlN/sapphire resulting in short carrier lifetimes and therefore a lower carrier density per absorbed pump power.

The results prove that the material quality of AlN/sapphire templates can be significantly improved by using ELO technology, resulting in a threshold power density of AlGaN based MQW laser heterostructures grown on those templates which is only slightly higher than for structures grown on bulk AlN substrates. Considering the advantages of sapphire substrates regarding availability, waver size, and costs, ELO

AlN/sapphire templates are a promising alternative to bulk AlN substrates for this application. Thus, the following sections and chapters will focus on this approach.

3.2 Surface morphology of lasers grown on patterned sapphire substrates

Laser heterostructures as described above show laser threshold densities of more than 6 MW/cm^2 under optical pumping with an excitation wavelength of 193 nm, which is comparatively high indicating high optical losses. Despite high material quality in terms of low defect densities and resulting low non-radiative recombination rates, the morphology of the epitaxial layer is a critical factor for low laser threshold as scattering processes may introduce high additional waveguide losses [46]. Additionally, the morphology can affect the incorporation of atoms during growth and therefore cause luminescence inhomogeneities [47] broadening the gain spectrum and eventually also increased modal losses. Especially the fact that the pattering of the substrate needed for the ELO process introduces lateral variations [48, 49] needs to be investigated in more detail.

3.2.1 Effect of pit density on optical losses

The surface morphology of an optically pumped laser heterostructure with a threefold 2 nm $Al_xGa_{1-x}N$ / 4 nm $Al_{0.70}Ga_{0.30}N$ MQW for emission around 275 nm embedded in $Al_{0.70}Ga_{0.30}N$ waveguide layers and a lower $Al_{0.80}Ga_{0.20}N$ cladding layer can be seen in the atomic force microscope (AFM) image in Fig. 3.5. The heterostructure in the left image clearly shows the presence of high numbers of hexagonal V-pits with diameters of more than 100 nm on the $Al_{0.70}Ga_{0.30}N$ waveguide surface, which can also be observed in InGaN layers grown on sapphire substrates [50]. The formation of V-pits can be controlled by growth parameters, as the surface mobility of the adatoms during growth strongly depends on parameters like pressure and temperature. The

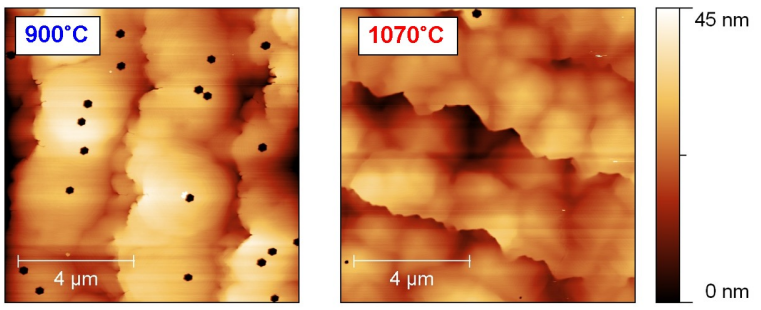

Figure 3.5
$10\,\mu m \times 10\,\mu m$ AFM images of laser heterostructures grown at different temperatures by MOVPE. [22]

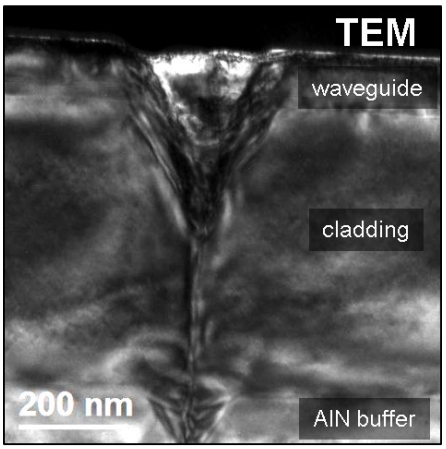

Figure 3.6 Cross section Transmission electron microscope (TEM) image of a laser heterostructure showing a V-pit (measurement by J. Park (TU Berlin)). [22]

right image in Fig. 3.5 shows the surface of a laser heterostructure, which was grown with increased temperature during growth of the MQW and waveguide layers. This drastically suppresses the formation of V-pits, which results in reduction of the V-pit density from $2.2 \cdot 10^7$ at 900 C° to $3 \cdot 10^6$ at 1070 C°.

In order to investigate the origin of the V-pits cross section TEM analysis was performed (see Fig. 3.6) [22]. The V-pit penetrates the complete waveguide layer. As origin of the pit a threading dislocation is identified, which can be clearly seen at the tip of the V-pit. At the surface the V-pit has a diameter of about 200 nm. As the V-pit is filled with the surrounding atmosphere the optical mode is facing a refractive index change from about 2.5 within the $Al_{0.70}Ga_{0.30}N$ waveguide to 1. This causes scattering of the optical mode and therefore increased waveguide losses lowering the net gain.

The influence of the pit density on the optically pumped laser threshold is shown in Fig. 3.7. The reduction of the pit density of about one order of magnitude results in a

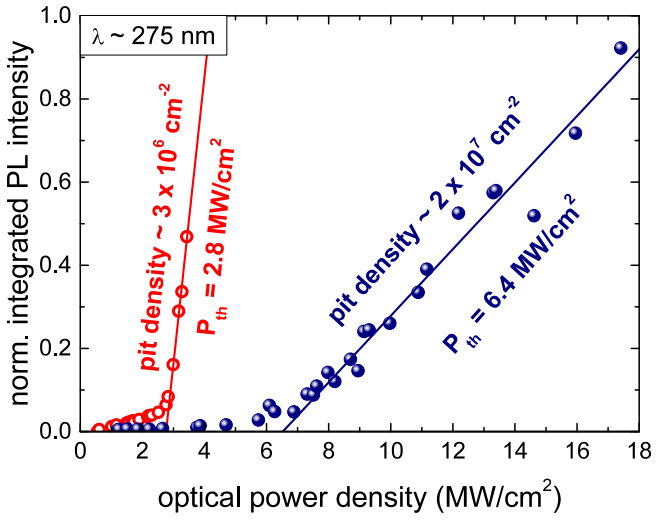

Figure 3.7 Laser threshold power densities of laser heterostructures grown at different temperatures and consequently exhibiting different V-pit densities. [22]

decrease of the laser power threshold from 6.4 MW/cm^2 to 2.8 MW/cm^2. This is attributed to reduced modal losses due to suppressed scattering at the V-pits indicating the importance of smooth and homogeneous morphology of the laser heterostructures.

3.2.2 Effect of height fluctuations and composition inhomogeneity on optical losses and laser threshold

The above discussed laser heterostructure surfaces exhibit not only V-pits which affect the laser performance but also a step-like morphology. The period of the steps match the period of the stripe pattern etched into the AlN/sapphire templates used for the ELO process. This is clear evidence that the step bunching results from the lateral overgrowth. Fig. 3.8(a) shows a schematic of the ELO growth. In order to obtain step flow growth of the AlN, the commercial sapphire substrate is fabricated with slight miscut to the m-plane [51]. This results in step bunching of the epitaxial layers after coalescence is reached. The step height depends on the miscut angle [49, 52]. The laser heterostructures discussed above were grown on sapphire substrates with a nominal miscut angle of 0.2 °. The morphology of an ELO AlN/sapphire template used for growth of laser heterostructures can be seen in the AFM image in Fig. 3.8(b). The template exhibits distinct steps following the stripe pattern of the ELO process with step heights in the range of 20 nm. This morphology is persistent throughout heterostructure growth, which can be concluded from the observation that the surface of a complete optically pumped laser heterostructures exhibits the same stripe-like pattern (see Fig. 3.9 left). Therefore, those steps are present at each heterostructure

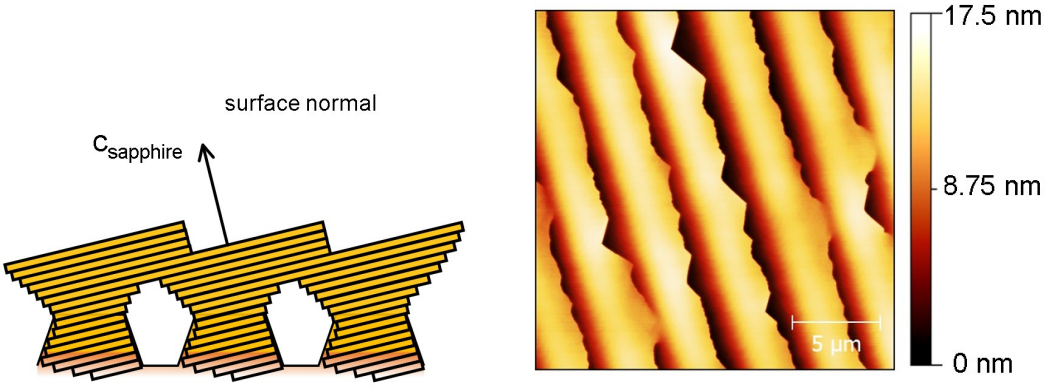

(a) schematic (b) AFM

Figure 3.8 Schematic of ELO AlN/sapphire template growth with step bunching [49] (a) and 20 µm × 20 µm AFM image of an ELO AlN/sapphire template with an nominal offcut of 0.2° (measurement by J. Enslin (TU Berlin)) (b).

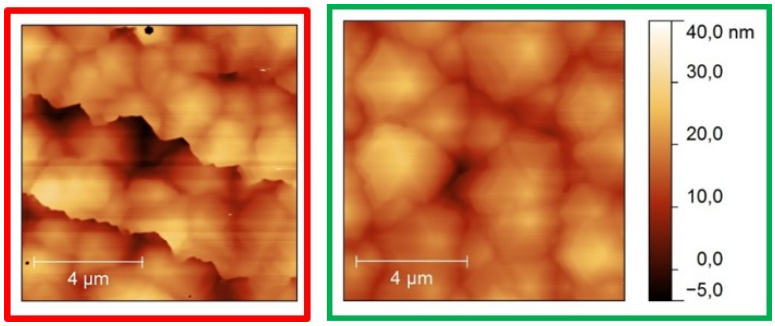

Figure 3.9 AFM images of optically pumped UV laser heterostructures with and without step bunching (measurement by C. Kuhn (TU Berlin)).

interface. As this introduces a refractive index change in direction of mode perturbation optical losses are increased by scattering processes [53] comparable to scattering at the V-pits (compare section 3.2.1).

As mentioned above the height of the steps in ELO AlN/sapphire templates depends on the miscut angle of the sapphire substrate [49]. Recently it was found that the step heights strongly affects the surface morphology. With decreasing miscut angle and step height the step bunching can be inhibited [52]. As critical miscut angle 0.14 ° could be identified. The surface morphology of an optically pumped laser heterostructure grown on ELO AlN/sapphire without step bunching is shown in the right AFM image in Fig. 3.9. The surface is comparably smoother and macrosteps as observed for heterostructures grown on templates with step bunching are not present.

In order to investigate the influence of the different surface morphologies on the luminescence characteristics of the optically pumped lasers cathodoluminescence (CL) experiments were conducted (measurement by U. Zeimer (FBH Berlin)). Fig. 3.10 shows CL peak wavelength maps at 80 K and the corresponding histograms of optically pumped deep UV laser heterostructures with and without step bunching. The MQW emission from heterostructures with step bunching exhibit considerably high peak wavelength distribution throughout the 5 µm × 5 µm CL map. While the peak wavelength for this laser scatters in a range of 30 nm, the laser without step bunching exhibits scattering in the range of 9 nm. The local spectra, however, exhibit comparable full with at half maximum (FWHM) for both lasers (spectra not shown). The broad emission peak distribution of the laser structure with step bunching can be attributed to high Ga incorporation at the macrosteps due to higher mobilities of Ga adatoms compared to Al adatoms during growth. Therefore, the wavelength of emission from region in the vicinity of the steps increases [47].

The modal losses of AlGaN MQW lasers can be determined from gain spectra obtained by the VSLM (see section 2.2.1). Fig. 3.11(a) shows the net gain spectra of optically pumped laser heterostructures for emission around 275 nm with and without step bunching. Both lasers exhibit a distinct modal gain peak with comparable

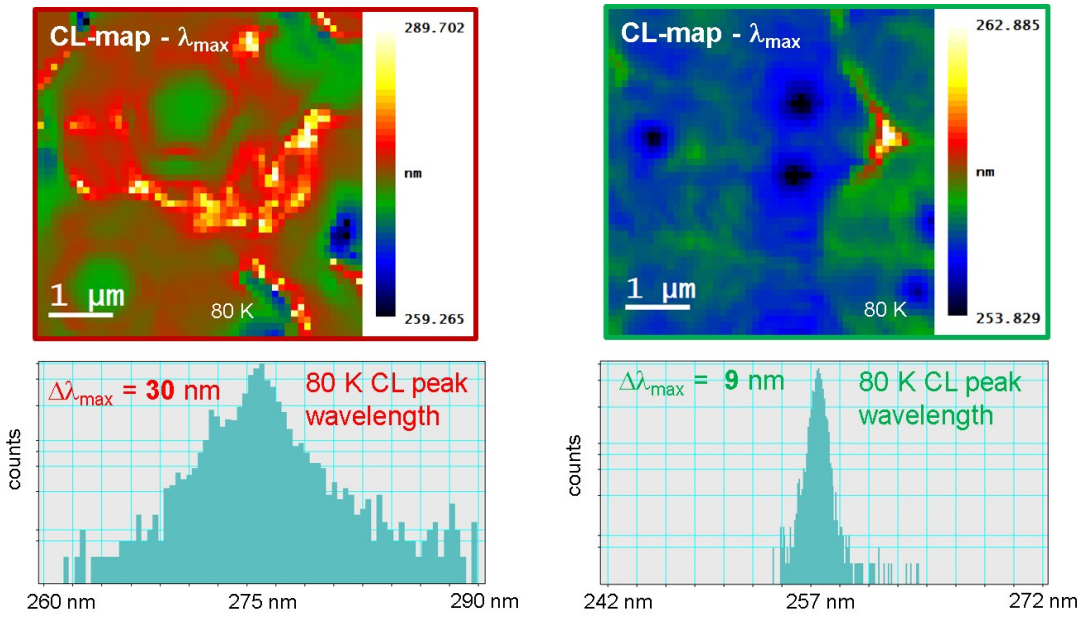

(a) step bunching (b) without step bunching

Figure 3.10 Cathodoluminescence (CL) peak wavelength map and peak wavelength distribution at 80 K of optically pumped laser heterostructures with step bunching (a) and without step bunching (b). (measurement by U. Zeimer (FBH Berlin))

characteristics. The internal losses, however, of the structure with step bunching are $\sim 25\,\mathrm{cm}^{-1}$ higher significantly lowering the net gain. This strongly influences the laser threshold power density as shown in Fig. 3.11(b). The improved surface morphology by optimized choice of substrate reduces the laser threshold power density

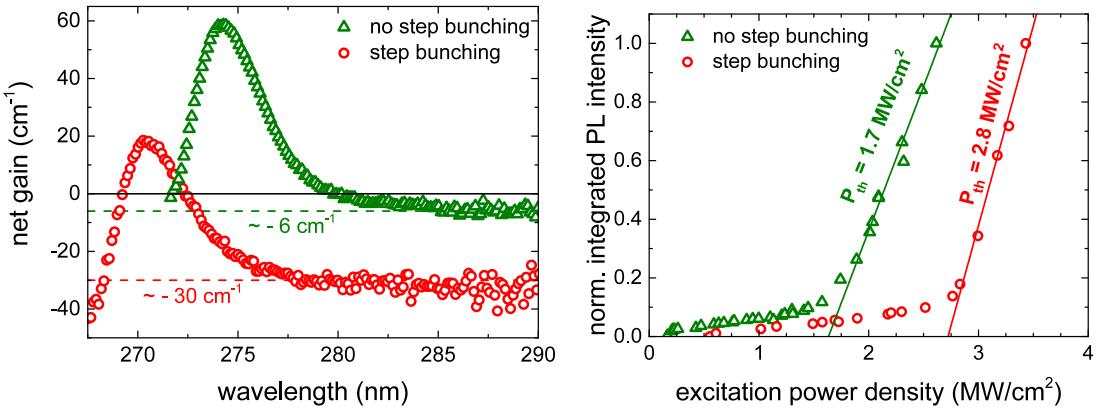

(a) net gain (b) laser threshold

Figure 3.11 Optical gain spectra (a) and laser threshold power densities (b) of laser heterostructures with and without step bunching.

from 2.8 MW/cm^2 to 1.7 MW/cm^2 [52]. However, it needs to be noticed that the sapphire miscut angle can also affect the TDD in the ELO AlN/sapphire templates. For higher miscut angle the reduction of TDD by the lateral overgrowth may be more efficient as inclined grain boundaries are generated at the coalescence point propagating through the AlN additionally annihilating threading dislocations [49]. This effect counteracts the advantages of improved surface morphology. The impact of those effects on the laser threshold may differ for different material composition and emission wavelength. In fact, for laser heterostructures emitting around 240 nm grown on ELO AlN/sapphire templates the laser threshold power density was observed to increase with decreasing miscut angle of the sapphire [54] indicating that in this experiment the effect of increased carrier life times is more important than reduced scattering losses.

Although step bunching can be suppressed by the use of substrates with low miscut angle, the surface morphology of the laser still exhibits a certain height fluctuation. Additionally, it was found that $Al_{0.80}Ga_{0.20}N$ cladding layers can exhibit compositional fluctuations and partial strain relaxation. A promising approach for improving the morphology and structural properties of AlGaN layers has proven to be the introduction of a layer stack with alternating Al content instead of a single layer [55–57]. The optical properties of such a short period super lattice (SPSL) are comparable to those of thick layers with the same Al content as the average Al content in the SPSL, while electrical properties can even be improved in SPSLs (compare section 5.1.1). Fig. 3.12 shows AFM images of a 1 µm thick single $Al_{0.80}Ga_{0.20}N$ and an $Al_{0.80}Ga_{0.20}N$ SPSL cladding layer. The SPLS cladding layer exhibits reduced height fluctuations which results in reduced surface roughness (rms roughness 5.8 nm to 2.5 nm). Additionally it was shown that SPSL cladding layers do not exhibit compositional fluctuation as observed for single $Al_{0.80}Ga_{0.20}N$ cladding layers determined by XRD measurements [58]. In order to investigate the influence of the improved surface morphology and compositional uniformity identical laser heterostructures were grown

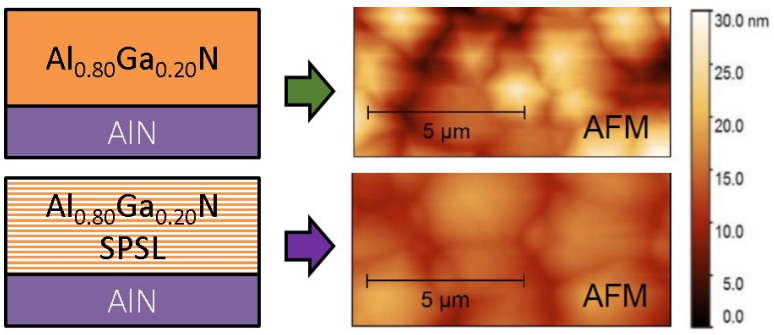

Figure 3.12 AFM images of a thick $Al_{0.80}Ga_{0.20}N$ cladding layer and an SPSL cladding layer with an average Al content of 80 %. [58]

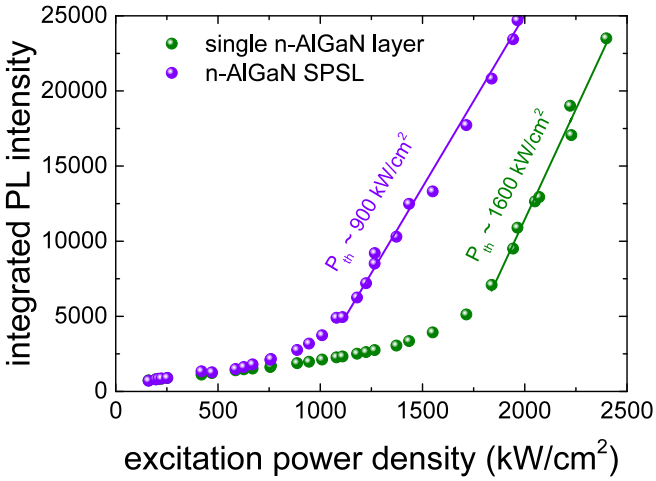

Figure 3.13 Laser threshold density of laser heterostructures emitting at 270 nm with a thick $Al_{0.80}Ga_{0.20}N$ cladding layer and a SPLS cladding layer with an average Al content of 80 %. [58]

with a single $Al_{0.80}Ga_{0.20}N$ cladding layer and an $Al_{0.80}Ga_{0.20}N$ SPSL cladding layer. The introduction of the SPSL leads to a reduction of the laser threshold power density from 1600 kW/cm^2 to 900 kW/cm^2 (see Fig. 3.13).

The studies discussed in this chapter show that the choice of substrate is a critical issues for the fabrication of low threshold AlGaN MQW lasers. Defect reduced AlN/sapphire templates have proven to be an alternative to low defect density single crystal bulk AlN. However, by introducing the ELO process lateral inhomogeneities are generated in the laser heterostructure, which may affect laser performance. By choosing a proper sapphire substrate and optimized growth conditions the optically pumped laser threshold power density of AlGaN MQW lasers emitting around 270 nm can be significantly reduced to values well below 1 MW/cm^2.

Chapter 4

Influence of multiple quantum well active region on laser performance

In chapter 3 was shown that the defect density in and the morphology of the semiconductor crystal have a major influence on the optically pumped laser threshold. At this point the design of the active region has not been investigated. From studies performed on deep UV LEDs it is known that parameters like QW thickness and number can also affect the emitter characteristics [59]. Those findings, however, are not necessarily applicable to the design of laser diodes. For the development of efficient LEDs the focus mainly lies on the reduction of non radiative recombination rates and the maximization of radiative recombination rates, which can e.g. be accomplished by an increase of the wave function overlap of electrons and holes or limiting carrier densities within the QWs ensuring that non radiative recombination processes with a higher order dependency on the carrier concentration (e.g. Auger recombination) do not take over. In order to achieve lasing, on the other hand, two major requirements have to be fulfilled. First, carrier density in the active region has to be high enough to reach transparency and second, sufficient modal gain has to be present to eventually overcome the waveguide and mirror losses. The former can be accomplished by limiting the total recombination rates including non radiative and radiative recombination as well, which is contrary to the requirements for efficient LEDs. For the latter high material gain is needed, which increases with e.g. increased transition matrix element and consequently radiative recombination rates [15].
In this chapter the influence of the composition and design of the active region in optically pumped lasers on the laser performance is investigated. Theoretical calculation and photo- as well as elctroluminescence experiments show that the optical polarization of $Al_xGa_{1-x}N/Al_yGa_{1-y}N$ MQW can be affected by the QW composition and strain and therefore by MQW design parameters as the barrier height and QW thickness [60–65]. The optical polarization of the spontaneous as well as laser emission of the present deep UV optically pumped lasers for different wavelengths is discussed in section 4.1 before the effects of emission wavelengths and active re-

gion design parameters on the laser threshold and optical gain will be discussed in section 4.2.

4.1 Optical polarization of quantum well emission

Due to the spin-orbit interaction and the crystal field in AlGaN material the valence band splits into three subbands with different symmetries and energy states for the holes. Depending on the symmetry the emission from electron-hole recombination is either TE or TM polarized. The crystal field energy and therefore the valence band order strongly depends on the Al content of the $Al_xGa_{1-x}N$ crystal (12.3 meV for GaN [66] and - 221 meV for AlN [67]), which results in a change of polarization from TE for GaN to TM for AlN. This leads to a transition from TE dominant to TM dominant emission for shorter wavelengths emission of AlGaN layers. The position of this transition within the $Al_xGa_{1-x}N$ composition range strongly depends on the strain within the layers [62, 63, 65].
Fig. 4.1(a) shows the polarization resolved spontaneous QW emission extracted through the m-plane crystal facet of optically pumped lasers for different MQW composition emitting between 240 nm and 280 nm normalized to the dominant polarized emission peak. Due to the wide range of QW composition and emission wavelength different barrier and waveguide compositions had to be chosen. While the structures emitting above 250 nm have $Al_{0.70}Ga_{0.30}N$ barriers and waveguide layers, for the laser emitting

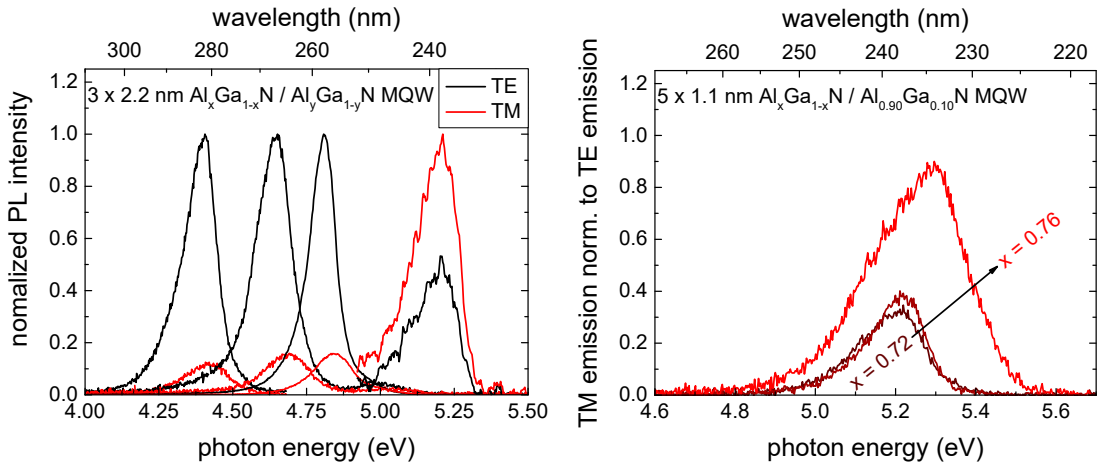

(a) emission from 2.2 nm QWs (b) emission from 1.1 nm QWs

Figure 4.1 Polarization resolved emission spectra collected from the facet below laser threshold of optically pumped laser structures with 2.2 nm QWs (a) and 1.1 nm QWs (b) with different QW composition.

at lower wavelength the composition of those layers was increased to an Al content of 90 %. With increasing Al content in the 2.2 nm thick QWs and decreasing emission wavelength the TM polarized contribution to the total emission increases. For emission wavelengths below 250 nm the emission is strongly TE polarized. Emission at 238 nm, on he other hand, is TM dominated indicating a transition from TE to TM at a wavelength between 238 nm and 258 nm. Since the different subbands are thermally occupied the emission is usually not solely TE or TM polarized. The peak of the dominant emission is slightly shifted to lower energies compared to the peak with lower intensity indicating that the dominant transition originates from the subband with the lowest energy. With decreasing emission wavelength the spacing between the different subbands decreases which leads to smaller spacing of the differently polarized emission peaks for less polarized MQW emission resulting in almost equal emission energies in case of the optically pumped laser structures emitting at 238 nm.
Since the holes in the different subbands have different effective masses the energy level of their confined states in the QW differ and the energy level is differently affected by parameters like QW thickness and barrier height. Therefore, active region design parameters can also influence the polarization degree of the QW emission. With decreasing QW thickness or increasing barrier height the hole states shift towards the energy level of the barriers. However, the holes causing TM polarized emission have a higher effective mass than the ones causing the TE polarized emission. With increasing spacing the occupation of the subbands becomes more inhomogeneous. Consequently, the overall MQW emission has a larger TE polarized contribution [65]. However, it needs to be noticed that this effect can only be observed up to a certain QW thickness. The energy shift towards the barrier becomes less prominent for energies close to the continuum energy and the spacing to the energy state with the larger hole masses decreases again, which could result into lower degrees of polarization of the MQW emission.
Fig. 4.1(b) shows the TM polarized emission normalized to the respective TE emission peak (not shown) of fivefold 1.1 nm thick MQWs with different Al concentration ranging from 72 % to 76 % with $Al_{0.90}Ga_{0.10}N$ barriers and waveguide layers. The MQW emission is between 235 nm and 238 nm depending on MQW composition. The PL peak is somewhat broadened compared to the threefold 2.2 nm MQW emission which can be attributed to effects resulting from the higher QW number (compare section 4.2.2). All emission peaks are TE dominated with an increasing TM contribution for decreasing emission wavelength. However, even for an emission wavelength of 235 nm the peak is TE dominated indicating that the transition from TE to TM dominated emission is shifted towards shorter wavelengths for 1.1 nm thick QWs compared

to 2.2 nm thick QWs. This effect can partially be attributed to the different influence of the confinement on holes with different effective masses discussed above. On the other hand also the general decrease of emission wavelength for thinner QW and higher confinement has to be taken into account. The combination of both effects results in the observed increase of TE polarized contribution to the MQW emission for smaller QW thicknesses.

The experimentally determined degree of polarization of optically pumped lasers with different QW composition and thickness as well as different composition in the barriers and waveguide layers is shown in Fig. 4.2 in dependance of the emission wavelength. Also shown are simulated values calculated according to a k · p-perturbation model (model and calculations by C. Reich (TU Berlin) [65]) for 2.2 nm thick QWs and $Al_{0.70}Ga_{0.30}N$ barriers for emission above 250 nm as well as 1.1 nm and 2.2 nm thick QWs with $Al_{0.90}Ga_{0.10}N$ for emission below 250 nm. The emission wavelength was varied by adjusting the QW composition. The emission wavelengths from the simulations were corrected in order to match the excitonic transition from the experiment. The exciton binding energy in bulk $Al_xGa_{1-x}N$ layers ranges from 28 meV for GaN [68] to 53 meV for AlN [42]. The exciton binding energy in 2D confined systems like QWs, however, can be significantly higher [69, 70]. An exciton binding energy in the MQW of 150 meV was estimated for the optically pumped laser and subtracted from the band to band transition calculated by the k · p-perturbation approach.

Independent of the QW thickness the experiments show strongly TE polarized MQW emission for wavelengths longer than 250 nm. The simulation predicts almost completely TE polarized emission of 2.2 nm thick QWs for a wavelength of 270 nm and

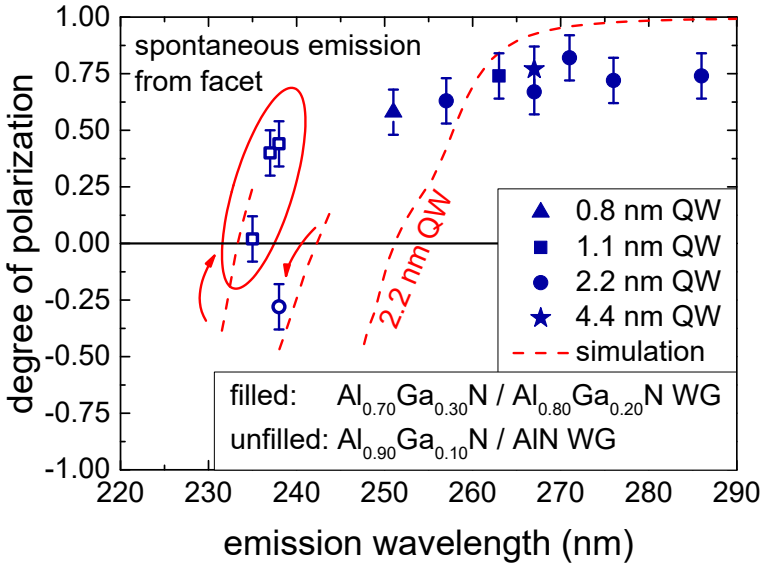

Figure 4.2 Degree of polarization of MQW emission of optically pumped laser structures with different QW width and composition. The dashed lines show simulations for the respective heterostructures (performed by C. Reich (TU Berlin)).

longer. The degree of polarization determined by the experiment, however, is limited by the collection of unpolarized stray light [64, 65], which results in a saturation of the measured polarization at a value of ~ 0.75. The transition from TE dominant to TM dominant MQW emission can be very well verified by the experiment. For heterostructures with $Al_{0.90}Ga_{0.10}N$ barriers and waveguide layers this transition is shifted to shorter wavelengths compared to lasers with $Al_{0.70}Ga_{0.30}N$ barriers and waveguide layers. This matches the slightly TM dominant MQW emission at 238 nm from MQW embedded in $Al_{0.90}Ga_{0.10}N$ barriers and waveguide layers. A further increase of the TE contribution to the MQW emission in the same wavelength range can be observed by experiment and simulation as well for reduced QW thicknesses of 1.1 nm (see Fig. 4.2).

The polarization resolved spectra for optically pumped lasers above threshold of 3.0 nm thick QWs emitting at 241 nm and 2.2 nm thick QWs emitting at 267 nm is shown in Fig. 4.3(a). Both emission peaks are strongly polarized. The laser emission at 241 nm is TM and the emission at 267 nm is TE polarized. This is consistent with observation of a transition from TE to TM polarized emission in a wavelength range between 240 nm and 250 nm for spontaneous emission from thicker QWs discussed above. All lasers with emission wavelength above 255 nm were found to exhibit strong TE polarization (see Fig. 4.3(b)). The degree of polarization of the emission above threshold is somewhat higher compared to the spontaneous emission. The laser emission itself is expected to be strictly TE or TM polarized depending on the polarization dependence of the optical gain. However, also less polarized spontaneous

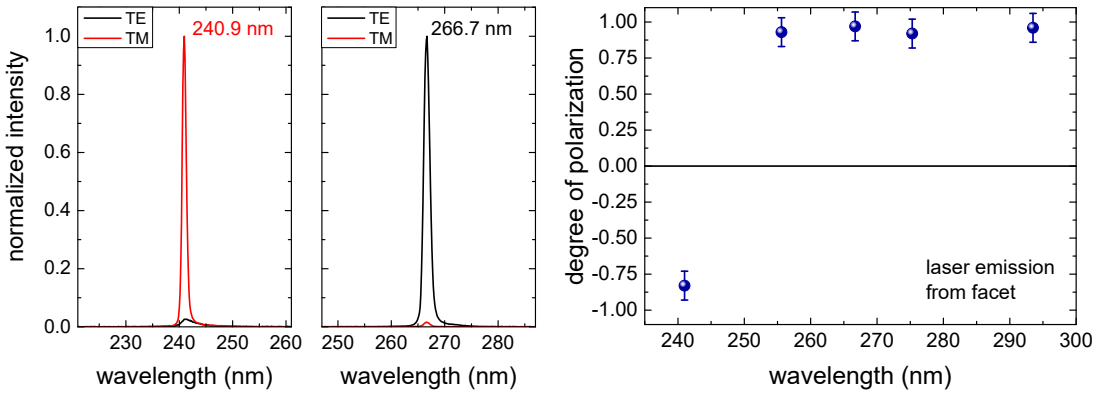

(a) laser spectra (b) degree of polarization

Figure 4.3 Polarization resolved laser spectra at 241 nm and 267 nm collected from the facet of optically pumped laser structures with 3.0 and 2.2 nm thick QWs, respectively (a) and the degree of polarization of laser emission from optically pumped lasers with different emission wavelength (b).

emission may be present in the spectra above threshold additionally to unpolarized stray light which eventually results in smaller values for the degree of polarization.

4.2 Laser threshold and optical gain

The design of the MQW active region determines parameters like emission wavelength, carrier density and the confinement factor of the lasers. In order to realize low laser threshold and high modal gain the influence of design parameters like QW number, QW thickness and composition on the laser performance needs to be investigated.

4.2.1 Influence of emission wavelength

The emission wavelength of the optically pumped lasers is mainly determined by the composition of the QWs. By altering the Al content in the QWs from 38% to 75% optically pumped lasing was achieved in a wide wavelength range between 237 nm and 293 nm (see Fig. 4.4). In order to cover this wide wavelength range different waveguide designs need to be utilized. The lasers with emission wavelengths above 250 nm consist of a $Al_{0.70}Ga_{0.30}N/Al_{0.80}Ga_{0.20}N$ mode guiding structure. For shorter wavelengths this design cannot provide sufficient carrier and optical confinement. Therefore, the MQW active regions emitting below 250 nm were embedded into $Al_{0.80}Ga_{0.20}N$ waveguide and AlN cladding layers, which will be discussed more detailed in section 4.2.2. In order to study the influence of the emission wavelength of the lasers on their performance, QWs with different Al content were embedded in the same waveguide design of optically pumped lasers, which is identical to the one discussed in the previous

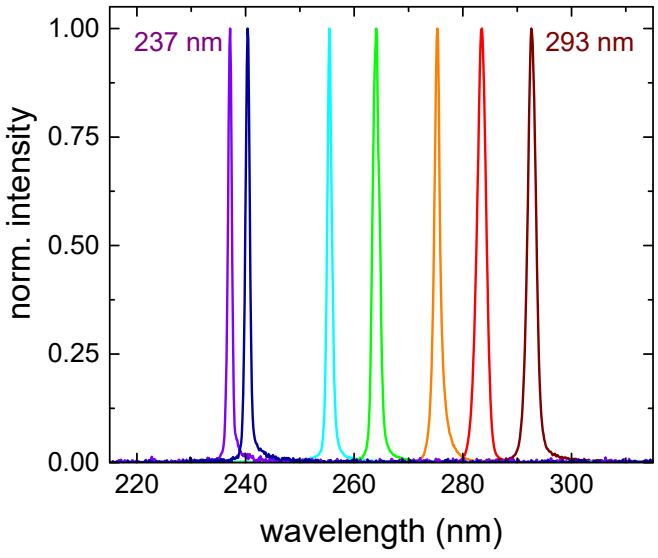

Figure 4.4 Optically pumped laser spectra with emission wavelengths ranging from 237 nm to 293 nm. For emission wavelengths above 250 nm the active region was embedded into a $Al_{0.70}Ga_{0.30}N/Al_{0.80}Ga_{0.20}N$ mode guiding structure. For shorter wavelengths $Al_{0.80}Ga_{0.20}N$ waveguide and AlN cladding layers were used.

chapters. A threefold 2.2 nm $Al_xGa_{1-x}N$ / 5 nm $Al_{0.70}Ga_{0.30}N$ MQW active region is sandwiched between two $Al_{0.70}Ga_{0.30}N$ waveguide layers and a lower $Al_{0.80}Ga_{0.20}N$ cladding layer (see Fig. 4.5(a)). All discussed heterostructures were grown on ELO AlN/sapphire templates (compare section 3.1). It is obvious that an upper limit of the Al content in the QWs is given by the composition of the waveguide layers and quantum barriers with an Al content of 70% in order to provide electrical as well as optical confinement. As the refractive index depends on the wavelength of the traveling light, the confinement factor is also affected by the emission wavelength.
The confinement of the optical mode within the waveguide structure is given by the refractive index difference between the cladding and waveguide layer. The smaller the refractive index contrast the stronger the mode penetrates the cladding layers. Fig. 4.5(b) shows the refractive indices of the $Al_{0.70}Ga_{0.30}N$ waveguide layers and the $Al_{0.80}Ga_{0.20}N$ cladding layer of the discussed mode guiding structure for different emission wavelengths. With increasing wavelength the refractive indices decrease. Since the decrease is stronger for wavelengths corresponding to a photon energy which is closer to the band gap energy of the semiconductor material, the refractive index difference between waveguide and cladding layer also decreases for increasing emission wavelength, which results in a decrease of the confinement factor from 0.057 for 260 nm to 0.048 for 290 nm. At wavelengths below 260 nm the confinement factor decreases again according to the calculation as the influence of the higher Al content and resulting lower refractive index in the QWs pushes the mode into the cladding layers. However, throughout this entire spectral range the calculated confinement

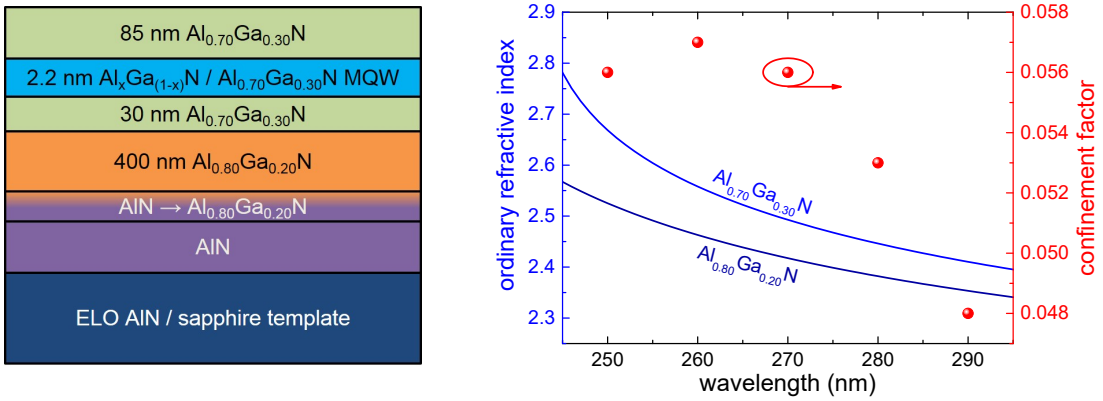

(a) heterostructure (b) optical confinement

Figure 4.5 Schematic of the optically pumped laser heterostructure (a) and refractive index of the $Al_{0.70}Ga_{0.30}N$ waveguide and $Al_{0.80}Ga_{0.20}N$ cladding layer calculated according to a model by [11] with experimental data from [12–14] as well as the calculated confinement factor in dependance of the emission wavelength (b).

factors with 0.048 and more reach reasonable values for high modal gain compared to GaN based lasers operating in the visible spectral range [71].
Additionally to the optical confinement the QW composition also influences the carrier confinement in the MQW active region. Since the barrier concentration is kept constant for the discussed emission range between 250 nm and 290 nm the potential barrier between QW and quantum barrier, which prevents the carriers from escaping the QWs, decreases with decreasing wavelengths as the difference of the Al content between QW and quantum barrier decreases. Fig. 4.6(a) shows room temperature PL spectra from optically pumped laser heterostructures with different emission wavelengths. The waveguide design is the same for all lasers (see Fig. 4.5(a)). The Al content in the AlGaN QWs was varied between 38% and 52%. The spectra show dominant QW emission with increasing peak wavelength from 260 nm to 287 nm with decreasing Al content in the QW. All spectra exhibit an additional emission peak at higher photon energies corresponding to emission from the $Al_{0.70}Ga_{0.30}N$ waveguide layers and quantum barriers, which are identical in all samples. Although most electron hole pairs are photogenerated in the upper $Al_{0.70}Ga_{0.30}N$ waveguide layer this emission peak is at room temperature considerably smaller compared to MQW emission, since the carriers tend to relax into the MQW. Additionally, due to the lack of carrier confinement radiative recombination rates are expected to be lower in the thick layers compared to QWs. It is obvious that the energy difference between the QW peak and waveguide and quantum barrier peak decreases for decreasing emission

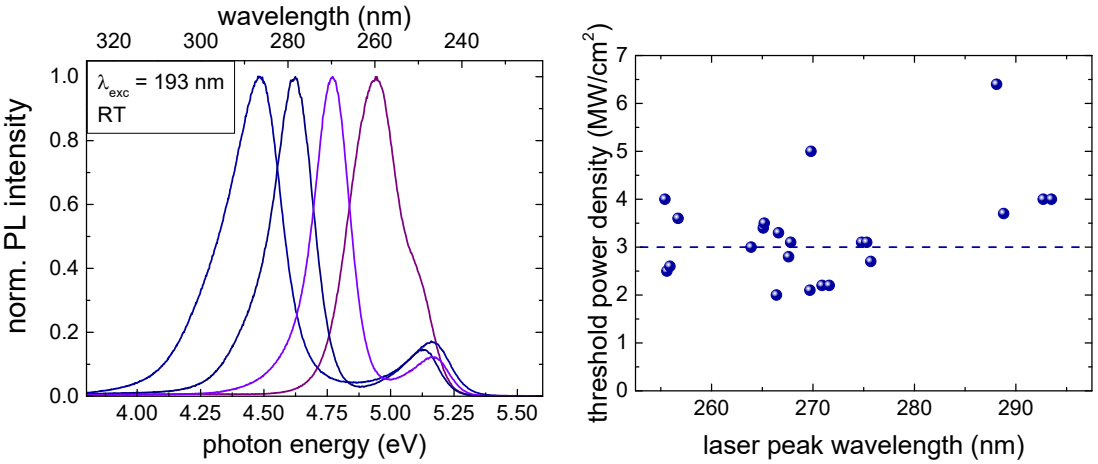

(a) photoluminescence (b) optically pumped threshold power

Figure 4.6 Room temeperature PL spectra collected from the heterostructure surface below threshold (measurement by C. Reich (TU Berlin)) (a) and optical threshold power density (b) of optically pumped lasers with different emission wavelength.

wavelengths of the laser's active region. Since the peak energies correlate with the energetic position of the carriers within the heterostructure this clearly illustrates the reduced potential barriers between quantum wells and barriers for decreasing emission wavelength.

Fig. 4.6(b) shows the threshold power density of optically pumped lasers with different emission wavelength. All laser heterostructures were grown on ELO AlN/sapphire templates with 0.2° off-cut, exhibiting a step-like morphology and resulting high scattering losses (see section 3.2). All lasers emitting between 250 nm and 280 nm exhibit laser threshold power densities around 3 MW/cm^2 within a certain scattering. The laser threshold of lasers emitting at 290 nm is slightly higher. Lowest threshold power densities were obtained for lasers emitting around 270 nm. The rather high level of the threshold values are mostly attributed to higher optical losses due to comparably rough surface morphologies (see section 3.2).

Fig. 4.7(a) shows optical gain spectra obtained by the VSLM (see section 2.2.1) of two optically pumped laser heterostructures emitting around 255 nm and 270 nm, respectively. Since both lasers are grown on wafers from the same batch of ELO AlN/sapphire substrates, the spectra exhibit comparable values of internal losses of $\sim 33\,\mathrm{cm}^{-1}$ mainly originating from scattering processes. Both lasers show an extinct gain peak reaching net gain values of $40\,\mathrm{cm}^{-1}$ and more depending on the pumping power. The inhomogeneous broadening is also comparable for both lasers. The

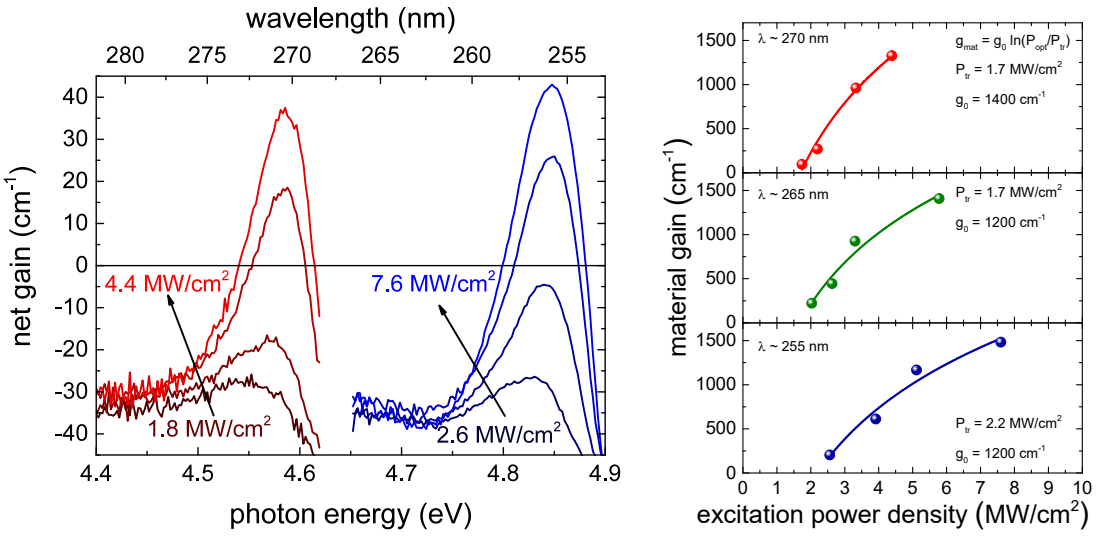

(a) gain spectra (b) peak material gain

Figure 4.7 Optical gain spectra (a) and peak material gain in dependance of the excitation power density (b) of optically pumped laser heterostructure with different emission wavelength.

FWHM of modal gain peaks of both lasers is in the range of 70 meV to 80 meV for excitation powers producing positive net gain. A major contribution to inhomogeneous broadening in ternary compound semiconductors is alloy fluctuation. For $Al_xGa_{1-x}N$ layers the maximum alloy broadening is expected for an Al content around 80% taking into account the maximum statistical disorder of the alloy at 50% Al content as well as the decreasing spatial distribution of excitons due to a decrease of the Bohr radius for increasing Al content [72,73]. Therefore, in the discussed spectral range alloy scattering would cause an increase of the inhomogenous broadenig with decreasing emission wavelengths, which cannot be observed. This observation is contrary to studies on the gain of InGaN based lasers emitting in the visible spectral range, where the gain profile changes drastically for increasing In content and emission wavelengths [74].
From the net gain spectra and the confinement factors (see Fig. 4.5(b)) the peak material gain can be derived. The increase of the material gain with pumping power can be well described by a logarithmic model with the gain coefficient g_0 and the transparency power density P_{tr} [15]. This is shown for three optically pumped lasers with different emission wavelength grown on the same ELO AlN/sapphire substrate in Fig. 4.7(b). The transparency pump power increases from 1.7 MW/cm^2 for 270 nm and 265 nm emission to 2.2 MW/cm^2 for 255 nm emission. The transparency pump power depends on three factors: The transparency carrier density of the active medium, which gives the number of carriers required to obtain population inversion, the effective carrier lifetimes in QWs and the efficiency for photogenerated carriers to reach the MQW. The transparency carrier density is determined by the density of states of the QWs at the transition peak energy. Calculations of the band structure and optical gain in AlGaN based MQW lasers show that with increasing Al content the density of low-lying states at the band edge increases, which increases the number of carriers needed for population inversion [2]. The carrier lifetime in the heterostructure is made up of the non radiative and radiative lifetimes. As the defect density in the different heterostructures is assumed to be same, also the non radiative lifetime are comparable. The radiative lifetime, on the other hand, depends on the overlap of the electron and hole wave function confined in the QW, which changes with the barrier height and quantum confined Stark effect and therefore with the Al content of the QWs. In this case this change is expected to be negligible, since the change of Al content is comparably small, the effect of increased confinement and quantum confined Stark effect are counteracting, and the contribution of radiative recombination to the total recombination is small. The effect of wave function overlap on the carrier density within the active region will be discussed in section 4.2.2 in more detail. The initial probability for carriers photogenerated in the upper waveguide layer

to relax into the QW is expected to be the same in all lasers. However, as the potential barrier between QW and quantum barrier decreases with increasing Al content thermal escape from the QWs of carriers is more likely for higher Al content QWs and therefore decreased emission wavelengths. This results in smaller fraction of photogenrated carriers participating to the population inversion. All described effects can result in increased transparency power density.
The effect discussed last has also a major effect on the gain coefficient. This parameter is a measure for how efficient additional carriers participate to the stimulated emission and describes the increase of material gain with increasing pump power [75]. The gain coefficient decreases from 1400 cm^{-1} for 270 nm emission to 1200 cm^{-1} for 265 nm and 255 nm emission, which can be explained by an increased number of carriers escaping the QW by thermal activation and recombining in the quantum barrier or waveguide layers. Like the variations in the laser threshold power density also the variation in transparency power density and the gain coefficient for different emission wavelengths are comparably small. However, the tendencies support the observation of the lowest laser threshold for laser emission around 270 nm. Therefore, the corresponding QW composition seems to be a reasonable starting point for further investigations and development.

4.2.2 Influence of quantum well number and thickness

Altering the QW number and QW thickness in the active region is a common way to push the characteristics of semiconductor based light emitters towards a certain target performance. In lasers, however, both parameters can hardly be discussed separately as both parameters have an effect on the confinement factor but also influence the device performance individually. For this reason, in this section the influence of the QW number is discussed for a fixed QW thickness before the influence of the QW thickness of a threefold QW is dealt with. Finally, laser heterostructures are studied for which both parameters are varied in order to keep the confinement factor constant.
In order to study the influence of the QW number on the laser threshold and the gain characteristics heterostructures emitting at $\sim$ 265 nm with QW numbers between one and ten are investigated by optical pumping. The volume of the overall waveguide is kept constant by adjusting the thickness of the single waveguide layer, so that the mode distribution within the laser is largely independent of the QW number.
Fig. 4.8(a) shows room temperature PL spectra of an optically pumped laser with a single QW (SQW) and a tenfold MQW active region. For both spectra emission from the active region as well as from the $Al_{0.70}Ga_{0.30}N$ quantum barriers and waveguide layers is clearly visible. However, considerable differences in the spectral distribution

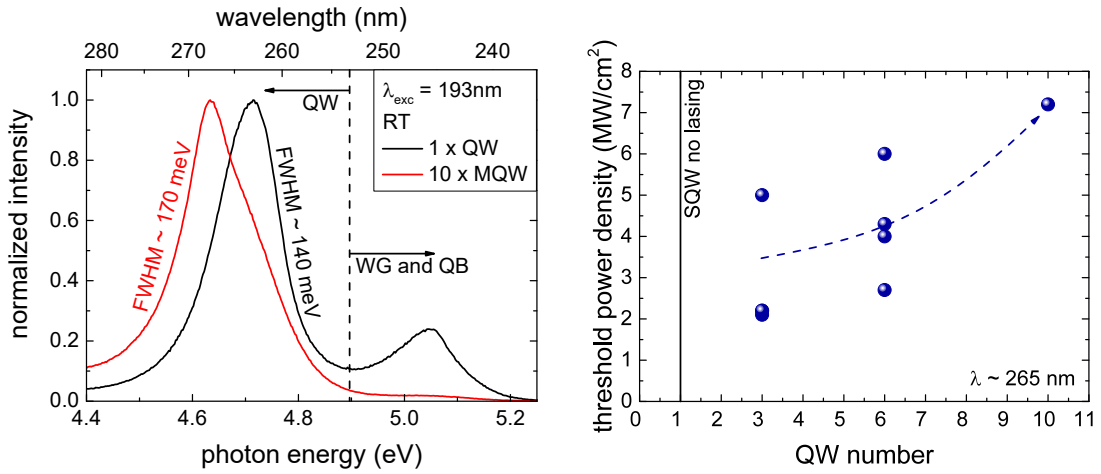

(a) photoluminescence (b) optically pumped threshold power

Figure 4.8 Room temperature PL spectra collected from the heterostructure surface below threshold (measurement by C. Reich (TU Berlin)) (a) and optical threshold power density (b) of optically pumped lasers with different QW number and constant QW thickness of 2.2 nm.

are obvious. Relative to the higher energetic emission from the quantum barriers and the waveguide layers the MQW emission is significantly stronger for the tenfold QW compared to the SQW active region. This can simply be explained by the increased total active volume for increased QW number, which leads to higher number of carriers combining in the QWs. Additionally, due to the fact that the total thickness is kept constant for the lasers with different QW number, the upper waveguide layer is thinner for heterostructures with higher QW number. This leads on one hand to a larger number of carriers relaxing into the QW before recombining in the waveguide layer and to larger number of carriers photogenerated directly in the QW due to higher intensities of the excitation at the depth of the QW on the other. Both effects result in higher number of carriers in the MQW.

Also the MQW peak itself shows differences in the room temperature PL spectra. The emission from the tenfold MQW is with a FWHM of ~ 170 meV somewhat broader than the emission from the SQW with a FWHM of ~ 140 meV and does not show a clear single peak shape. The peak maximum of the tenfold MQW is additionally slightly shifted to lower energies while the emission peak from the quantum barriers and the waveguide layers of both heterostructures match. However, a clear distribution of the tenfold MQW emission can be observed at the energetic position of the peak maximum of the SQW. The emission peak from the tenfold MQW is rather made up of several emission peaks originating from each QW which may slightly vary in QW composition or thickness. As a consequence the overall MQW peak is broad-

ened an inhomogeneous.

Except for the heterostructure with the SQW active region laser operation with facet emission is achieved for all lasers. The threshold power density increases from about 2 MW/cm^2 for the laser with threefold QW to 7 MW/cm^2 (see Fig. 4.8(b)). Obviously, the increased confinement factor for increased QW number is one effect which increases the net gain and can reduce laser threshold. The refractive index profile and calculated mode distribution in the optically pumped lasers with a SQW, threefold, sixfold and tenfold MQW active region is shown in Fig. 4.9(a). As the total waveguide thickness is the same in all lasers, the mode distribution is not affected by the choice of QW number although the average refractive index is slightly higher due to the higher refractive index of the QWs. The MQW active region is each positioned in the vicinity of the mode maximum. Therefore, the confinement factor increases from 1.8% for the SQW active region to 17.9% by approximately a factor of ten. At the same time, however, the carrier density decreases as for the same sheet carrier density in the active region the same number of carriers are distributed among a higher number of QWs. Since the generation of carriers is not homogenous throughout the heterostructure, the carriers are most likely not distributed homogeneously

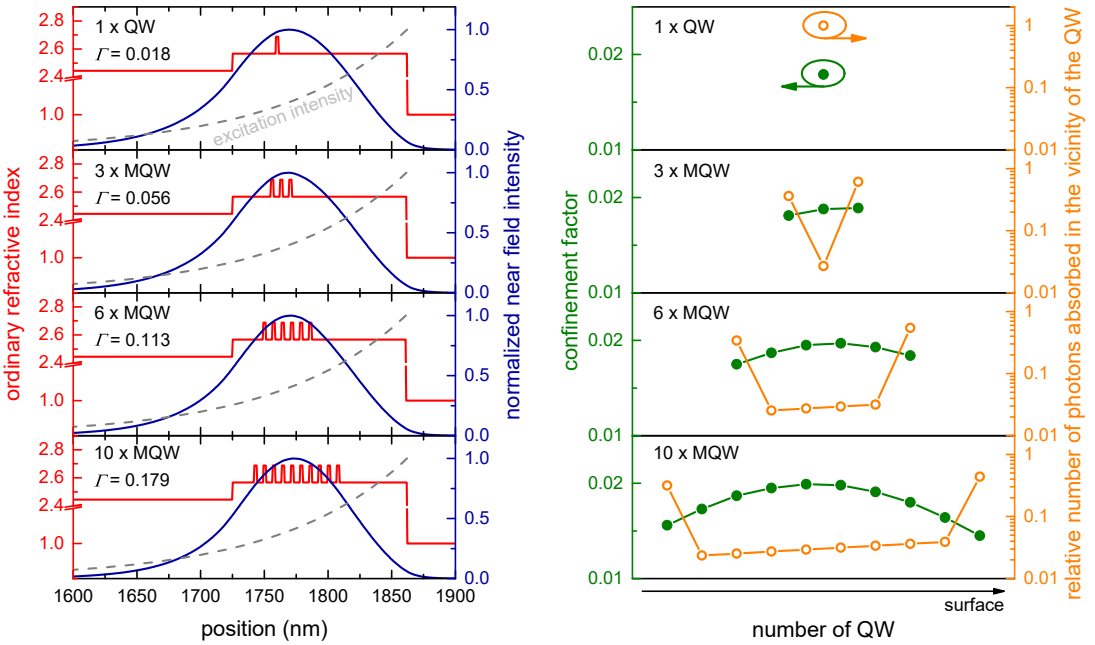

(a) mode distribution (b) confinement factor and absorbed photons

Figure 4.9 Refractive index profile and calculated mode distribution (a) and calculated confinement factor and estimated number of photons absorbed in the vicinity of each QW (b) in MQW laser heterostructures with different QW number.

among the QWs. Also shown in Fig. 4.9(a) is the intensity of the optical excitation normalized to the intensity penetrating the heterostructure at the crystal surface. The absorption coefficient for the pumping wavelengths of 193 nm is assumed to have a constant value of $1 \times 10^5\,\mathrm{cm}^{-1}$ throughout the heterostructure [76]. The absorption in the semiconductor crystal is mainly caused by the generation of free electron hole pairs. Therefore, the excitation intensity profile also represents the profile of the carrier generation rate. Most carriers are generated in the $Al_{0.80}Ga_{0.20}N$ waveguide layer and eventually relax into the QW if generated within the diffusion length of the QW. This diffusion length depends on the recombination rate of the layer, the mobility of the carrier and the temperature. Those parameters can significantly vary for different layers and are therefore not easy to evaluate, but expected to be the same in all lasers. The presence of radiative recombination in those layers, as seen in the PL spectra (compare Fig. 4.8(a)), is clear evidence that not all photogenerated carriers recombine in the MQW active region. Since the carrier generation profile is not constant throughout the heterostructure, the number of carriers initially relaxed into the QWs will not be equally distributed among the QWs. Additional effects like carrier diffusion and tunneling may also affect the carrier distribution and eventually flatten the carrier profile. In this case also the different mobilities of electrons and holes need to be considered. This, however, is not discussed in more detail at this point.

In Fig. 4.9(b) the relative number of photons absorbed in the vicinity of each QW is shown for the different laser heterostructures. The vicinity of the QW is defined as the QW itself with half of the thickness of the quantum barrier at each side plus the upper and lower waveguide layer for the topmost and last QW, respectively. Under the assumption that all generated carriers relax into the QWs, calculated photon numbers also represent the relative number of carriers in each QW. In case of the SQW active region all generated carriers have the chance to relax into the SQW and eventually recombine. When the QW number is increased, the carrier distribution becomes strongly inhomogeneous. The topmost QW is necessarily occupied by the largest number of carriers, because most carriers are generated in the upper waveguide layer. For each QW sandwiched between the topmost and last QW the volume of the available carrier reservoir and therefore the carrier density is significantly smaller. As discussed above those QWs may be additionally be filled by diffusion and tunneling processes, which are not taken into account. The carrier density decreases exponentially with deeper QWs following the exponential decrease of the generation rate. The middle QWs, however are those, which have the highest confinement factor (also shown in Fig. 4.9(b)) and are therefore capable of producing the highest modal

gain or losses in the laser heterostructure. For the last QW, on the other hand, the volume from which carriers may relax into the QW is again larger and consequently the carrier density higher but still not reaching the occupation of the topmost QW. As a consequence, for the outer QWs population inversion and transparency can be obtained for pump power densities at which the middle QWs are still absorbing and producing significant optical losses, which hinder laser operation.
All three effects, discussed above, i.e. increased confinement factor for increased QW number, decreased carrier density in the active region for a given sheet carrier density for increasing QW number, and inhomogeneous occupation of the QWs for active regions with more than one QW affects the laser threshold and net optical gain. In order to gain a better understanding of the influence of the QW number in the MQW active region on the optical gain characteristics of optically pumped MQW lasers, the internal optical losses and the differential gain are extracted from optical gain spectra obtained by the VSLM (see Fig. 4.10). The differential gain describes the increase of the peak net gain with increasing power in a linear model, which can be very well applied within a certain pumping range. It is a suitable parameter in order to link the net gain directly to the pump power. However, it needs to be stated that this parameter leaks physical justification as the increase of gain with carrier density for QW based active regions is expected to be logarithmic [15]. The internal losses in the laser heterostructures increase with increased QW number. While for lasers with active region containing one, three, and six QWs the losses are all in the range of 30 cm^{-1}, which is comparable to the losses of lasers with comparable morphology, discussed above, the losses for the tenfold MQW active region increase to about 70 cm^{-1}. The differential gain shows a comparable value at $\sim 10\,cm^{-1}/MW\,cm^{-2}$ for threefold and sixfold QWs and drops to about half its value for the tenfold MQW and even lower values for the SQW. These results support the trend of the increase of laser

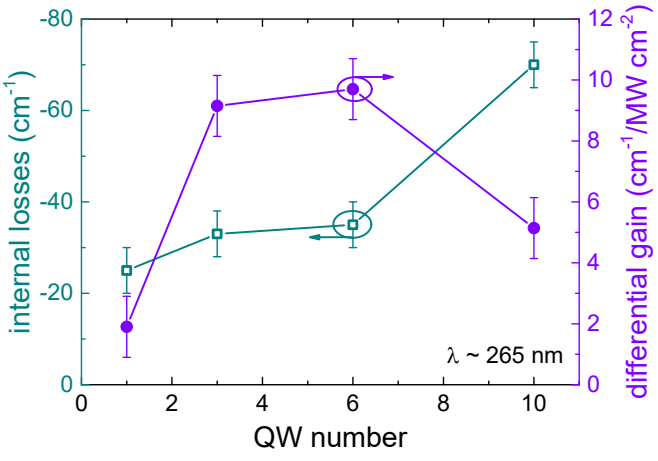

Figure 4.10 Internal losses and differential gain of optically pumped lasers determined from optical gain spectra.

threshold with increasing QW number. For the laser heterostructure with an SQW active region no laser operation was achieved, which is consistent with observation of very low differential gain. It seems that the confinement factor of less than 2% is too low to produce sufficient modal gain. Additionally, the upper waveguide layer is in this structure thicker than any of the others, since the overall volume of the active region is for the SQW the smallest, which may result in less efficient pumping of the active region due to increased recombination in the thick $Al_{0.80}Ga_{0.20}N$ layer. The lasers with a threefold and sixfold MQW active regions show comparable modal losses and differential gain and also exhibit threshold power densities in the same range. This suggests that either the advantage of higher modal gain for the sixfold MQW is compensated by lower carrier densities for the same pumping power or that for both lasers the modal gain is only produced by the outer QWs, where carrier densities are comparable due to the inhomogeneous carrier distribution within the MQW. When the QW number is further increased to ten, laser operation is almost completely inhibited and only observed for high pumping powers, which seems to be a result of the high internal losses originating from the inhomogeneous broadening of the MQW emission as also discussed for the PL data above. The differential gain is also smaller, which can be a result of reabsorption of inefficiently pumped QWs, pointing out that the modal gain can hardly overcome the increased losses. Also non radiative recombination at interfaces may play a role due to higher number of interfaces for active regions with more QWs [77].

The presented results suggest that best performance can be obtained for lasers with active regions consisting of a QW number in the range of three in matter of low laser thresholds, reduced modal losses, and high differential gain. This is consistent with studies performed on GaN based laser diodes emiting in the visible spectral range [78]. For current injection laser diodes emitting in the deep UV spectral range, where drift processes are dominant for carrier transport and electrons and holes are injected into the active regions from opposite sides, carrier distribution within the active region may differ from the optically pumped lasers. Numerical calculations of the carrier distribution within UV LEDs show that due to the different mobility of electron and holes the QW closest to the p-side has the highest electron as well as hole concentration [59]. Therefore, the MQW active region for deep UV laser diodes needs to be evaluated in current injection experiments in future, for which the present results can provide a starting point.

The volume of the active region can additionally be varied by altering the QW thickness. In order to investigate the influence of QW thickness on the laser performance four optically pumped laser with a threefold MQW with QW thicknesses of 0.6 nm,

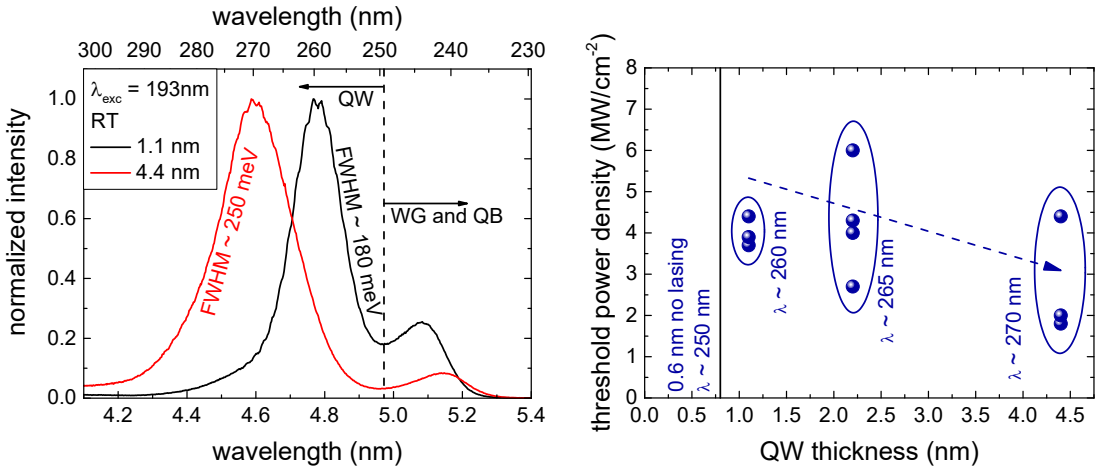

(a) photoluminescence (b) optically pumped threshold power

Figure 4.11 Room temperature PL spectra collected from the heterostructure surface below threshold (measurement by C. Reich (TU Berlin))(a) and optical threshold power density (b) of optically pumped lasers with threefold MQW active region with different QW thicknesses.

1.1 nm, 2.2 nm, and 4.4 nm were studied. The QW composition was chosen for emission around 265 nm depending on the QW thickness with $Al_{0.70}Ga_{0.30}N$ quantum barriers. The active region is embedded in the same $Al_{0.70}Ga_{0.30}N/Al_{0.80}Ga_{0.20}N$ waveguide structure discussed above. Fig. 4.11(a) shows the normalized room temperature PL spectra of the laser heterostructures with 1,1 nm and 4.4 nm thick QWs for comparison. Both spectra exhibit a clear signal from recombination in the MQW and the $Al_{0.70}Ga_{0.30}N$ quantum barrier or waveguide layers as well. The QW emission is shifted towards higher energies for thinner QWs due to higher confinement energies. Relative to the QW emission both heterostructures exhibit, the higher energy emission peak not originating from MQW emission is stronger for thinner QWs, which can be attributed to the large total volume of active regions with thicker QWs equivalent to the increase of active volume by increased QW number, discussed above. Also, the FWHM of the QW emission peak from the thicker QW is with 250 meV significantly broadened compared to the thin QW with 180 meV (140 meV and 115 meV at liquid helium temperature, spectra not shown). A broadening of the emission peak with increasing QW thickness has already been discussed in literature for $Al_xGa_{1-x}N$ with Al contents up to 0.25 [79] and is usually attributed to a stronger contribution of the alloy fluctuation for thicker QWs.

The threshold power density of the optically pumped lasers decreases for increasing QW thickness, while for lasers with 0.6 nm QWs no laser operation was achieved even for high pumping (see Fig. 4.11(b)). At the same time the emission wavelength in-

creases for increasing QW thickness due to the decreased confinement energy, which is consistent with the observations from the PL experiments performed below threshold. The reduction of the laser threshold with increasing QW thickness can easily be explained by the increase of the confinement factor from 2 % for 0.6 nm thick QWs to more than 11 % for 4.4 nm thick QWs. In case of increased QW numbers this effect was compensated by decreased carrier concentrations for the same sheet carrier density and inhomogeneous carrier distribution among the QWs. For MQW active region with identical QW number but different QW thickness, on the other hand, the number of carriers in each QW is comparable for all lasers. However, the QW thickness can significantly affect the radiative recombination processes within the QW. Fig. 4.12 shows the calculated band diagram and electron and hole wave functions of the ground state for the optically pumped lasers with different QW thickness (model by M. Guttmann (TU Berlin)). For illustration issues the zero level of each wave function is positioned at the calculated energy level of the respective ground state. With increasing thickness the carriers are less confined and drop further into the QWs towards the band edge resulting in lower transition energies. Additionally, the influence of the QCSE increases, which leads to a further reduction of the energy state of the carriers. This effect is more pronounced for the holes as they are stronger localized within the potential dip created by polarization induced band bending due to larger effective masses. The QCSE leads additionally to a spatial separation of electron and holes and a reduction of the wave function overlap of the carriers (also shown

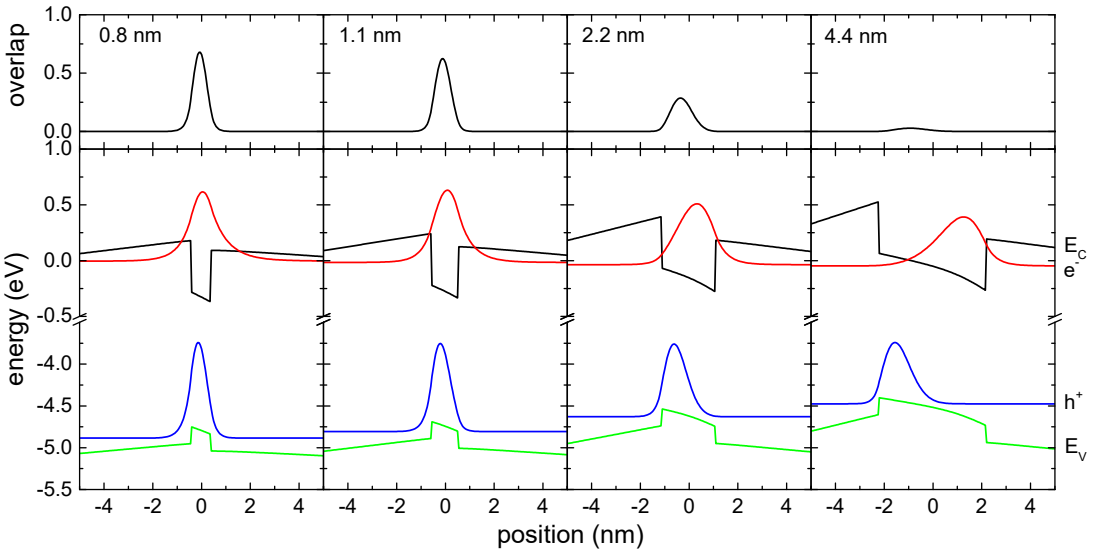

Figure 4.12 Calculated band diagram and electron as well as hole wave functions for QWs with different QW thicknesses for emission in the range of 265 nm. (model by M. Guttmann (TU Berlin))

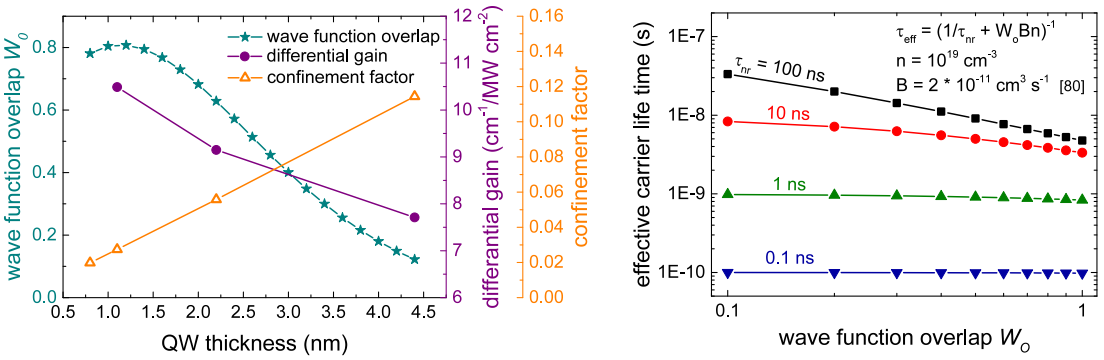

Figure 4.13 Calculated wave function overlap W_0, confinement factor, and determined differential gain (a) and calculated effective carrier life times in the QWs in dependance of the wave function overlap (b) of optically pumped lasers with a threefold MQW active region with different QW thicknesses.

in Fig. 4.12). The wave function overlap is an important parameter for the transition matrix element and affects the radiative recombination rate and the material gain. The calculated wave function overlap drops from 0.8 for a QW thicknesses in the range of 1.0 nm to 1.5 nm to almost 0.1 for 4.4 nm thick QWs (see Fig. 4.13(a)). For QW thicknesses smaller than 1.0 nm the overlap decreases again. In this region the increasing effect of confinement is dominant. As the energy state shifts towards the band edge the wave function delocalizes with a pronounced tail into the barriers. Due to the different effective masses of electron and hole this effect sets in earlier for electrons and the tails of the electron wave function penetrating the barrier only have a small overlap with the hole wave function.

The wave function overlap linearly scales the radiative recombination rate. Fig. 4.13(b) shows effective carrier life times calculated for a carrier density of $10^{19}\,\mathrm{cm}^{-3}$ according to a rate equation for linear and square terms for different non radiative carrier life times in dependance of the wave function overlap W_O. For the calculation a fixed B parameter of $2 \times 10^{-11}\,\mathrm{cm}^3\,\mathrm{s}^{-1}$ [80] was chosen giving the efficiency of the radiative recombination. The longer the non radiative life time the higher the effect of radiative recombination processes on the effective carrier life time. Therefore, also the wave function overlap in the QW can only influence the effective carrier life time for long non radiative life times. For shorter life times of 1 ns and less, as expected for Al rich QWs emitting in the deep UV spectral range [81–83], radiative recombination cannot significantly affect the total life times and therefore the carrier densities as described for GaN based QWs emitting in the blue-violet spectral range for which higher radiative and lower non radiative recombination rates can be assumed [84]. In

fact, the opposite effect of decreasing carrier life times with increasing QW thickness was observed for AlGaN QWs [85], which is attributed to an increased influence of localization of carriers due to potential fluctuation for thinner QWs and resulting lower non radiative recombination rates.
The differential net gain, determined by optical gain data obtained by the VSLM, decreases with increasing QW thickness (see Fig. 4.13(a)) following the trend of the wave function overlap, which can be explained by the decreased transition matrix element and resulting reduction of material gain. Also the increased inhomogeneous broadening, discussed for the PL data may play a role. However, this effect is compensated by the increased confinement factor increasing the modal gain.
In order to separate the effect of increasing confinement factor from the influence of the QW thickness on the recombination processes, optically pumped lasers emitting at 240 nm with 1.5 nm, 3.0 nm, and 6.0 nm thick QWs with 8 nm thick $Al_{0.80}Ga_{0.20}N$ quantum barriers, in which the confinement factor is kept constant by changing the QW number from four to two and one, respectively, are studied. The active region is embedded in an $Al_{0.80}Ga_{0.20}N$ waveguide with a total thickness of 80 nm. The refractive index contrast to the underlying AlN and topmost 20 nm thick AlN cap layer provides mode confinement. The laser heterostructures are grown on two different ELO AlN/sapphire templates with 0.1° and 0.2° miscut and different threading dislocation density and surface morphology accordingly (compare section 3.2.2). In general the threshold power density of laser heterostructures grown on templates with 0.1° miscut is higher than of lasers grown on templates with 0.2° miscut, which is in accordance to previously discussed results. Fig. 4.14 shows the dependency of the laser threshold on the QW thickness or QW number. The laser threshold power for the lasers with a 3.0 nm thick double QW and the 6.0 nm thick SQW active region are in the same range of 2.0 MW/cm^2 or 1.5 MW/cm^2, depending on the used AlN/sapphire template. The laser threshold of the lasers with 1.5 nm thick fourfold MQW active region, however, is slightly increased reaching power densities of more than 3 MW/cm^2, which can not be explained by lower modal gain due to higher confinement factors. The trend, however, is comparable to the one for different QW number and different altering confinement factors observed for lasers with longer wavelength emission discussed above. The behavior can therefore be explained by an increase of non radiative recombination at interfaces, which increases for higher number of interfaces and consequently higher QW number, or increasingly inhomogeneous carrier distribution among the QW for higher QW numbers.
In conclusion, for optically pumped lasers an active region consisting of a threefold MQW with QW thicknesses of more than 4 nm seem to be preferable in order to

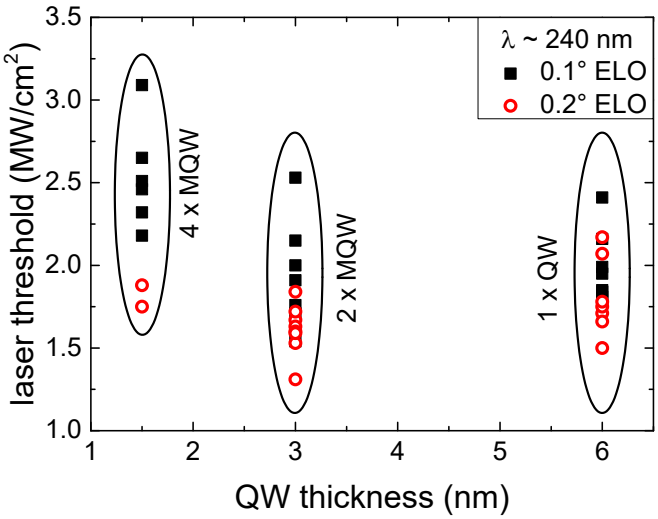

Figure 4.14 Threshold power density of optically pumped lasers with different QW thickness and number emitting around 240 nm. The confinement factor is kept constant by adjusting the QW number.

achieve low threshold power densities as they combine low optical losses, high confinement factor, and comparably homogeneous carrier distribution among the single QWs in the MQW. However, for current injection laser diodes different effects have to be taken into account. As electron and holes injected through contacts positioned on opposite sides of the heterostructure and carrier drift is involved the carrier distribution profile may for current injection devices significantly vary from the heterostructures under optical pumping. Also, additional optical losses originating from modal absorption in doped layers or at the metal contacts have to be overcome in order to achieve lasing (see section 5.2). This makes differential gain more important than for optically pumped lasers with moderate modal losses. The optimal active region design for deep UV laser diodes has to be determined by current injection experiments and sophisticated device modelling. However, the present results from optically pumped lasers give a better inside in gain and loss processes in the active region which is essential for further development.

Chapter 5

Towards current injection UV laser diodes

In chapters 3 and 4 the influence of material quality of the heterostructure as well as the design of the active region on the laser threshold and optical gain was discussed. It was shown, that the use of AlGaN based multiple quantum well active regions embedded in an $Al_xGa_{1-x}N/Al_yGa_{1-y}N$ separate confinement heterostructure can provide sufficient material gain as well as optical confinement in order to achieve optically pumped lasing.

In order to realize deep UV current injection lasing various technological and physical challenges have to be addressed. For the high carrier densities necessary to reach transparency condition and eventually lasing, highly conductive n- as well as p-AlGaN layers with high aluminum mole fractions are needed. This, however, is due to the large ionization energies especially for magnesium acceptors in AlGaN with high aluminum mole fractions a critical issue. One approach suggested in literature to overcome the high activation energy is to use a periodic structure of Mg-doped $Al_xGa_{1-x}N/Al_yGa_{1-y}N$ layers instead of a single thick AlGaN layer. The suitability of this approach for current injection in high optical confinement heterostructures will be discussed in section 5.1.

From blue-violet emitting devices it is known, that magnesium acceptors can introduce additional absorption in GaN, which dramatically increases optical losses and can inhibit efficient lasing. In section 5.2 the influence of magnesium acceptors on optical losses in AlGaN based waveguide structures for deep UV lasing will be discussed. By quantifying the magnesium absorption it is possible to perform reliable calculations of modal losses in deep UV separate confinement structures and suggest heterostructure designs which combine high optical confinement, high modal gain, and efficient carrier injection.

5.1 Carrier injection into separate confinement heterostructures

A separate confinement heterostructure has already been introduced for optically pumped lasing in section 2.1. In this case the mode guiding is given by the refractive index contrast between the $Al_{0.70}Ga_{0.30}N$ waveguide layer and the $Al_{0.80}Ga_{0.20}N$ cladding layer on the substrate side of the waveguide. In contrast, on the surface side of the waveguide the high refractive index contrast between the $Al_{0.70}Ga_{0.30}N$ waveguide layer and the surrounding air ($n \approx 1.0$) ensures high mode confinement. This results with properly chosen waveguide layer thicknesses in high confinement factors Γ of more than 5 %.

In order to design a heterostructure for current injection lasing, several elements have to be added to the separate confinement heterostructure designed for optically pumped lasing (see Fig. 5.1). Since the required contact metals are highly absorptive for the laser mode [86] the n- as well as the p-contact need to be spatially well separated from the active region. In case of the n-contact this is not a critical issue, because the used sapphire or AlN substrates are isolating and the n-contact material is deposited after mesa etching alongside the cavity. The p-contact on the other hand is for conventional gain-guided and index-guided device structures positioned on the crystal surface above the cavity. Therefore, an additional cladding layer is embedded between the active region and the contact. For better contact resistance and reduced electron leakage a p-GaN contact layer and electron blocking layer (EBL) is introduced equivalent to LED fabrication [87–89].

Fig. 5.2 shows refractive index profiles and mode calculations for 270 nm emission for an exemplary laser diode structure with a threefold $Al_{0.42}Ga_{0.58}N/Al_{0.70}Ga_{0.30}N$ multiple quantum well, 6 nm thick AlN EBL, 25 nm thick upper $Al_{0.70}Ga_{0.30}N$ up-

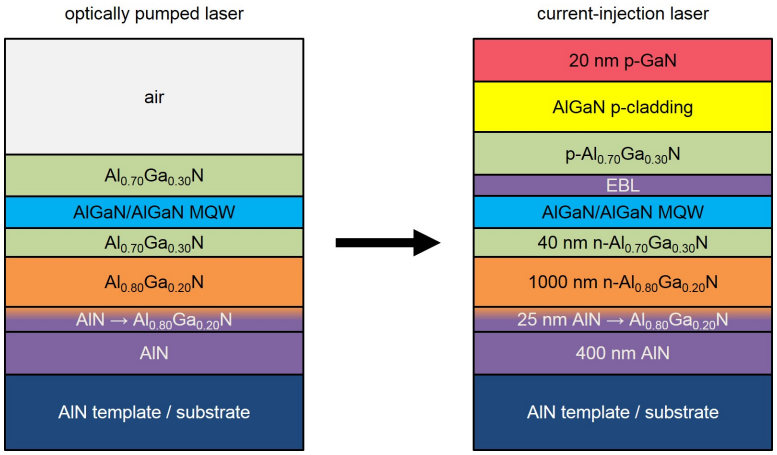

Figure 5.1 Schematic of a heterostructure used for optically pumped lasing and current injection lasing

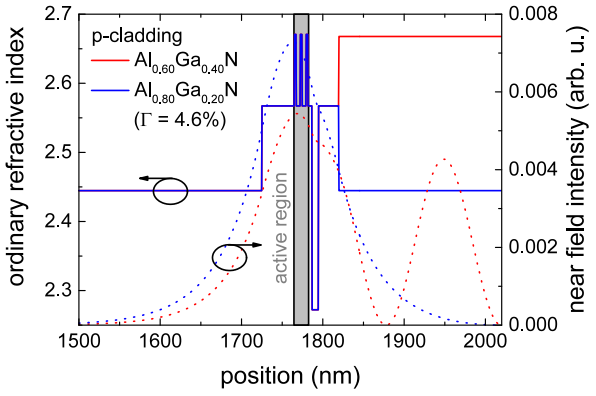

Figure 5.2 Refractive index and calculated mode profile of laser diodes at 270 nm with p-cladding layer compositions higher (blue) and lower (red) than the $Al_{0.70}Ga_{0.30}N$ waveguide layers. For the laser diode with lower p-cladding layer composition the second order mode is shown, as it has a higher confinement than the fundamental mode. [90]

per waveguide layer and 200 nm upper cladding layer with an aluminum composition of 60 % and 80 %, respectively. The refractive index profile follows the composition profile as expected with the highest refractive index for the $Al_{0.42}Ga_{0.58}N$ quantum wells and the lowest for $Al_{0.80}Ga_{0.20}N$ cladding layers and AlN EBL. This results in a well confined mode with a confinement factor of $\Gamma = 4.6\,\%$ for the symmetric $Al_{0.70}Ga_{0.30}N/Al_{0.80}Ga_{0.20}N$ waveguide structure. The refractive index of an $Al_{0.60}Ga_{0.40}N$ upper cladding layer, however, is only slightly lower than the one of the the quantum wells and considerably higher than the one of the $Al_{0.70}Ga_{0.30}N$ waveguide layers. As a result the fundamental mode in this structure is guided within the $Al_{0.60}Ga_{0.40}N$ cladding layer instead of the intentional waveguide, while the second order mode has a considerably overlap with the active region (shown in Fig. 5.2). However, a large contribution of the mode still overlaps with the absorptive $Al_{0.60}Ga_{0.40}N$ layer resulting in high modal losses. This clearly illustrates the need for high aluminum content $Al_xGa_{1-x}N$ p-cladding layers ($x > 0.7$). The influence of the waveguide design on the confinement factor, optical losses, and injection efficiency is discussed in section 5.2.2 in detail.

For carrier injection the high aluminum content cladding layers need be doped. For ionization energies of silicon donors in $Al_xGa_{1-x}N$ layers quite constant values of 15 meV have been reported for a composition range of $0 \leq x \leq 0.8$ and increasing values for higher aluminum content up to 255 meV for AlN [91]. For $Al_{0.80}Ga_{0.20}N$:Si layers resistivities as low as 0.026 Ωcm with carrier concentrations up to $1.5 \times 10^{19}\,cm^{-3}$ have been reached [92]. However, the ionization energies of magnesium acceptors in AlGaN increase with increasing aluminum content and are considerably higher (see Fig. 5.3(a)). The high ionization energies of more than 400 meV for the composition of interest drastically limit the hole concentration in the AlGaN:Mg layers. The calculated carrier concentration in an $Al_{0.80}Ga_{0.20}N$:Mg layer in dependance of the

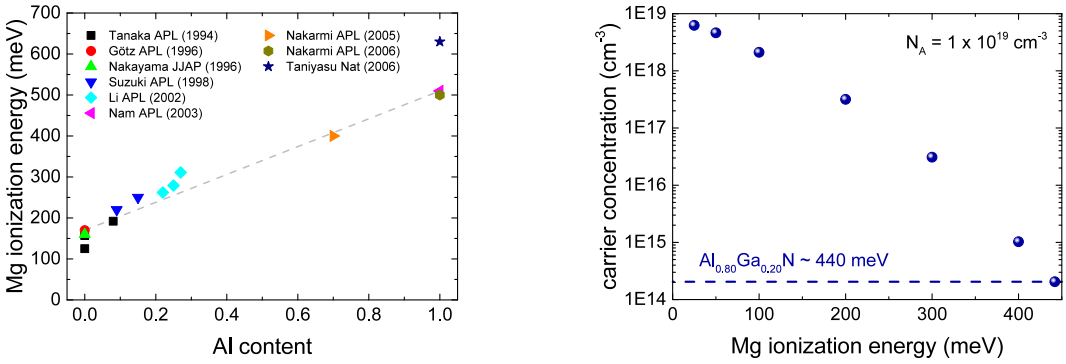

(a) Mg ionization energy in AlGaN

(b) calculated hole concentration

Figure 5.3 Reported values of ionization energies of magnesium acceptors in $Al_xGa_{1-x}N$ layers [93–101]. Dashed line: Guide to the eye from 170 meV for GaN to 510 meV for AlN layers (a). Calculated hole concentration in an $Al_{0.80}Ga_{0.20}N$:Mg layer in dependance of the ionization energy for an acceptor concentration of N_A=$1 \times 10^{19}\,cm^{-3}$ at room temperature (b).

ionization energy for an acceptor concentration of $10^{19}\,cm^{-3}$ is shown in Fig. 5.3(b). Calculated carrier concentrations as well as band structures discussed in this chapter were simulated using the SiLENSe software package [17]. An $Al_{0.80}Ga_{0.20}N$ layer with the predicted ionization energy in range of 440 meV would exhibit carrier concentrations in the range of $2 \times 10^{14}\,cm^{-3}$ which is five orders of magnitude lower than the electron concentration in silicon doped AlGaN layers of the same composition. This inhibits efficient hole injection into the active region and increases operation voltage, which causes device heating leading to reduced radiative recombination rates.

5.1.1 Magnesium ionization in $Al_xGa_{1-x}N/Al_yGa_{1-y}N$ short period super lattices

One approach to circumvent the high ionization energy in high aluminum content AlGaN layers is to grow a periodic sequence of thin magnesium doped AlGaN layers with alternating composition. The use of such a so called short period super lattice (SPSL) in order to achieve high hole concentrations in AlGaN has first been suggested and calculated by Schubert et al. [102] and later experimentally proven by different groups [103–107]. Since the carrier concentration within an SPSL can be significantly higher compared to thick layers this corresponds to a reduction of the effective ionization energy. Fig. 5.4 shows values for the effective ionization energy versus the average aluminum content of the SPSL published by different groups. Since the performance of the SPSL strongly depends on geometry factors (i.e. period, composition

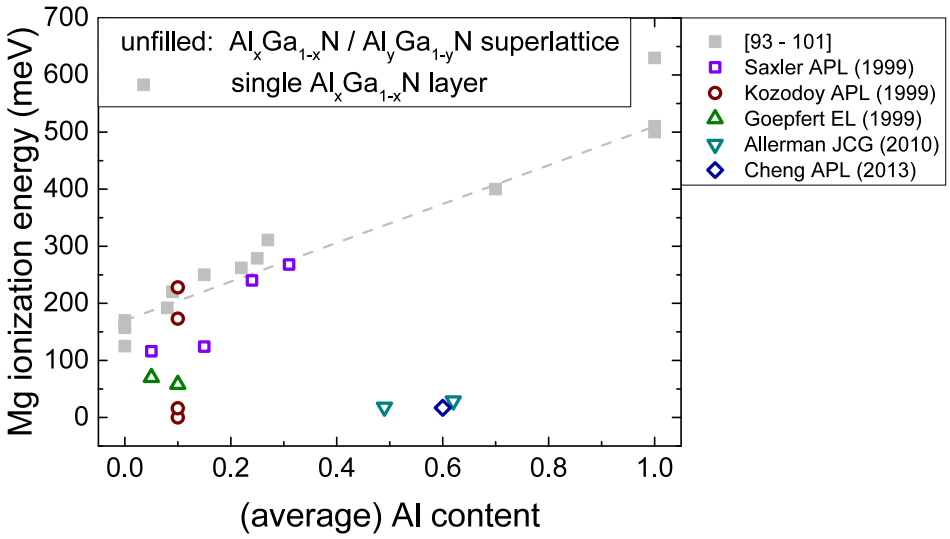

Figure 5.4 Reported values of effective ionization energies of magnesium acceptors in $Al_xGa_{1-x}N/Al_yGa_{1-y}N$ super lattices (unfilled symbols). Grey symbols: Reported values for magnesium activation in single thick $Al_xGa_{1-x}N$ layers for comparison. [103–107]

contrast), the reported values can scatter over a quite broad energy range. However, effective activation energies as low as 17 meV were reported for AlGaN SPSLs with an average aluminum content of 60 % [107].

The impact of the alternating material composition in an SPSL on the activation of acceptors can be best understood by taking a look at the band structure. Fig. 5.5(a) shows the calculated valance band edge and the acceptor energy level within the band gap for a bulk $Al_{0.80}Ga_{0.20}N$:Mg and different $Al_{0.90}Ga_{0.10}N$:Mg/$Al_{0.70}Ga_{0.30}N$:Mg SPSLs with acceptor concentrations of $10^{19}\,cm^{-3}$. The Fermi level is located at zero energy each. On the topmost diagram the band structure for thick $Al_{0.80}Ga_{0.20}N$:Mg with constant composition is shown. The magnesium acceptor is separated by the ionization energy $E_A = 440$ meV from the valance band and is located within the band gap. The Fermi energy ($E = 0$ eV) is located between acceptor level and valence band edge close to the acceptor level as expected in the freeze-out regime. Because of the high ionization energy thermal activation of acceptors is very unlikely, resulting in low hole concentrations of $2 \times 10^{14}\,cm^{-3}$ throughout the layer (see Fig. 5.5(b)). The second graphs from the top show the situation for $Al_{0.90}Ga_{0.10}N/Al_{0.70}Ga_{0.30}N$ SPSL with a period of 5 nm without any polarization fields included. The valance band edge and the acceptor level follow the compositional profile of wells and barriers forming a rectangular function. The Fermi level in thermodynamic equilibrium, however, needs to be constant throughout the crystal at an averaged energy level. As a consequence the Fermi level is in the barrier region significantly closer to the

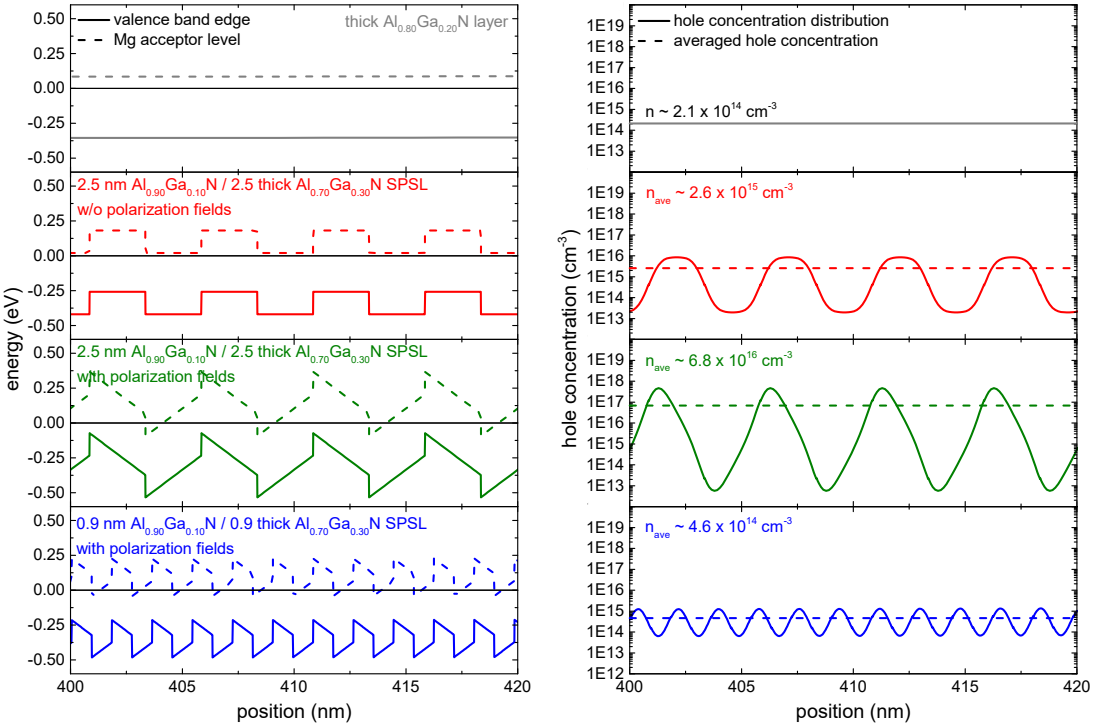

(a) valance band and acceptor level

(b) carrier concentration

Figure 5.5 Calculated valence band edge and magnesium acceptor level (a) and resulting hole concentration (b) in $Al_{0.80}Ga_{0.20}N$:Mg bulk layer and $Al_{0.90}Ga_{0.10}N$:Mg/$Al_{0.70}Ga_{0.30}N$:Mg SPSLs with different period and with and without polarization fields. The acceptor concentration is $10^{19}\,cm^{-3}$.

acceptor level than in the wells. The spacing between Fermi level and acceptor level is in the barriers also closer compared to the thick $Al_{0.80}Ga_{0.20}N$ layer. As a result more acceptors are ionized. The in the barriers activated free holes tend to relax into the wells with lower energies forming an inhomogeneous carrier distribution throughout the SPSL with high hole concentration in the wells and depleted barriers (see Fig. 5.5(b)). The averaged hole concentration, however, is with $3 \times 10^{15}\,cm^{-3}$ one order of magnitude higher than in the bulk layer. This effect is additionally enhanced by the presence of polarization fields at the heteorstructure interfaces within the SPSL. This case is shown for the $Al_{0.90}Ga_{0.10}N/Al_{0.70}Ga_{0.30}N$ SPSL with a period of 5 nm in the third graphs of Fig. 5.5 (polarization calculated according to Bernardini et al. [108]). The polarization field induced band bending results in a further reduced spacing between Fermi level and acceptor level and even regions at heterostructure interfaces where the Fermi level is above the acceptor level, which means that all acceptors are ionized. The resulting periodic hole concentration has an average value of $7 \times 10^{16}\,cm^{-3}$ which is a further increase of more than one order of magnitude.

Since the polarization field induced bend bending within the SPSL depends on the spacing between the interfaces it is worth taking a look at different SPSL periods. The bottommost graphs in Fig. 5.5 show the valance band profile and hole concentration for a $Al_{0.90}Ga_{0.10}N/Al_{0.70}Ga_{0.30}N$ SPSL with a period of 1.8 nm and polarization fields included. The smaller band bending leads to smaller areas in which all acceptors are ionized and resulting lower hole concentration. This cannot be compensated by the effect that for the same SPSL length the SPSL with smaller period has a larger number of areas with high hole concnentration compared to an SPSL with larger period. In fact, the averaged hole concentration for the SPSL with 1.8 nm period is with $5 \times 10^{14}\,\mathrm{cm}^{-3}$ more than two orders of magnitude lower than the one in the SPSL with 5 nm period. This clearly illustrates that the SPSL geometry is important for the SPSL characteristics. Another important parameter which has not been considered so far is the band offset between SPSL barrier and well which also influences the polarization induced band bending and hence affect carrier densities.

Although the use of an SPSL is favorable for increased carrier concentrations, the periodic carrier distribution and the internal potential barriers within an SPSL might inhibit the vertical carrier transport through the SPSL. As the band bending increases the holes are more localized in the potential dips at the heterostructure interfaces and as the period of the SPSL increases those hole accumulations are more separated. Additional to the conventional thermionic excitation, however, different transport mechanisms are possible in SPSL structures. If barriers are thin enough the hole wave functions of localized holes eventually overlap forming subbands of allowed states within in SPSL barriers. The transmission of carriers through the SPSL can then be

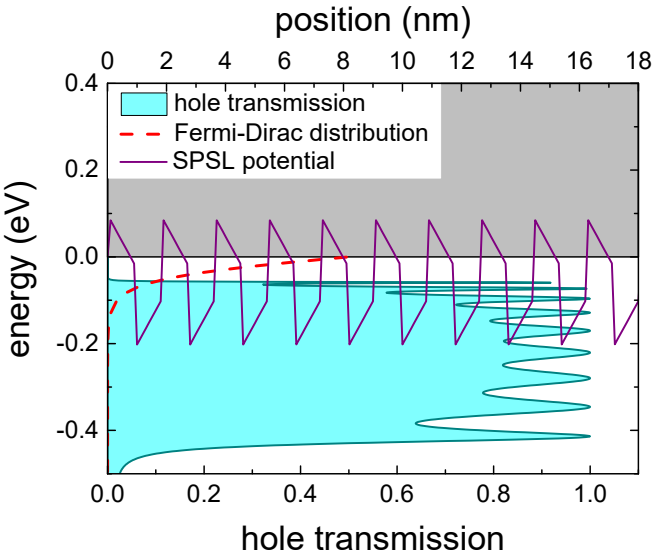

Figure 5.6 Calculated hole transmission of an $Al_{0.90}Ga_{0.10}N/Al_{0.70}Ga_{0.30}N$ SPSL with a period of 1.8 nm (model by Martin Guttmann (TU Berlin)).

calculated by the transfer matrix method [109]. The calculated transmission of an $Al_{0.90}Ga_{0.10}N/Al_{0.70}Ga_{0.30}N$ with a period of 1.8 nm is shown in Fig. 5.6 for a split-off hole with the effective mass linearly interpolated between $m_h^* = 0.15$ for GaN and $m_h^* = 0.27$ for AlN (model by Martin Guttmann (TU Berlin)). A transmission band is formed in a region where classical transport through the barriers would be impossible. The width and position of this band depends on the period of the SPSL and the offset between wells and barriers.
In order to provide an qualitative value for the hole transmission, the hole transmission factor η_{tr} is introduced:

$$\eta_{tr} = \frac{\int_E T(E) \cdot n_{FD}(E) \cdot dE}{\int_E n_{FD}(E) \cdot dE}, \qquad n_{FD}(E) = \frac{1}{exp\left(\frac{E}{k_b T}\right) + 1} \tag{5.1}$$

$T(E)$ is the calculated transmission spectrum, n_{FD} the Fermi-Dirac distribution, and $k_B T$ represents the thermal energy. The transmission factor describes the overlap between the transmission spectrum and the Fermi-Dirac distribution. The Fermi-Dirac distribution gives the occupation probability (see Fig. 5.6). This way the transmission is weighted by the energetic position of holes and can provide qualitative expression for the hole transport. The Fermi energy is here artificially set to $E_F = 0$ eV. In a real crystal it depends on the doping and the surrounding material. For calculations with a more quantitative value additional considerations have to be done. In order to determine the exact energetic position of the holes, the density of states for holes in the SPSL structure has to be calculated. However, this is at the current state not yet included in the model. Also, external fields are not yet considered. However, the transmission factor can be used in order to qualitatively compare SPSLs with different geometries regarding their hole transmission.
In Fig. 5.7 the calculated hole concentrations and transmission factors for AlGaN:Mg SPSLs with an average aluminum content of 80 % for different SPSL periods and well and barrier compositions are shown. As discussed before, with increasing SPSL period the polarization field induced band bending increases favoring acceptor ionization. This leads to a significant increase of average hole concentration with increasing SPSL period. The carrier concentration with a period of 10 nm is four orders of magnitude higher than the one in a single $Al_{0.80}Ga_{0.20}N$ layer (SPSL period = 0 in Fig. 5.7) with homogeneous composition. At the same time the transmission factor decreases sev-

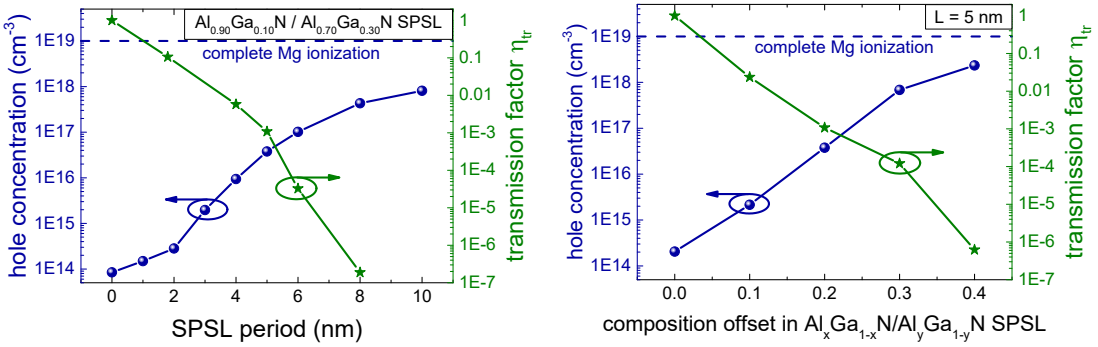

(a) hole concentration vs. SPSL period

(b) hole concentration vs. SPSL composition offset

Figure 5.7 Calculated hole concentration in and transmission factors (model by Martin Guttmann (TU Berlin)) of $Al_{0.90}Ga_{0.10}N/Al_{0.70}Ga_{0.30}N$ SPSLs in dependance of the SPSL period (a) and in AlGaN SPSLs with a period of 5 nm and an average aluminum content of 80 % in dependance of well and barrier composition (b). The acceptor concentration is $1 \times 10^{19}\,\mathrm{cm}^{-3}$.

eral orders of magnitude. This can be explained by a gradual shift of the transmission band to higher energies with increasing SPSL period. This leads to a smaller overlap between transmission spectrum and the Fermi-Dirac distribution, i. e. the SPSL is only transparent for excited holes. A similar behavior can be observed for increasing band offset between wells and barriers (in Fig. 5.7 represented by the composition offset). As the average hole concentration drastically increases, the transmission factor drops several orders of magnitude. An increased band offset pushes the Fermi level in the SPSL closer to the acceptor levels in the barrier leading to enhanced ionization. This is additionally enhanced by the increasing internal fields with increasing composition offset and resulting increased band bending. On the other hand, by increasing the band offset the transmission band width decreases decreasing the overlap with Fermi-Dirac distribution, which again results in a decreased transmission probability. If this theoretically discussed effect turns out to be relevant in grown epitaxially structures despite side effects from unideal crystal quality, a suitable compromise between enhanced acceptor ionization and efficient vertical hole transport needs to be found in order to design an optimized SPSL geometry for deep UV laser diode cladding layers. The characteristics of laser diode heterostructures with SPSL cladding will be discussed in section 5.1.2.

While the introduction of an SPSL enhances the ionization of acceptors compared to thick AlGaN layers the optical properties remain. Fig. 5.8 shows the transmission spectra of $Al_xGa_{1-x}N$:Mg/$Al_yGa_{1-y}N$:Mg SPSLs with different average aluminum contents between 37 % and 81 % and the transmission of the used AlN/sapphire for

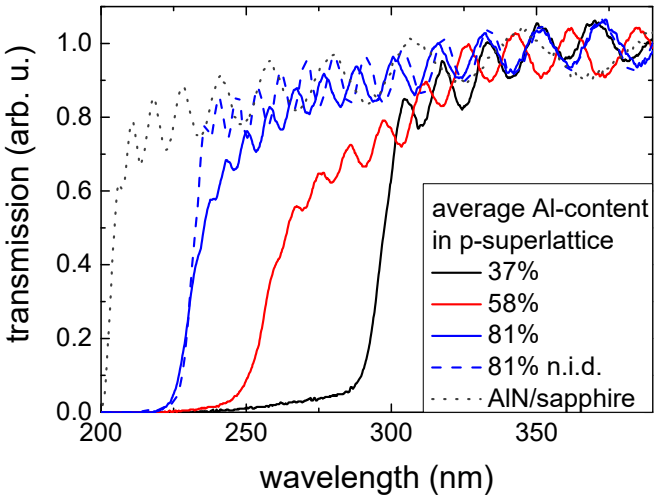

Figure 5.8 Optical transmission spectra of AlGaN SPSLs with different average aluminum content. The transmission of the used planar AlN/sapphire is shown for comparison. (measurement by C. Kuhn (TU Berlin)) [90]

comparison. A clear absorption edge can be observed for all SPSLs at decreasing wavelengths for increasing aluminum content. The absorption edges of the SPSLs correspond to the band edge energies of thick $Al_xGa_{1-x}N$ with the respective average aluminum content. The AlGaN:Mg SPSLs exhibit an absorption tail into the transparent region, i.e. into the band gap. The comparison of transmission spectra of Mg-doped and undoped SPSLs clearly shows that this absorption tail correlates with the Mg-doping. This has also been observed for GaN used for blue-violet laser diodes [110, 111]. The influence of magnesium acceptors on modal losses in AlGaN based waveguide structures will be discussed in section 5.2 in detail. As the refractive index is not independent of the absorption coefficient, but linked by the Kramers-Kronig relation, the refractive index of an SPSL is also expected to show comparable behavior to thick layers with the corresponding composition [112]. Therefore, AlGaN:Mg SPSL cladding layers can be used for high injection efficiency laser diode heterostructures.

5.1.2 Hole injection into active region with high mode confinement

The in section 5.1.1 introduced SPSL structures are integrated in laser diode heterostructures in order to experimentally investigate their suitability as efficient current injection p-side cladding layers. The chosen heterostructure is described above and schematically shown in Fig. 5.1. Since the influence of the SPSL geometry on carrier transport is difficult to predict (as discussed in section 5.1.1), different SPSL designs are tested and compared to a thick AlGaN:Mg p-cladding layer. The investigated p-cladding variations are summarized in table 5.1 with average aluminum content, aluminum content in wells and barriers, SPSL period, number of period, and total SPSL thickness. The variation includes SPSLs with different average aluminum con-

ave. Al cont.	layer Al cont.	period	period number	thickness
37%	32% / 42%	5.0 nm	33	150 nm
37%	32% / 42%	1.8 nm	111	200 nm
58%	71% / 46%	1.8 nm	111	200 nm
81%	91% / 71%	1.8 nm	111	200 nm
81%	single layer	single layer	single layer	200 nm

Table 5.1 Different p-SPSL geometries integrated in a laser diode heterostructure.

tent ranging from 37 % to 81 %. The duty cycle of the SPSL is kept constant at 0.5 (i.e. the well and barrier widths are equal).

All AlGaN:Mg SPSLs as well as the thick $Al_{0.81}Ga_{0.19}N$:Mg layer were grown with the same Cp_2Mg flow rate. Since the aluminum content was varied by adjusting the gallium flow rate, the Mg/group-III ratio in the gas phase during growth increases for increasing aluminum content. However, the magnesium concentration of all p-cladding layers is $2 \pm 0.5 \times 10^{20}\,\mathrm{cm}^{-3}$ as determined by wavelength-dispersive x-ray analysis (WDX) [113] (measurement by G. Kusch (University of Strathclyde)). All wafers were processed into LED structures for bottom emission. A 100 µm × 100 µm Pd-based p-contact was deposited on top of the p-GaN contact layer and after mesa etching a wide V-based n-contact was deposited on the n-cladding layer. All electrical charcterization discussed in this chapter has been performed on-wafer, by contacting the contact metal of the devices with needles using micro positioners [114].

Prior to characterizing the full LED structure, the transfer length method (TLM) is applied in order to characterize the metal contacts and injection layers of the n- and p-side, respectively. By comparing the nn or pp I-V characteristics from contacts with different spacing this method allows to determine the contact resistivity, sheet resistivity and transfer length [115]. For this purpose metal contacts with different spacing ranging from 8 µm and 25 µm were deposited on the lower $Al_{0.80}Ga_{0.20}N$:Si cladding layers and the GaN:Mg contact layers.

Fig. 5.9(a) shows the nn I-V characteristics exemplary for the $Al_{0.80}Ga_{0.20}N$:Si cladding layer of the laser diode heterostructure with the p-SPSL with an average aluminum content of 58 % for different electrode spacings from 8 µm to 25 µm. All characteristics show a nonlinear behavior with a voltage onset of about 3 V, indicating the Schottky-like behavior of the metal contacts. Also shown is the total resistivity in dependance of the applied voltage. As the bias voltage overcomes the Schottky barrier the resistance drops about two orders of magnitude. The electrode spacing, on the other hand, has a much weaker influence on the resistance. This is clear evidence that the I-V characteristics in this voltage range is rather dominated by the contact

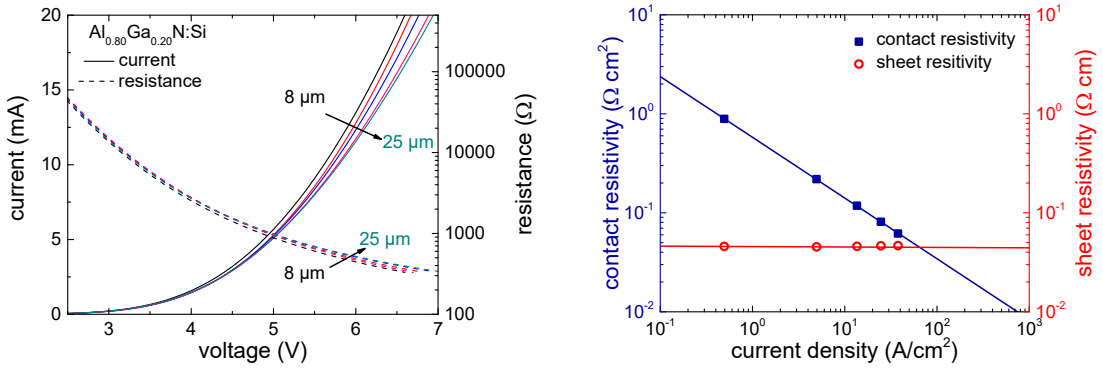

(a) nn I-V characteristics (b) contact and sheet resistivity

Figure 5.9 nn I-V characteristics and its total resistance (a) and contact and sheet resistivity determined by TLM (b) of a lower $Al_{0.80}Ga_{0.20}N$:Si cladding layer. Exemplary shown is the data from the heterostructure with an SPSL with an average Al content of 58 %. (measurement by E. Ziffer (TU Berlin))

resistance than the sheet resistance. From electrode spacing dependent resistances the contact and sheet resistivities for different current densities were derived according to the TLM formalism [115] (see. 5.9 (b)). With increasing current density the contact resistivity drops to a value of $6 \times 10^{-2}\,\Omega\,\mathrm{cm}^2$ at $40\,\mathrm{A/cm}^2$. The higher the applied voltage and the injected current density, the influence of the Schottky barrier decreases and consequently the contact resistivity decreases. However, even if extrapolated for high current densities ($\sim 10^{-3}\,\Omega\,\mathrm{cm}^2$ at $10\,\mathrm{kA/cm}^2$) the contact resistivities are considerably higher compared to reported values from optimized n-contacts on $Al_{0.40}Ga_{0.60}N$ in the range of $10^{-6}\,\Omega\,\mathrm{cm}^2$ [116]. The high contact resistivities on the $Al_{0.80}Ga_{0.20}N$:Si cladding layers can partially be explained by the increased aluminum content, which results in higher electron affinities and due to the higher ionization energies of silicon donors in lower carrier densities. Both effects make the development of low resistive, ohmic contacts more challenging. On the other hand, it has been shown that the contact resistivity of the metal contacts can strongly depend on process technology parameters such as surface treatment and formation temperature [116]. Therefore, the contact resistivity of the metal contacts on $Al_{0.80}Ga_{0.20}N$:Si may also be reduced by further process optimization. The sheet resistivity, on the other hand, is constant over the investigated current density range. The value of $4 \times 10^{-2}\,\Omega\,\mathrm{cm}$ is in the range of previously reported resistivities of comparable layers determined by contactless resistivity measurements [92].

To gain information about the p-contact and p-SPSL cladding layer resistances is somewhat more complicated compared to the n-TLM analysis discussed above. In the TLM geometry with planar contacts on the crystal surface the current path neces-

sarily has a lateral and a vertical contribution. As the electrode spacing increases the lateral part will become more dominant. However, the carrier density and mobility are expected to be extremely anisotropic within SPSL structures (see 5.1.1). Also, the contribution of the carriers traveling laterally through the p-GaN contact layer and also the influence of the interface between contact and cladding layer can hardly be quantified. Therefore, this method is not suitable to determine the sheet resistivity for a vertical current path through an SPSL layer stack and consequently not applicable to conventional, edge emitting devices investigated in this work.

Testing the devices in LED operation allows to investigate the influence of the Al content and SPSL geometry in the p-side on the electrical and optical performance of the laser diode heterostructures. In order to reach the active regions, the holes need to travel vertically through the SPSLs, the same way as they would for laser operation. All LEDs show dominant quantum well emission between 265 nm and 275 nm without longer wavelength parasitic luminescence independent of driving current or the p-side cladding (see Fig. 5.10). This shows, that all investigated p-sides are capable of injecting holes into the active region, where sufficient overlap with electrons can be provided for radiative recombination. Additionally, the absence of parasitic luminescence is a sign for efficient electron blocking. Usually a broad emission band at longer wavelengths than the MQW emission in deep UV AlGaN MQW emitters is attributed to defect related electron-hole recombination in the p-side [87]. Therefore, we can conclude that electrons are not significantly able to overshoot the electron blocking structure.

Taking a closer look at the I-V characteristics of the LEDs with the different p-side can provide a deeper insight into the influence of the SPSLs on the carrier transport (see Fig. 5.11(a)). All characteristics show a clear diode-like behavior with a distinct

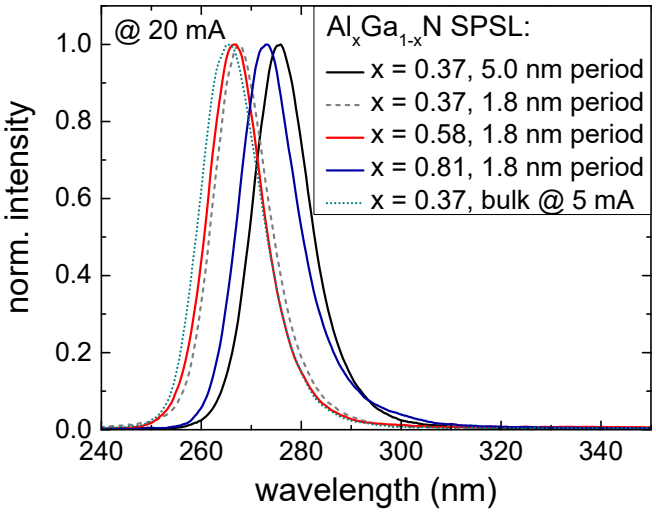

Figure 5.10 Emission spectra of LEDs with different AlGaN p-sides at 20 mA. (measurement by E. Ziffer (TU Berlin))

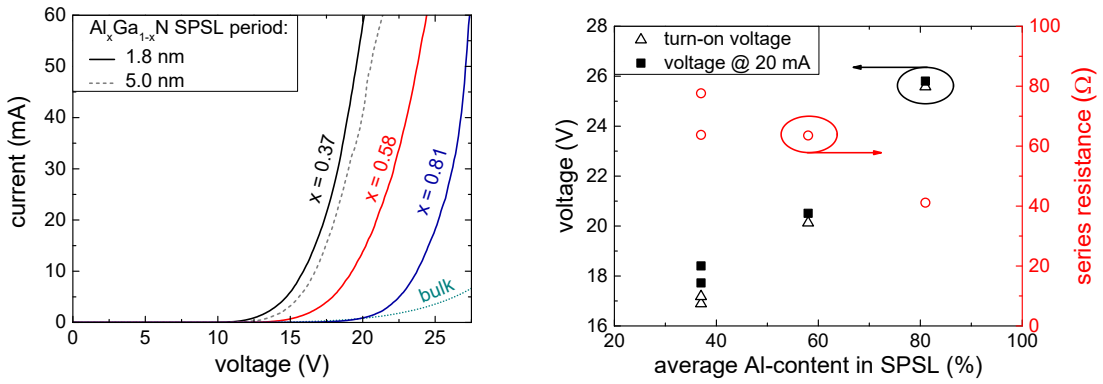

(a) cw I-V characteristics (b) cw emission spectra

Figure 5.11 I-V characteristics of LED structures for bottom emission with different p-side cladding layers in cw operation (a) and the extracted operation voltages and series resistances in dependance of the Al content in the p-side cladding layer (b). (measurement by E. Ziffer (TU Berlin)) [90]

turn-on voltage. As the MQW emission was observed to set in as soon as the current starts to flow, parasitic current paths bypassing the active region can be excluded. With increasing Al content in the p-side the operation voltage clearly increases. For the diode with a 200 nm thick bulk $Al_{0.81}Ga_{0.19}N$:Mg layer only low currents in the range of 5 mA could be injected. Its counterpart, however, with an SPSL with the same aluminum content in average exhibits significantly higher currents of more than 60 mA at the same voltages indicating higher vertical conductivity for the SPSL compared to a thick layer with homogeneous composition. Additionally, the diodes with a p-AlGaN:Mg SPSL with a period of 1.8 nm and 5 nm with the same average aluminum content of 37% exhibit comparable characteristics even though the total thickness of the layer stack with the smaller period is higher. At the turn-on voltage the current increases with increasing voltage as the applied field overcomes the built-in potential at the pn-junction turning into a linear regime dominated by the series resistance of the diode. The turn-on voltages and the series resistances have been determined for all diodes. This as well as the operation voltage at 20 mA is shown in Fig. 5.11(b) in dependance of the average Al content in the p-SPSL cladding layers.

The turn-on voltage increases from 17 V to 26 V when the aluminum content is increased from 37% to 81%. The operation voltages at 20 mA are slightly higher and follow the same trend. In order to understand the rather high operation voltages the turn-on voltages and the series resistances have to be discussed individually. The turn-on voltages need to be applied to overcome different potential barriers within the heterostructure before carriers can travel through. Obviously, this includes the built-in potential at the pn-junction. The built-in potential is given by the difference

of the Fermi levels in the layers directly surrounding the intrinsic layers, which are in the present heterostructures $Al_{0.70}Ga_{0.30}N$:Si and $Al_{0.70}Ga_{0.30}N$:Mg, respectively. Consequently, in the case of non degenerate semiconductors, which can be very well assumed for high Al content AlGaN material, the built-in potential needs to be smaller than the corresponding band gap energies of these layers. Therefore, we can estimate the contribution of the built-in potential to the turn-on voltage to be smaller than 5 V for all diodes. The additional voltage is mainly made up of the potential barriers at the metal contacts. The TLM data discussed above showed that the n-contacts on the $Al_{0.80}Ga_{0.20}N$:Si cladding layers are not ohmic. The nn I-V characteristics reveals a voltage offset in the range of 3 V. As the Schottky like contacts are arranged in back-to-back constellation, this voltage offset is the sum of the voltage drops at one contact in reverse and one contact in forward operation. Qualitatively separating both contributions is difficult. However, we can conclude that the voltage drop in LED operation over the n-contact is less than 3 V in all heterostructures.

Both contributions to the turn-on voltage discussed, the built-in potential at the pn-junction and Schottky barrier at the n-contacts, are independent of the p-cladding layer and hence identical in all characteristics. Therefore, a third contribution needs to be discussed, which causes the increase of turn-on voltage with increasing Al content in the p-side. This part is attributed to a voltage drop at the p-contact, although the p-contacts are also deposited on the nominally same p-GaN contact layers. The nominal thickness of the p-GaN layer is only 20 nm. Additionally, due to the large lattice mismatch between the coherently grown AlGaN layers and the p-GaN contact layer and the resulting high compressive strain, the p-GaN tends to grow in islands and eventually does not form a complete coverage as observed for similar heterostructures. Therefore, the influence of this layer on the heterostructures' band structures and the Schottky barrier is unknown. However, the increased Al content in the p-cladding causes either an increased potential barrier between AlGaN cladding layer and p-GaN contact layer or an increase of the height and, due to lower hole concentration, width of the Schottky barrier at the contact metal. Either effect can cause the increase of turn-on voltage, that is observed in the I-V characteristics. Additionally, the fact that the Al content in the p-side and not the design of the p-side (i.e. bulk or SPSL, SPSL geometry) has the major influence on the turn-on voltage is evidence that this increase is a result of an increased potential barrier at the top interface of the p-cladding layer. The series resistance, on the other hand, decreases with increasing Al content in the p-SPSL cladding layers (Fig. 5.11(b)). The series resistance is determined far beyond the turn-on in a linear regime of the I-V characteristics, where the internal barriers are overcome by the external field, and represents the sum of the ohmic resistances

of each element in the layer stack. Because of the higher ionization energies, it is expected that with increasing Al content in the p-side the resistance also increases. This should result in a higher series resistance, which cannot be observed. Therefore, the decreasing series resistance is attributed to higher Joule heating of the device for higher dc operation voltages. In pulsed operation, where Joule heating is negligible, the series resistance increases with increasing Al content in the p-side ($\sim 80\,\Omega$ - $\sim 120\,\Omega$), which is attributed to the higher ohmic resistance of the SPSLs. However, the series resistance of all diodes with an SPSL p-side is about one order of magnitude lower compared to the diode with a 200 nm thick bulk p-$Al_{0.81}Ga_{0.19}N$:Mg layer.
The laser diode heterostructure with an $Al_{0.91}Ga_{0.09}N$:Mg/$Al_{0.71}Ga_{0.29}N$:Mg SPSL cladding provides high optical confinement with an confinement factor of more than 4 % as well as sufficient carrier injection and confinement for deep UV emission. Thereby, both key requirements for an efficient separate confinement heterostructure are fulfilled. The LED structures discussed above are primarily designed for bottom emission through the sapphire substrate. Edge emitting lasers, however, require a well defined cavity. For this purpose, additionally to the LEDs, the laser heterostructures were processed into broad area laser diodes. A stripe-shaped Pd-based p-contact is deposited on the crystal surface. As the contact geometry defines the pumped area, the cavity width is determined by the stripe width. Comparable to the optically pumped lasers (see section 2.1.2) the resonator mirrors are formed by the $(1\bar{1}00)$ crystal facets obtained by laser scribing and subsequent cleaving. No additional facet coating was deposited. The V-based n-contact was deposited alongside the p-contact stripe after mesa etching. Fig. 5.12(a) shows an SEM image of a part of a cleaved laser bar with 24 different diodes with cavity widths of 5 µm, 10 µm, 20 µm, and 40 µm, respectively and cavity lengths of 1000 µm. The red line marks the outline of a single laser diode chip with a stripe width of 20 µm.
The laser diode structures were driven in pulsed operation. This way the effects of Joule heating, i.e. increased non radiative recombination rate and decreased injection efficiency, can be minimized. Short pulses of 100 ns and a repetition rate of 30 kHz have been used. In order to prevent the devices from damage, the pulse needs to be clearly shaped without severe ringing. Ringing can occur, if the impedances of the device under test and the pulse source are not matched. This, however, is difficult to accomplish since the impedance drastically varies with the applied voltage, which can be easily seen for the ohmic part of the impedance. Therefore, the devices are pre-biased with a DC voltage of 20 V, which introduces a DC current of about 1 mA. This means, that the DC voltage overcomes the turn-on voltage, while the voltage pulses are operating in a range of the characteristic, where the impedance is quite

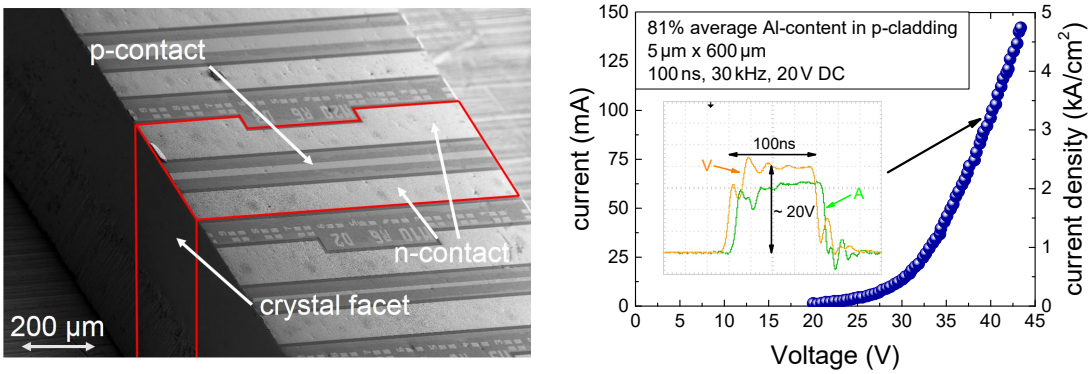

(a) SEM image of a processed laser diode structure

(b) pulsed I-V characteristic

Figure 5.12 SEM image of a processed laser diode structure for edge emission with a cavity length of 1000 µm and widths between 5 µm and 40 µm (measurement by L. Sulmoni (TU Berlin))(a). Pulsed I-V characteristic of a laser diode heterostructure with symmetric $Al_{0.80}Ga_{0.20}N/Al_{0.70}Ga_{0.30}N$ waveguide structure (b). The inset shows the 100 ns current and voltage pulse as displayed on the oscilloscope. Measurement was performed with a 20 V DC bias applied. [90]

constant. The DC voltage, however, does not cause severe heating as the DC current is small. The pulsed and DC signals are coupled into a bias tee (Picosecond Pulse Labs, model 5530B [117]) over a high pass or low pass filter, respectively, before the mixed signal is applied to the diode. The resulting voltage and current pulses with suppressed ringing are shown in the inset of Fig. 5.12(b).

The pulsed I-V characteristic of a laser diode structure with a 5 µm × 600 µm cavity is shown in Fig. 5.12(b). The diode withstands currents of almost 150 mA which translates into a current density of more than 4.5 kA/cm^2, before breaking through. Although high currents can be injected and the heterostructure provides sufficient mode guiding, carrier densities in the active region are not high enough for stimulated emission or laser operation. This means that either net gain or injection efficiency needs to improved. In the following section the influence of the Mg-doping on the optical losses will be discussed before heterostructures will be suggested which combine high injection efficiency with low modal losses.

5.2 Combining high modal gain and efficient carrier injection

The transmission data discussed in section 5.1.1 already showed, that introducing Mg-doping to the AlGaN SPSLs affects the absorption of the layers (Fig. 5.8). With

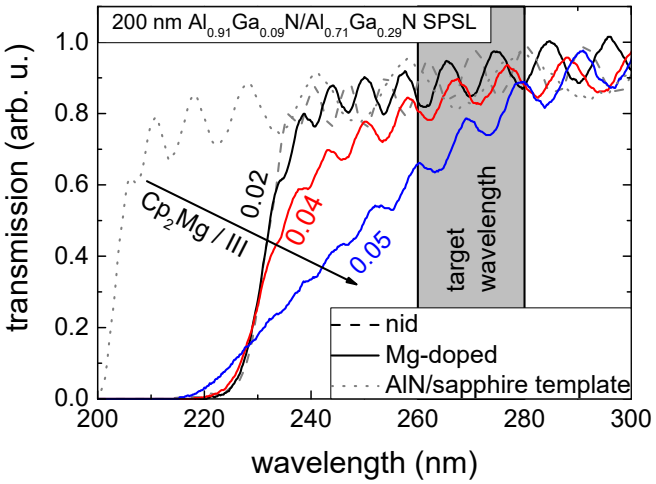

Figure 5.13 Optical transmission spectra of $Al_{0.91}Ga_{0.09}N/Al_{0.71}Ga_{0.29}N$ SPSLs with different Mg-doping ranging from nid to a Cp_2Mg/group-III ratio (in the gas phase) of 0.05. The transmission of the used planar AlN/sapphire is shown for comparison. (measurement by C. Kuhn (TU Berlin))

Mg-doping a clear absorption tail into the band gap is present. Fig. 5.13 shows transmission spectra of 200 nm thick $Al_{0.91}Ga_{0.09}N/Al_{0.71}Ga_{0.29}N$ SPSLs as used for cladding layers in laser diode heterostructures with different Mg concentration realized by different Cp_2Mg/goup-III ratios in the gas phase during epitaxial growth of the layers. With increasing Mg-doping the absorption tail becomes more prominent in the band gap. For the highest Mg concentration investigated the absorption edge is dramatically broadened, which indicates that these high Mg levels lead to the formation of additional defects or to crystal degradation. From the transmission data Mg-induced absorption in the range of 9000 cm^{-1} can be estimated for these high Mg levels. However, even for lower Mg concentrations the absorption tail extends to the target emission wavelengths of the designed laser heterostructures resulting in modal losses, although the band edge energies of the QWs and the cladding layer clearly differ. Those Mg-induced modal losses have to be taken into account in order to design efficient laser diode heterostructures. The issue of modal losses in the p-side of nitride-based laser diodes has already been discussed for devices emitting in the visible spectral range grown on GaN based substrates. Therefore, the Mg-induced absorption has been studied for GaN and low aluminum content AlGaN [110, 111, 118]. For higher Al content AlGaN ($x \geq 0.70$) as needed as waveguide or cladding layers in deep UV laser diodes, however, there is a lack of reliable data concerning the Mg-induced absorption.

The transmission data in Fig. 5.13 can only provide limited information about the absorption within the band gap of moderately Mg-doped layers, which are used for current injection devices, because the spectra are dominated by Fabry-Perot oscillations and features originating from the AlN/sapphire templates. In order to quanti-

tatively investigate the absorption in Mg-doped layers additional approaches have to be considered.

5.2.1 Magnesium induced absorption in Mg-doped AlGaN

As described in section 2.2.1 optical losses can be well obtained from gain spectra determined by the VSLM performed on optically pumped laser structures. In order to investigate the influence of Mg-doping on the optical losses in deep UV lasers different samples with different doping depths in the upper waveguide layer are analyzed. By varying the setback of the Mg-doping within the upper waveguide layer we are able to realize different mode overlap with the doped regions without altering the mode guiding itself and we are able to correlate the modal losses with effects resulting from the Mg-doping.

The laser heterostructures, which were analyzed for this study, base on the optically pumped lasers discussed in section 2.1.1 with an $Al_xGa_{1-x}N/Al_yGa_{1-y}N$ QW active region embedded in a 30 nm lower $Al_{0.70}Ga_{0.30}N$ and a 80 nm upper $Al_{0.70}Ga_{0.30}N$ waveguide layer and a 1200 nm lower $Al_{0.80}Ga_{0.20}N$ cladding layer. A 5 nm thick single quantum well was chosen for these studies in order to exclude possible effects originating from inhomogeneous carrier distributions in the QWs of an MQW active region due to relaxation of carriers photogenerated in the upper waveguide layer (see section 4.2.2). Three different laser heterostructures with different Mg-doping in the upper waveguide were grown. The waveguide variations include a completely Mg-doped upper waveguide, one waveguide with the topmost 60 nm Mg-doped, and one waveguide with the topmost 40 nm Mg-doped (see Fig. 5.14 left). Additionally, one

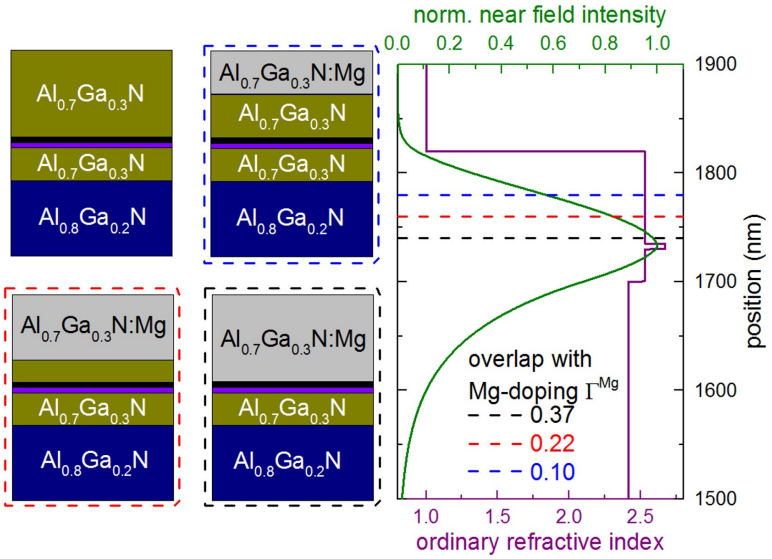

Figure 5.14 Schematic of the investigated optically pumped lasers with different doping depth in the upper waveguide layer (left). Refractive index profile and calculated optical mode of the lasers (right). The overlap of the mode with the Mg-doped region for the different structures is 0%, 10%, 22%, and 37%. [119]

laser structure without Mg-doping was grown as reference. The Mg concentration is $\sim 1 \times 10^{20}\,\mathrm{cm}^{-3}$ as determined by secondary ion mass spectroscopy measurements (SIMS). This doping level is comparable to the one in the current injection heterostructures discussed in section 5.1.2 and has proven to be suitable for efficient carrier injection into deep UV laser heterostructures [90]. Usually Mg acceptors are bound in Mg-N-H complexes in as-grown (Al)GaN layers. This leads to increased hydrogen concentrations and reduced hole densities in those layers. Therefore, the mangesium needs to be activated by thermal annealing [94]. After annealing the hydrogen concentration in the investigated layers was determined to be $\sim 2 \times 10^{19}\,\mathrm{cm}^{-3}$, which is one order of magnitude lower than the Mg concentration which means that most of the Mg acceptors are activated. In all heterostructures the upper waveguide is separated by a 5 nm thick nid $Al_{0.70}Ga_{0.30}N$ interlayer from the active region in order to minimize diffusion from Mg-acceptors into the SQW. However, SIMS analysis showed in the case of the structure with the completely Mg-doped upper waveguide layer considerable Mg levels in the range of $10^{19}\,\mathrm{cm}^{-3}$ in the SQW region. This can result in significantly increased non radiative recombination rates and reduced IQE.
The refractive index profile and the calculated optical mode distribution of the lasers is shown in Fig. 5.14(right). Due to the high activation energies of Mg acceptors in the $Al_{0.70}Ga_{0.30}N$:Mg layer, the free hole density is expected to be fairly low [99]. Therefore, the optical mode is assumed to be independent of the Mg-doping and consequently identical for all the optically pumped lasers. The confinement factor of the laser heterostructures is 0.04. With decreasing width of the Mg-doped layers and increasing spacing between the Mg-doped layer and the active region the overlap of the optical mode with the Mg-doped region Γ^{Mg} decreases from 0.37 to 0 for the structure without Mg-doping.
All laser heterostructures were grown on wafers of the same batch of ELO AlN/sapphire templates, which ensures comparable crystal quality in the nid AlGaN layers in all structures. Fig. 5.15 shows AFM images of the laser heterostructures' surfaces. The surface morphologies are dominated by undulation patterns with a period of 3.5 µm originating from the ELO AlN/sapphire templates and hills originating from the spiral growth of the $Al_{0.80}Ga_{0.20}N$ cladding layers. The Mg-doping in the upper waveguide layer, however, does not influence the surface morphology. Degradation of the surface as reported for highly Mg-doped GaN layers [120, 121], was not observed. Therefore, we conclude that modal losses originating from interface scattering or absorption in the undoped layers should be similar for all lasers and we should be able to separate the influence of the Mg-doping from all other effects.
All lasers show photopumped spontaneous emission from the facet in a wavelength

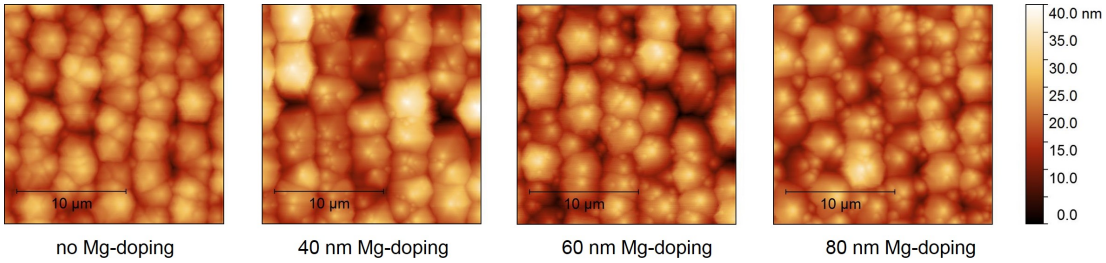

Figure 5.15 $20\,\mu m \times 20\,\mu m$ AFM images of the laser with undoped, 40 nm Mg-doped, 20 nm Mg-doped, and completely Mg-doped upper waveguide. Independent of the Mg-doping of the upper waveguide layer the samples exhibit a stripe-like morphology originating from the patterned ELO AlN/sapphire template. [119]

range between 270 nm and 280 nm. Clear threshold behavior is present in $P_{out} - P_{exc}$ characteristics for all lasers except for the one with the completely Mg-doped upper waveguide layer (see Fig. 5.16(a)). This laser shows a linear increase of spontaneous emission with increasing pump power as expected below threshold up to an excitation power density of $\sim 25\,\mathrm{MW/cm^2}$. With increasing thickness of the Mg-doped region the laser threshold power density increases from $2.5\,\mathrm{MW/cm^2}$ to $12\,\mathrm{MW/cm^2}$ (see Fig. 5.16(b)). This increase can partially be attributed to the expected increase of modal losses due to Mg-doping related absorption and resulting lower net gain. However, also different pump efficiencies have to be considered. The effect of the Mg-doping on the recombination and transport of carriers generated in the upper

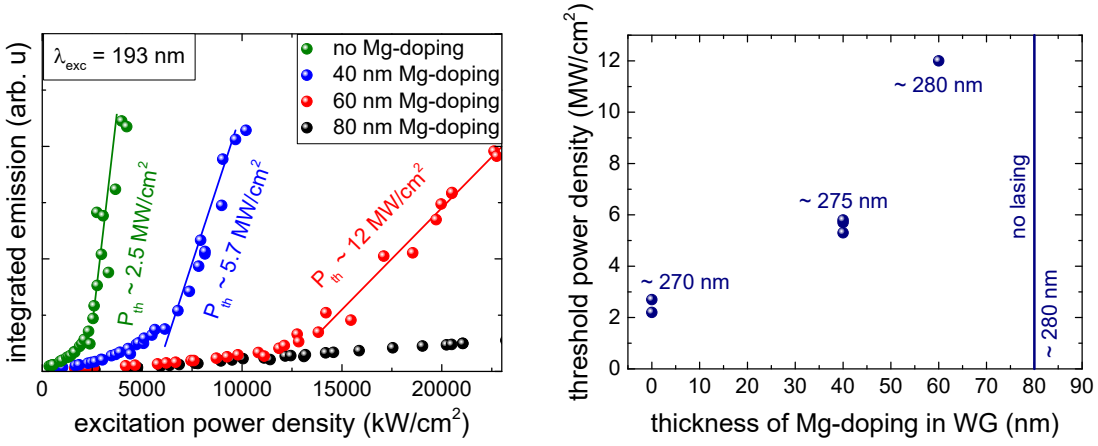

(a) $P_{out} - P_{exc}$ characteristics

(b) optically pumped laser threshold

Figure 5.16 $P_{out} - P_{exc}$ characteristics of the optically pumped lasers with different Mg-doping in the upper waveguide layer (a) and laser threshold power density versus thickness of Mg-doped region of the lasers with the corresponding laser emission wavelength or spontaneous emission wavelength of the heterostructure with the completely Mg-doped upper waveguide (b).

$Al_{0.70}Ga_{0.30}N$ waveguide layer into the SQW has to be taken into account. Because the non-radiative recombination lifetime in the Mg-doped layers is expected to be shorter than in the undoped regions, more efficient carrier injection into the SQW and consequently higher carrier densities within the active regions can be expected for lasers with thinner Mg-doped regions even if the excitation power densities are the same. Additionally, the higher Mg level in the SQW of the laser heterostructure with the completely Mg-doped upper waveguide might result in an increased point defect density in the SQW inhibiting laser operation.
Also shown in Fig. 5.16(b) is the laser emission or spontaneous emission wavelength, respectively. The emission wavelength varies between 270 nm and 280 nm. Although the emission seems to follow a trend of shifting towards longer wavelengths for increased thickness of Mg-doped waveguide, this is rather attributed to fluctuations in the growth conditions than to effects originating from the magnesium acceptors.
Fig. 5.17(a) shows the gain spectra determined by the VSLM (see section 2.2.1) of the optically pumped laser without Mg-doping in the waveguide for different excitation power densities. For an excitation power density of 2.2 MW/cm^2, which is below the laser threshold power density of 2.5 MW/cm^2, the net gain is with 5 cm^{-1} too low to overcome the mirror losses. With increasing pump power the net gain increases reaching a value of $\sim$45 cm^{-1} for an excitation power density of 8.4 MW/cm^2 (see Fig.5.17(b)). The increase of the net gain peak can be described by a logarithmic approach with the confinement factor $\Gamma^{QW} = 0.042$, the gain coefficient $g_0 = 690\,\mathrm{cm}^{-1}$, and the transparency power density $P_{tr} = 1.9\,\mathrm{MW/cm}^2$. The peak wavelength shifts about 1 nm from 269 nm to 268 nm with increasing pumping power due to screening

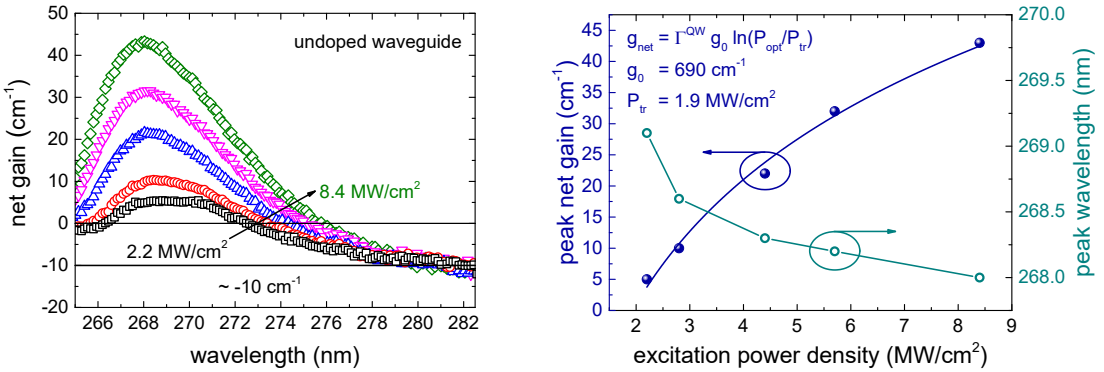

(a) gain spectra (b) peak gain and gain peak wavelength

Figure 5.17 Optical gain spectra for different excitation power densities (a) and the peak net gain as well as the peak gain wavelengths versus pumping power (b) of the optical pumped laser without Mg-doping. [119]

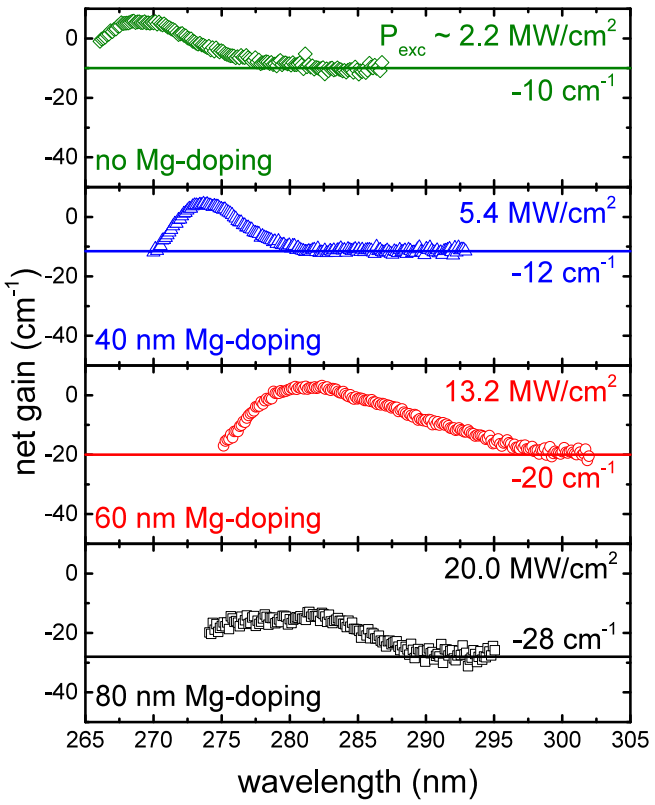

Figure 5.18 Gain spectra of the optically pumped lasers with different Mg-doping in the upper waveguide at excitation power densities in the range of the laser threshold. [119]

of the QCSE and band filling. On low energy side the gain spectra saturate at the same value of 10 cm^{-1} independent of the excitation power representing the internal losses. Those internal losses can e.g. originate from reabsorption of the optical mode at defect or surface states or scattering of the mode at rough surfaces or interfaces. Since all lasers have comparable crystal quality and morphology those losses are assumed to be present in all optically pumped lasers independent of the Mg-doping in the upper waveguide layer.

Gain spectra of the optically pumped lasers with different Mg-doping in the waveguide are shown in Fig. 5.18 for comparison at excitation power densities in the range of the respective laser threshold except for the heterostructure with the completely Mg-doped upper waveguide. This laser does not reach positive net gain even for high excitation power densities of 25 MW/cm^2, although material gain can clearly be observed. However, carrier densities within the active regions are too low to overcome the internal losses. As already observed for the laser emission and the spontaneous emission from the SQW, the gain spectra vary between 270 nm and 280 nm for the different heterostructures due to slight deviations in the growth conditions from run to run.

All gain spectra reach a saturation level at the low energy side of the spectra. Be-

cause this feature is independent of the carrier density, we are able to compare the internal losses of the different heterostructures. With increasing overlap of the optical mode with the Mg-doped waveguide region, the modal losses increase from 10 cm^{-1} to 28 cm^{-1}. The laser with the undoped waveguide exhibits internal losses of (10±2) cm^{-1}, which cannot originate from Mg-induced absorption. Therefore, those losses are referred to as residual losses α^{res}. Since all laser heterostructures have the same structural properties and morphologies, those residual losses originating from modal scattering or absorption in undoped regions are assumed to be the same in all the lasers. This allows to calculate the overall internal losses α^i of all lasers by applying the linear relation

$$\alpha^i = \alpha^{Mg}_{mat} \times \Gamma^{Mg} + \alpha^{res}, \tag{5.2}$$

where α^{Mg}_{mat} is the absorption factor for Mg-induced absorption in the waveguide and Γ^{Mg} is the overlap of the optical mode with the Mg-doped region.
The internal losses α^i derived from the measured gain spectra of the different lasers (Fig. 5.18) versus the mode overlap with the Mg-doped regions Γ^{Mg} is shown in Fig. 5.19. By applying a linear fit of the data and Eq. 5.2 we obtain the parameters $\alpha^{Mg}_{mat} = (50 \pm 10)\, cm^{-1}$ and $\alpha^{res} = (9 \pm 1)\, cm^{-1}$. The Mg-induced loss for a laser is then given by

$$\alpha^{Mg}_{mod} = \alpha^{Mg}_{mat} \times \Gamma^{Mg} = 50\, cm^{-1} \times \Gamma^{Mg}, \tag{5.3}$$

as shown in Fig. 5.19 (dashed, red line) [119].
The presented data cannot provide evidence for the origin of the Mg-induced absorption. However, studies have been published addressing this issue for Mg-doped GaN and low Al content AlGaN for the use in laser diodes emitting in the visible spectral

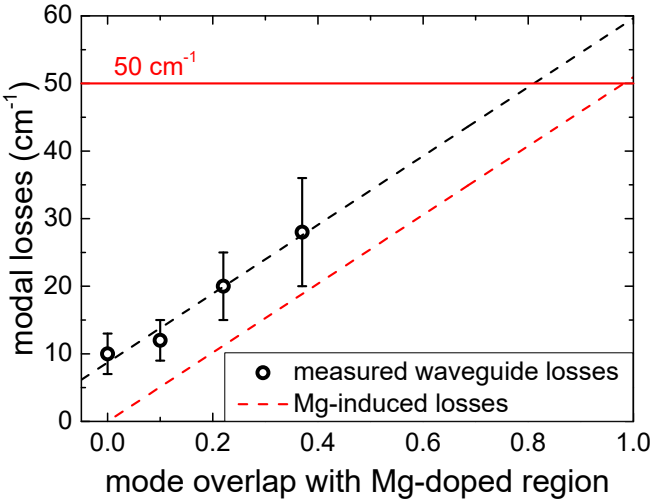

Figure 5.19 Modal losses obtained from gain spectra versus overlap of the optical mode with Mg-doped region. The red, dashed line shows the Mg-induced losses for the lasing mode corresponding to Eq. (5.3). [119]

range. Sizov et al. [111, 122] showed that the absorption within the band gap energy increases when the investigated GaN:Mg layers are thermally annealed and hydrogen levels are reduced indicating that the absorption is related to activated acceptors. It was also possible to reverse this effect by annealing the layers under ammonia atmosphere and repassivating the Mg-acceptors. Theoretical calculations suggested that absorption at acceptor bound holes is the main contribution for elevated absorption values [123]. The absoprtion values reported for GaN:Mg layers are with $\sim 100\,\mathrm{cm}^{-1}$ in the range as the one of the investigated $Al_{0.70}Ga_{0.30}N$:Mg layer [110, 111, 118].
For the studies above a SQW active region was used in order to ensure homogeneous pumping into the active region and best comparability between the lasers with different Mg-doping in the upper waveguide layer. However, the material gain of this active region is not high enough to overcome the high Mg-induced optical losses and consequently incapable of producing laser operation for the carrier densities that can be injected through Mg-doped regions. Therefore, this experiment has also been performed on optically pumped lasers with a 2.2 nm $Al_{0.42}Ga_{0.58}N$/5. nm $Al_{0.70}Ga_{0.30}N$ active region, which has a higher confinement factor and is expected to show higher material gain (see chapter 4). Fig. 5.20(a) shows the gain spectra of lasers with and without Mg-doping in the upper waveguide layer for comparison. The internal losses of the laser with a completely Mg-doped upper waveguide are about $16\,\mathrm{cm}^{-1}$ higher compared to the ones of the laser with nid waveguides. This difference is comparable to the results from the gain spectra of the lasers with an SQW active region discussed above.
The material gain of the TQW active region is high enough to overcome the optical

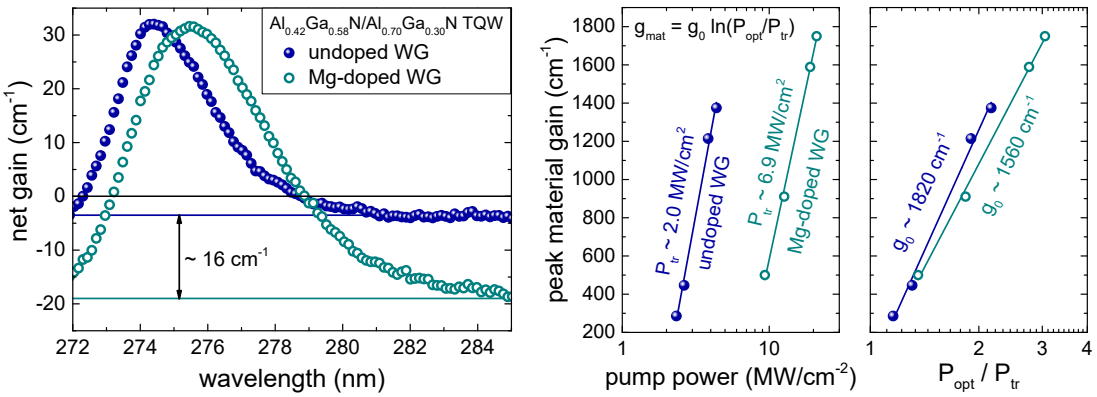

(a) gain spectra (b) peak gain

Figure 5.20 Optical gain spectra (a) and the peak material gain versus pumping power (b) of optically pumped lasers with and without Mg-doping in the upper waveguide layer with an $Al_{0.42}Ga_{0.58}N/Al_{0.70}Ga_{0.30}N$ TQW active region.

losses resulting in positive net gain resulting in laser operation. This allows to compare the behavior of the optical gain with pumping power. Fig. 5.20(b) shows the peak material gain in dependance of the excitation power density and pump power normalized to the respective transparency power density in a logarithmic scale. As the material gain is independent of the optical losses it gives a value for the amplification provided by the active region for a certain carrier density independent of the Mg-doping. The material gain of both lasers clearly follows a logarithmic trend, as expected for QW active regions. The transparency power density can than be extracted by fitting. The significantly increased transparency power density for the laser with Mg-doped upper waveguide can be attributed to the inefficient pumping as explained above. A better comparison can be done when the gain is plotted versus the pumping power normalized to the respective transparency power as shown on the right graph in Fig. 5.20. Assuming that transparency power density is the same for both lasers since the active regions are identical, this way the influences of the different relaxation processes of photogenerated carriers into the active region can be excluded giving rather information about the dependency on carrier density, than on excitation power density. The material gain of both lasers show a comparable behavior. The slope of the linear increase in the logarithmic scale is given by the gain coefficient g_0. By fitting, slightly different values for the lasers are obtained. This difference can be explained by the fact that the influence of the Mg-doping on the pumping efficiency is not expected to be linear with the excitation power density, because scattering processes at defects as well as recombination processes are not independent of the carrier density. Additionally, diffusion of Mg atoms into the last QW may limit the material gain. However, since this is only expected for the topmost of the TQW this effect is not as severe as it is for the SQW active region discussed above.
With the presented results we are able to reliably estimate the optical losses within the p-side of deep UV laser diodes. Additionally, as shown for the TQW active region the performance of the gain material is not significantly affected by the Mg-doping of the covering layers. This allows to optimize the heterostructures towards a compromise between low optical losses and efficient carrier injection without worrying about the gain medium.

5.2.2 Waveguide and cladding losses

As reported for GaN based lasers in the visible spectral range, absorption in the Mg-doped p-side of the laser diode heterostructures is the critical factor of the overall optical losses eventually hindering laser operation. The above determined absorption

value of 50 cm^{-1} [119] for AlGaN:Mg with high Al content allows us to calculate the p-side losses of deep UV laser diode heterostructures. Additionally to the absorption in the Mg-doped p-cladding layer absorption in the GaN:Mg contact layer and p-contact metal have to be taken into account. The absorption coefficient of the GaN:Mg layer used for the calculations is 1.75×10^5 cm^{-1} [29] and Pd is chosen as p-contact metal with an absorption coefficient of 10^6 cm^{-1} and a refractive index of 1.2 [86] for the target laser emission wavelength of 270 nm. In order to minimize p-side losses the upper waveguide layer is not Mg-doped and does therefore not contribute to the p-side losses.

Fig. 5.21 shows the refractive index profile and calculated mode distribution of a typical deep UV laser diode heterostructure with an $Al_{0.46}Ga_{0.54}N/Al_{0.70}Ga_{0.30}N$ TQW active region, an $Al_{0.70}Ga_{0.30}N/Al_{0.80}Ga_{0.20}N$ mode guiding structure, an $Al_{0.95}Ga_{0.05}N$ EBL for improved carrier injection [89], a GaN:Mg p-side contact layer and a Pd-based p-contact. The optical mode is well confinement to the waveguide with a confinement factor of $\Gamma^{QW} = 0.052$. Within the $Al_{0.80}Ga_{0.20}N$:Mg cladding layer the mode intensity drops about two orders of magnitude. The overlap of the optical mode with the p-cladding can be calculated from the mode simulation to be $\Gamma^{Mg} = 0.19$. This is the portion of the mode which is facing the determined absorption value of 50 cm^{-1}. Although the mode intensity at the interface between p-cladding and p-GaN contact layer is only about 10^{-3} of its maximum value absorption in the GaN:Mg and even in the contact metal may have a considerable contribution to the modal losses, due to the high absorption coefficients. The mode overlap in the present heterostructure

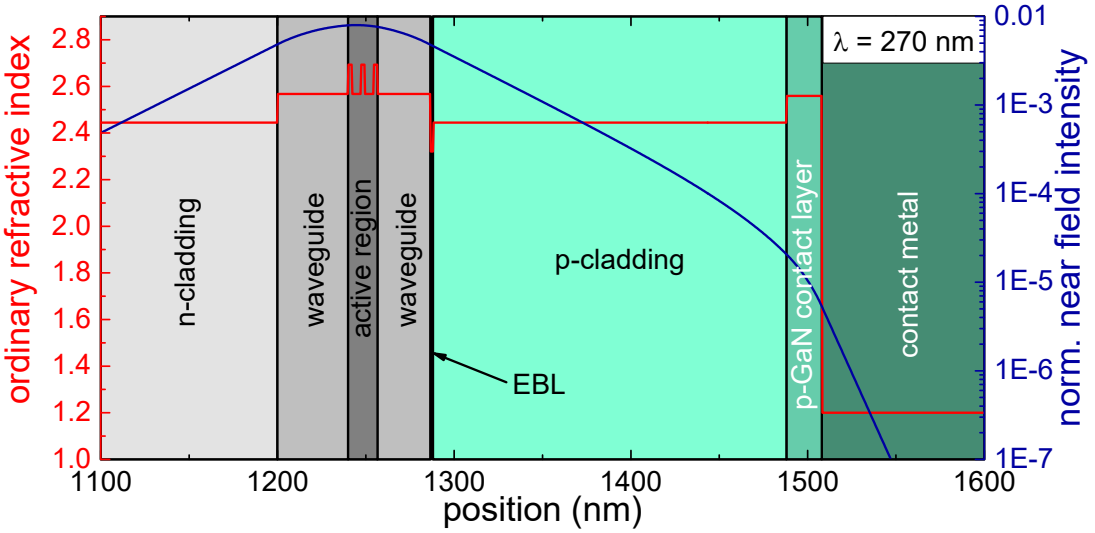

Figure 5.21 Refractive index profile and calculated mode distribution of a laser diode heterostructure with $Al_{0.70}Ga_{0.30}N/Al_{0.80}Ga_{0.20}N$ mode guiding structure for 270 nm emission.

with the p-GaN contact layer is $\Gamma^{GaN} = 2.4 \times 10^{-4}$ and the overlap with contact metal is $\Gamma^{Pd} = 5 \times 10^{-5}$. The overall p-side losses can then can be calculated by

$$\alpha^p = \Gamma^{Mg}\, 50\, cm^{-1} + \Gamma^{GaN}\, 1.75 \times 10^5\, cm^{-1} + \Gamma^{Pd}\, 10^6\, cm^{-1} \approx 100\, cm^{-1}. \quad (5.4)$$

As the laser diode heterostructure is altered the mode distribution changes affecting the modal losses in the p-side. Composition and thickness of the waveguide layers can be optimized for low mode losses. Fig. 5.22(a) shows e.g. the calculated mode profile in an $Al_xGa_{1-x}N/Al_{0.80}Ga_{0.20}N$ mode guiding structure with 40 nm lower and 30 nm upper waveguide layer for different waveguide compositions from x = 0.60 to x = 0.75. The mode confinement within the waveguide layers is provided by the refractive index difference between the waveguide and the cladding layer. By increasing the Al content in the waveguide layers this difference decreases. Consequently, the optical field distribution broadens and the mode overlap with the Mg-doped cladding layers increases and extends to the highly absorptive GaN:Mg contact layer and the contact metal. Another possible way to influence the optical mode is to alter the thickness of the upper waveguide layer (see Fig. 5.22(b)). This way not only the optical field distribution is affected, but also the geometry of the heterostructure itself has an influence on the overlap of the mode with the different regions as the interface between the cladding layer and the GaN:Mg contact layer is shifted away from the active region with increasing thickness of the upper waveguide layer. Additional to the width and composition of the waveguide layers, the optical mode can also be influenced by composition and thickness of the cladding layers.
Optimizing the heterostructure towards low optical losses, the influence of the heterostructure on the carrier injection needs to be considered. In order to estimate the

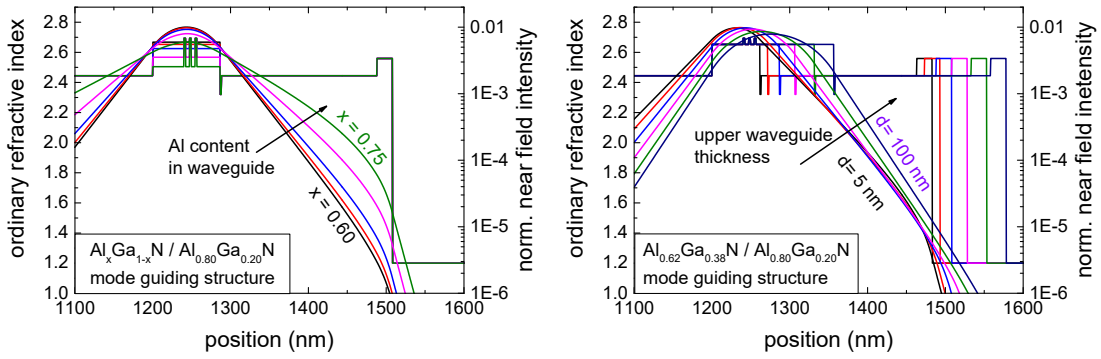

(a) waveguide composition (b) waveguide thickness

Figure 5.22 Calculated optical mode in waveguide structures with varying Al content in the waveguide layers and barriers (a) and varying upper waveguide thickness (b).

injection efficiency numerical simulations have been performed using the commercial software package SiLENSe [17]. The software uses a 1D approach to calculate current and voltage with a drift-diffusion model and the band structure with a Schrödinger-Poisson solver. The injection efficiency η_{inj} is then given by the total number of recombination processes R (including radiative and non radiative recombination) within the QWs normalized to the total number of injected carriers j/q:

$$\eta_{inj} = (q/j) \cdot \int_{QW} R(z) \cdot dz \tag{5.5}$$

Fig. 5.23(a) shows the according to equation 5.4 calculated modal losses within each layer of the diodes' p-sides and the total p-side losses of a laser diode heterostructure with an $Al_{0.46}Ga_{0.54}N/Al_xGa_{1-x}N$ TQW active region and a lower 40 nm thick $Al_xGa_{1-x}N$, an upper 30 nm $Al_xGa_{1-x}N$ waveguide layer and 1200 nm lower and 200 nm upper $Al_{0.80}Ga_{0.20}N$ cladding layers for different waveguide and quantum barrier composition (compare Fig. 5.22). With increasing Al content in the waveguide layers the modal losses increase due to the decreasing refractive index contrast between waveguide and cladding layer and the resulting broadening of the optical mode. Also the contribution of the absorption in the different layers to the total p-side losses changes. While for waveguide layers with lower Al contents and well confined modes the absorption in the $Al_{0.80}Ga_{0.20}N$:Mg cladding layer, the GaN:Mg contact layer and contact metal is in the same range, the contribution of the absorption in the cladding layer to the total losses becomes less relevant for less confined modes. Obviously,

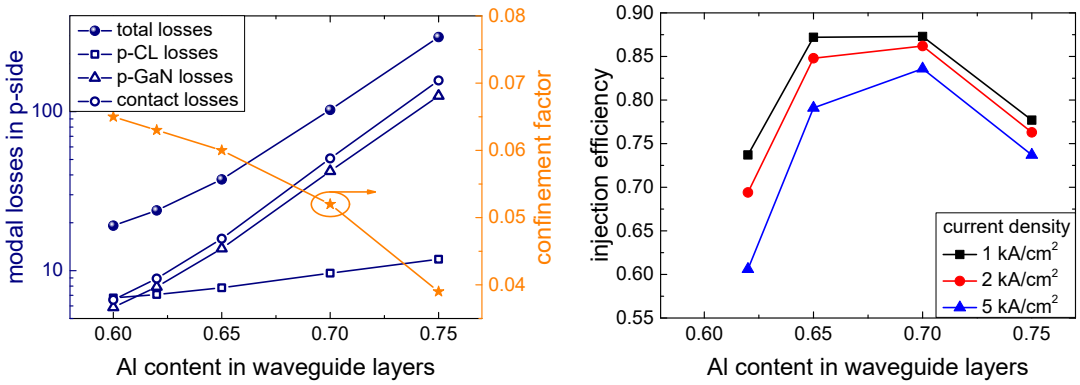

(a) p-side losses and confinement

(b) injection efficiency

Figure 5.23 Calculated modal losses in the p-side and confinement factor (a) and injection efficiency at different current densities (b) for a laser diode heterostructure with $Al_{0.80}Ga_{0.20}N$ cladding layers and different composition in the waveguide layers and quantum barriers. The upper waveguide layer is 30 nm thick.

limiting the overlap with the highly absorptive contact layer and metal is more critical than the overlap with the comparably transparent cladding layer. The total p-side losses reach values of more than 100 cm^{-1} for laser diode heterostructures with an Al content of 70 % or more in the waveguide layers. Those high losses can hardly be compensated by the gain provided by the active region. Also shown in Fig. 5.23(a) is the calculated confinement factor for the different waveguide compositions. With increasing Al content in the waveguide layers the confinement factor drops from 0.065 to less than 0.04 resulting in reduced modal gain. This additionally leads to higher carrier densities needed to overcome modal losses. Consequently, waveguide layers with an Al content of less than 70 % are needed in order to obtain current injection lasing. Additionally to this upper limit, a lower limit for the Al content in the waveguide layers is given by the need for efficient carrier injection. If the compositional contrast between waveguide layers or quantum barriers and QWs is too low, the carriers tend to escape from the QWs before recombination. The simulated injection efficiency for the different laser diode heterostructures is shown in Fig. 5.23(b) at different current densities between 1 kA/cm^2 and 5 kA/cm^2. At lower current densities the injection efficiency is constant at values of almost 0.9 in Al content range between 65 % and 70 %. For lower Al contents the efficiency drastically decreases due to the low potential barriers between QWs and quantum barriers or waveguide. For higher Al content in the waveguide the efficiency also decreases, because the potential barrier between EBL and waveguide is too small for efficient electron blocking. For higher current densities the injection efficiency decreases with a slight shift of the optimal waveguide composition to higher Al contents.

A different approach to minimize the optical losses originating in the p-side of the diodes is to increase the thickness of the undoped upper waveguide layer. This is shown in Fig. 5.24(a) for $Al_{0.62}Ga_{0.38}N$ waveguide layers with varying thicknesses of the upper waveguide layer between 5 nm and 100 nm (compare Fig. 5.22). By shifting the p-doped regions away from the active region, the mode overlap with those layers is reduced resulting in significantly lower optical losses. For upper waveguide thicknesses of 70 nm or more the intensity of the mode at the interface between p-cladding and GaN:Mg contact layer is low enough, that absorption in the contact layer and the contact metal can be neglected and the total p-side losses are estimated to be less than 10 cm^{-1}. On the other hand by increasing the thickness of the upper waveguide layer the waveguide becomes more and more asymmetric and the mode center is shifted towards the p-side. Also the increase of the total thickness of the waveguide leads to broadening of the mode. Both effects result in a drop of the confinement factor with increasing upper waveguide thickness of more than 30 nm.

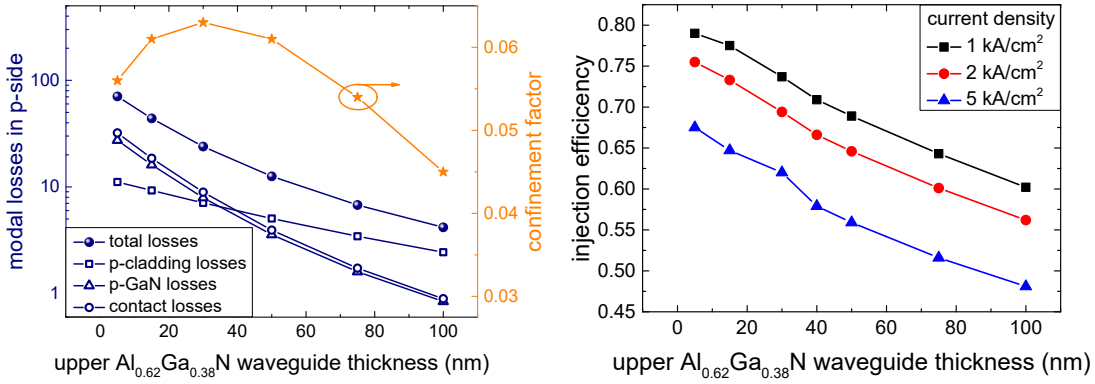

(a) p-side losses and confinement

(b) injection efficiency

Figure 5.24 Calculated modal losses in the p-side and confinement factor (a) and injection efficiency at different current densities (b) for a laser diode heterostructure with $Al_{0.80}Ga_{0.20}N$ cladding layers, $Al_{0.62}Ga_{0.38}N$ waveguide layers and different upper waveguide layer thicknesses.

For layer thickness smaller 30 nm the mode maximum is slightly shifted to the n-side, which also leads to smaller confinement factors.

The simulated injection efficiency for different upper waveguide layer thicknesses is shown in Fig. 5.24(b).With increasing spacing between the MQW and the EBL, which is located between the waveguide and cladding layer in the p-side, electrons overshooting the active region more likely recombine in the upper waveguide layer. This leads to significantly reduced injection efficiencies for thicker waveguide layers. For higher current densities the injection efficiency is further reduced, which makes this effect even more critical.

The analysis of the electrical performance of laser diode heterostructures with different composition in the $Al_xGa_{1-x}N$:Mg p-cladding layer as discussed in section 5.1.2 showed that the Al content strongly affects the turn-on voltage, series resistance, and consequently the operation voltage. From this perspective a lower Al content in the cladding layer would be preferable. However, by lowering the Al content in the p-cladding layer the waveguide structures becomes asymmetric. The refractive index contrast between waveguide and cladding layer on the p-side of the heterostructure is smaller compared to the n-side. As a result the mode is slightly shifted and broadened towards the p-side. This leads to an increase of the optical losses in the p-side. The calculated modal losses for a laser diode with 15 nm thick $Al_{0.62}Ga_{0.38}N$ upper waveguide for different composition in the upper cladding are shown in Fig. 5.25(a). Optical absorption in the GaN:Mg contact layer and contact metal dominate the modal losses for decreasing Al content in the p-cladding causing total losses of more than 700 cm^{-1}

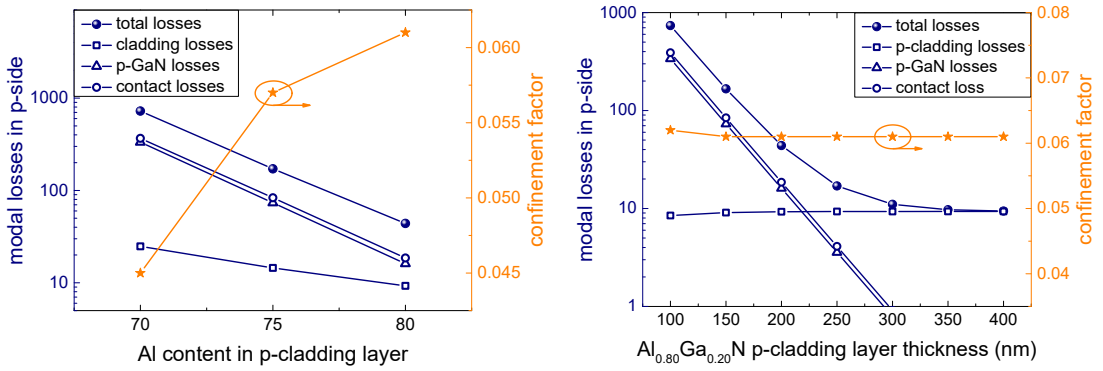

(a) p-cladding composition (b) p-cladding thickness

Figure 5.25 Calculated modal losses in the p-side and confinement factor for a laser diode heterostructure with $Al_{0.62}Ga_{0.38}N$ waveguide and quantum barriers, a 15 nm thick upper waveguide layer for different composition of a 200 nm thick p-cladding layer (a) and different thickness of an $Al_{0.80}Ga_{0.20}N$ p-cladding layer (b).

for $Al_{0.70}Ga_{0.30}N$ p-cladding layers. At the same time the confinement factor drops from more than 0.06 to about 0.045. This effect can partially be compensated by also reducing the Al content in the n-cladding layer for symmetric waveguide structures. In this case the optical mode is still broadened compared to higher Al content cladding layer but not shifted to the highly absorptive p-side resulting in modal losses of $\sim 200\,cm^{-1}$ and $\sim 100\,cm^{-1}$ for cladding layers with an Al content of 70 % and 75 % respectively (not shown). By designing an asymmetric waveguide structure with higher Al content in the p-side cladding compared to the n-side cladding layer the mode can be shifted towards the n-side, which results in drastically reduced modal losses in the p-side layers, e.g. less than $10\,cm^{-1}$ for a waveguide structure with an $Al_{0.80}Ga_{0.20}N$ p-cladding and an $Al_{0.70}Ga_{0.30}N$ n-cladding (not shown). However, the asymmetric mode distribution would again result in significantly reduced confinement factors and therefore lower the modal gain. Also, the tensile strain in the thick $Al_xGa_{1-x}N$:Si layer grown pseudomorphically with respect to the AlN template gives a lower limit for the Al content, which has not been studied in detail yet.

As a last design parameter, which affects the modal losses in the p-side, the thickness of the upper cladding layer is discussed. While the mode profile within the waveguide, and therefore the confinement factor is only slightly affected, the cladding layer thickness has significant influence on modal absorption as it determines the separation between the mode center and the highly absorptive GaN:Mg layer and contact metal. With decreasing cladding layer thickness the mode intensity at the interface between cladding and contact layer increases which results in an increase of the p-side losses up to more than $700\,cm^{-1}$ for a thickness of 100 nm (Fig. 5.25). For increasing thick-

ness the losses saturate at $\sim 10\,\mathrm{cm}^{-1}$ for thicknesses of more than 350 nm. In this case the losses are dominated by absorption in the cladding layer while the contact layer and metal have no influence. However, increasing the thickness of the rather resistive $Al_{0.80}Ga_{0.20}N$:Mg cladding layer increases the series resistance of the diode, which leads to increased operation voltage and Joule heating. First studies on the influence of the cladding layer thickness on the electrical characteristics show that in pulsed operation a heterostructure with a 300 nm thick $Al_{0.70}Ga_{0.30}N$:Mg cladding layer introduces an additional voltage drop of about 10 V compared to a diode with a 200 nm thick $Al_{0.70}Ga_{0.30}N$:Mg cladding layer in a current range between 5 mA and 50 mA. Therefore, before the series resistance of the diodes is significantly reduced by further optimization of the p-SPSL cladding layers, a 200 nm thick cladding layer seems to be a suitable compromise between comparably low optical losses and low operation voltage.

With the calculated modal losses and the confinement factor the material gain produced by the active region can be calculated which is necessary to overcome those losses and eventually enable laser operation. A heterostructure which provides a reasonable compromise between low modal losses and efficient carrier injection contains a 30 nm thick upper $Al_{0.65}Ga_{0.35}N$ waveguide layer with p-side losses of about $40\,\mathrm{cm}^{-1}$ and an injection efficiency of almost 0.9 for low currents (compare Fig. 5.23). In complete laser diode structures additional losses have to be considered adding to the p-side losses. Optical gain data show that a certain level of residual modal losses in the range of $10\,\mathrm{cm}^{-1}$ is present due to scattering or reabsorption processes independent of band to band absorption in the GaN contact layer, absorption in the contact metal or Mg-induced absorption in doped layers [119]. Also, in case of laser diodes with uncoated facets mirror losses have considerable contribution to the optical losses, e.g. $17\,\mathrm{cm}^{-1}$ for a 1 mm laser cavity ($n_{eff} \approx 2.5$), which could be considerably reduced by high reflection coatings. The total optical losses discussed sum up to a value of $67\,\mathrm{cm}^{-1}$, which corresponds to a required material gain of $\sim 1100\,\mathrm{cm}^{-1}$ in order to reach laser threshold. Those values can be reached for pumping powers twice the transparency pumping power as determined by optical gain data (see Fig. 5.20 in section 5.2.1). Assuming that in a first approximation the sheet carrier density is linear with pumping power this translates into carrier densities in the range of twice the transparency sheet carrier density. From numerical simulations a transparency sheet carrier density of $7.2 \times 10^{12}\,\mathrm{cm}^{-2}$ was derived for an AlGaN/AlGaN active region emitting at 270 nm [2]. This means that a sheet carrier density of $1.44 \times 10^{13}\,\mathrm{cm}^{-2}$ in the laser diode's active region is required to overcome the estimated total losses and reach threshold condition.

The carrier concentration in the active region of the laser diodes can easily be approximated for a given injection efficiency and carrier lifetime. The number of carriers injected is determined by the injected current density. The injection efficiency gives the portion of carriers eventually reaching the MQW active region. From the requirement of equilibrium between injection rate and recombination rate, which is represented by the carrier lifetime, the sheet carrier density can be calculated. Fig. 5.26 shows the sheet carrier density in the active region for different carrier lifetimes and the simulated injection efficiency for the laser diode heterostructure discussed above. Since the injection efficiency decreases for increasing current density the sheet carrier density is not linear with injected carriers but flattens towards higher currents. For a carrier lifetime of 1 ns transparency condition is reached for current density of 1.3 kA/cm^2 and laser threshold around 3 kA/cm^2. However, the carrier lifetime in the laser diodes is unknown and not independent of the current density. With increasing carrier density the radiative recombination rate increases quadratically decreasing the sheet carrier density. Therefore, it is plausible that at higher currents the carrier lifetimes are considerably lower than 1 ns which affects the threshold current density. For carrier lifetimes of 700 ps threshold condition is reached at 4 kA/cm^2 and for 700 ps at 6 kA/cm^2. In the case of very low lifetimes of 300 ps threshold current density shifts beyond 10 kA/cm^2. However, all number are reasonable current densities which can be obtained in semiconductor diodes. It was already shown, that current densities of more than 4.5 kA/cm^2 can be reached in a laser diode heterostructure with a mode guiding structure providing high mode confinement for laser emission of 270 nm [90]. As a limiting factor is the high operation voltage considered, which may cause Joule heating. This can drastically lower the injection efficiency and increase nonradiative recombination rates and therefore limit the carrier concentration. The presented results and considerations on the other hand prove with reduced sheet and

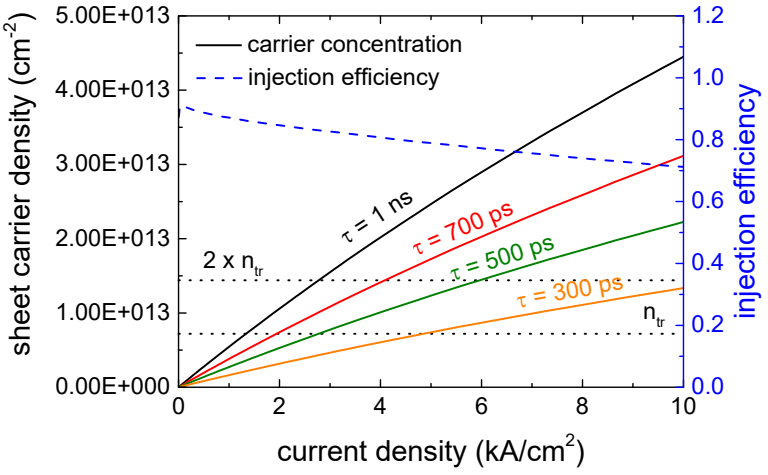

Figure 5.26 Calculated sheet carrier density in the active region of a laser diode for different carrier lifetimes. The carrier density is derived from equilibrium condition between generation and recombination rate. The injection efficiency is obtained from 2D device simulations.

contact resistivity by further process and design optimization and with the presented heterostructure design suggestions the feasibility of deep UV lasing from AlGaN based current injection laser diodes.

Chapter 6

Summary

Several aspects of the development of AlGaN based deep UV laser diodes including epitaxial growth, heterostructure design, and current injection were investigated in this work. The goal of the presented research was to provide deeper insight in the optical gain and modal loss in AlGaN MQW based active regions for deep UV lasers. So far no MQW based current injection laser diode emitting in the deep UV spectral region has been demonstrated. Critical aspects about the fabrication of deep UV laser diodes include material quality, optical confinement, carrier confinement, and hole injection. Each of the aforementioned aspects was addressed in order to systematically improve laser performance and identify limiting factors.

In a first step, optical and electrical issues were investigated individually. Optically pumped laser heterostructures were studied using spectroscopic methods including laser threshold measurements by excitation in stripe geometry and detection of MQW emission from the facet, determination of optical gain spectra by the variable stripe length method, and polarization selective spectroscopy. The current injection into AlGaN based MQW active regions was analyzed focusing on the hole injection and the laser diodes' p-cladding layers. The discussion was supported by numerical simulation of mode distribution, band structure and carrier transport. Findings from both perspectives were combined in order to derive a sophisticated concept for deep UV laser diode development.

All laser heterostructures discussed here were grown in [0001] direction on either sapphire or free standing AlN substrates by MOVPE. Optically pumped laser heterostructures consist of $Al_xGa_{1-x}N/Al_yGa_{1-y}N$ MQW active regions embedded in waveguide layers and a lower cladding layer. For emission between 250 nm and 300 nm $Al_{0.70}Ga_{0.30}N$ waveguide layers and a lower $Al_{0.80}Ga_{0.20}N$ cladding layer provide sufficient mode guiding for lasing. For wavelengths below 250 nm $Al_{0.80}Ga_{0.20}N$ waveguide and AlN cladding layers are used. The epitaxial layers are pseudomorphically strained with respect to the underlying relaxed AlN layer, indicating that no additional defects are formed by strain relaxation. The wafers were cleaved in m- and a-direction, respectively, in order to obtain resonator mirrors. No additional facet coating was

applied. With those heterostructures optically pumped lasing in a wavelength range from 237 nm to 293 nm is realized.
The influence of the defect density of the epitaxial layers on laser threshold and optical gain was investigated by studying MQWs for emission around 270 nm grown on different substrates. Lasing was observed with comparable laser threshold densities for MQWs grown on bulk AlN and ELO AlN/sapphire substrate with TDDs of $< 10^4\,\mathrm{cm}^{-2}$ and $5 \cdot 10^8\,\mathrm{cm}^{-2}$, respectively. Lasers grown on planar AlN/sapphire substrates with TDD in the range of $10^{10}\,\mathrm{cm}^{-2}$, on the other hand, do not reach laser threshold even for high pumping up to $50\,\mathrm{MW/cm}^2$, indicating that a critical value for non radiative recombination rates is reached. This observation was supported by temperature dependent PL measurements, showing that MQWs on bulk AlN and ELO AlN/sapphire substrates have comparable IQEs in the range of 20 % while the IQE of MQWs on planar AlN/sapphire substrates is about one order of magnitude lower. Additionally, it was found that scattering processes at macrosteps resulting from ELO process lead to an increase of the internal losses of $25\,\mathrm{cm}^{-1}$ and consequently an increased laser threshold. For AlGaN MQW laser heterostructures on optimized ELO AlN/sapphire substrates, laser threshold power densities of below $1\,\mathrm{MW/cm}^2$ for emission wavelength at around 270 nm was obtained.
By studying MQWs with different design, i.e. QW number, thickness, and composition, the influence of the optical as well as carrier confinement and carrier distribution on the optical gain and losses was investigated. The emission wavelength can be tuned by altering the Al content in the QWs. The optical polarization of MQW emission through the facet changes from TE to TM dominant emission with decreasing wavelength. Depending on the QW thickness and quantum barrier composition the transition was found to be in the range of 230 nm to 240 nm for MQW pseudomorphically strained with respect to the AlN. While for emission below threshold distribution of both polarizations could be observed, laser emission is strictly TE or TM polarized. For lasers in a wavelength range between 250 nm and 300 nm laser threshold power densities and optical gain characteristics are comparable, which was attributed to competing effects of increasing confinement factor and decreasing carrier confinement with increasing Al content in the QWs. The number and thickness of the QW on the other hand can have significant effect on the carrier distribution in the MQW and hence on the laser threshold, differential gain, and modal losses. The results suggest that best performance can be obtained for lasers with active regions consisting of a QW number in the range of three in matter of low laser thresholds, reduced modal losses, and high differential gain. For optically pumped lasers, an active region consisting of a threefold MQW with QW thicknesses of more than 4 nm seems to be

preferable in order to achieve low threshold power densities as they combine low optical losses, high confinement factor, and comparably homogeneous carrier distribution among the single QWs within the MQW.
In order to achieve current injection deep UV lasing from AlGaN based MQWs, high Al content p-side cladding layers are required. However, due to the high ionization energies of Mg acceptors in AlGaN increasing with higher Al content, conductivity of those layers is limited resulting in low hole densities and high operation voltages. The use of AlGaN short period super lattices (SPSL) has proven to efficiently lower the effective ionization energy. With an optimized SPSL deep UV AlGaN MQW separate confinement heterostructures for emission around 270 nm with high optical confinement of 4.6 % was designed and processed into broad area laser diodes. For this, a stripe-shaped Pd-based p-contact was deposited on the crystal surface and V-based n-contacts were deposited alongside the p-contact stripe after mesa etching. This structure is capable of withstanding current densities of almost 5 kA/cm^2 in pulsed operation. However, carrier density is still too low to achieve lasing. One limiting factor inhibiting laser operation is high modal losses in Mg-doped regions. In order to design an efficient laser diode heterostructure combining low optical losses and high injection efficiencies, the Mg-induced absorption was quantified by comparing the optical losses in optically pumped AlGaN laser heterostructures with different depth of Mg-doping in the upper waveguide layer. As a result the Mg-induced absorption in AlGaN based deep UV lasers could be quantified by 50 cm^{-1} x Γ_{Mg} with Γ_{Mg} being the mode overlap with the Mg-doped layers. This for the first time allows to conduct reliable device simulations in order to optimize the laser heterostructure design for high modal gain and low optical losses and give an approximation for the expected laser threshold current density. By this a laser diode heterostructure design for emission at 270 nm was suggested which is expected to exhibit lasing at current densities below 10 kA/cm^2 depending on the effective carrier life times. This structure contains an $Al_{0.46}Ga_{0.54}N/Al_{0.70}Ga_{0.70}N$ TQW active region, a thick lower n-$Al_{0.80}Ga_{0.20}N$ cladding layer, a 40 nm thick lower $Al_{0.70}Ga_{0.30}N$ waveguide layer, a 30 nm thick upper $Al_{0.65}Ga_{0.35}N$ waveguide layer, and a 200 nm thick upper p-$Al_{0.80}Ga_{0.20}N$ cladding layer. The calculated p-side losses are in the range of 40 cm^{-1}.
The presented results prove the feasibility of deep UV lasing from AlGaN based current injection laser diodes. However, further development of metal contacts especially on the p-side and the p-SPSL cladding layer is required in order to minimize thermal heating, reach high carrier densities and obtain deep UV lasing.

Bibliography

[1] S. Nakamura, S. Senoh, S. Nagahama, I. Iwasa, T. Yamada, T. Matsushita, H. Kiyoku, and Y. Sugimoto. InGaN-based multi-quantum-well-structure laser diodes. *Japanese Journal of Applied Physics*, 35(1B):L74, 1996.

[2] W. Chow and M. Kneissl. Laser gain properties of AlGaN quantum wells. *Journal of Applied Physics*, 98(11):114502, 2005.

[3] T. Wunderer, C. L. Chua, J. E. Northrup, Z. Yang, N. M. Johnson, M. Kneissl, G. A. Garrett, H. Shen, M. Wraback, B. Moody, H. S. Craft, R. Schlesser, R. F. Dalmau, and Z. Sitar. Optically pumped uv lasers grown on bulk AlN substrates. *physica status solidi (c)*, 9(3-4):822–825, 2012.

[4] Z. Lochner, T. Kao, Y. Liu, X. Li, M. Satter, S. Shen, P. Yoder, J. Ryou, R. Dupuis, Y. Wei, H. Xie, A. Fischer, and F. Ponce. Deep-ultraviolet lasing at 243 nm from photo-pumped AlGaN/AlN heterostructure on AlN substrate. *Applied Physics Letters*, 102(10):101110, 2013.

[5] J. Xie, S. Mita, Bryan. Z., W. Guo, L. Hussey, R. Moody, B. andl Schlesser, R. Kirste, M. Gerhold, R. Collazo, and Z. Sitar. Lasing and longitudinal cavity modes in photo-pumped deep ultraviolet AlGaN heterostructures. *Applied Physics Letters*, 102(17):171102, 2013.

[6] A. Kneissl, T. Kolbe, J. Schlegel, J. Stellmach, C. Chua, Z. Yang, A. Knauer, V. Kueller, M. Weyers, and N. Johnson. AlGaN-based ultraviolet lasers - applications and materials challenges. *CLEO:2011 - Laser Applications to Photonic Applications*, page JTuB1, 2011.

[7] H. Yoshida, Y. Yamashita, M. Kuwabara, and H. Kan. Demonstration of an ultraviolet 336 nm AlGaN multiple-quantum-well laser diode. *Applied Physics Letters*, 93(24):241106, 2008.

[8] S. Okawara, Y. Aoki, Y. Yamashita, and Y. Yoshida. *presented at 6th Int. Symp. Growth III–Nitrides (ISGN-6)*, 2015.

[9] T. Wunderer, C. Chua, Z. Yang, J. Northrup, N. Johnson, G. Garrett, H. Shen, and M. Wraback. Pseudomorphically grown ultraviolet c photopumped lasers on bulk aln substrates. *Applied Physics Express*, 4(9):092101, 2011.

[10] J. Jeschke, M. Martens, A. Knauer, V. Kueller, U. Zeimer, C. Netzel, C. Kuhn, F. Krueger, C. Reich, T. Wernicke, M. Kneissl, and M. Weyers. UV-C lasing from AlGaN multiple quantum wells on different types of AlN/sapphire templates. *IEEE Photonics Technology Letters*, 27(18):1969–1972, 2015.

[11] A. Wenzel. private communication.

[12] R. Goldhahn, S. Shokhovets, J. Scheiner, G. Gobsch, T.S. Cheng, C.T. Foxon, U. Kaiser, G.D. Kipshidze, and W. Richter. Determination of group III nitride film properties by reflectance and spectroscopic ellipsometry studies. *physica status solidi (a)*, 177(1):107–115, 2000.

[13] S. Shokhovets, R. Goldhahn, G. Gobsch, S. Piekh, R. Lantier, A. Rizzi, V. Lebedev, and W. Richter. Determination of the anisotropic dielectric function for wurtzite AlN and GaN by spectroscopic ellipsometry. *Journal of Applied Physics*, 94(1):307–312, 2003.

[14] N. A. Sanford, L. H. Robins, A. V. Davydov, A. Shapiro, D. V. Tsvetkov, A. V. Dmitriev, S. Keller, U. K. Mishra, and S. P. DenBaars. Refractive index study of $Al_xGa_{1-x}N$ films grown on sapphire substrates. *Journal of Applied Physics*, 94(5):2980–2991, 2003.

[15] L. A. Coldren and S. W. Corzine. *Diode Lasers and Photonic Integrated Circuits*. Wiley Interscience, 1995.

[16] A. Schleife, F. Fuchs, C. Rödl, J. Furthmüller, and F. Bechstedt. Branch-point energies and band discontinuities of III-nitrides and III-/II-oxides from quasiparticle band-structure calculations. *Applied Physics Letters*, 94(1):012104, 2009.

[17] SiLENSe. *STR Group, Inc.*, http://www.str-soft.com, Engels av. 27, P.O. Box 89, 194156, St.-Petersburg, Russia.

[18] S. C. Jain, Willander M., Narayan J., and R. Van Overstraeten. III–nitrides: Growth, characterization, and properties. *Journal of Applied Physics*, 87(3):965–1006, 2000.

[19] M.A. Herman, W Richter, and H. Sitter. *Epitaxy - Physical Principles and Technical Implementation*. Springer, 1 edition, 2004.

[20] U. W. Pohl. *Epitaxy of Semiconductors*. Springer, 1 edition, 2004.

[21] K. Ban, J. Yamamoto, K. Takeda, K. Ide, M. Iwaya, T. Takeuchi, S. Kamiyama, I. Akasaki, and H. Amano. Internal quantum efficiency of whole-composition-range AlGaN multiquantum wells. *Applied Physics Express*, 4(5):052101, 2011.

[22] C. Kuhn, M. Martens, F. Mehnke, J. Enslin, P. Schneider, C. Reich, F. Krueger, J. Rass, J. Park, V. Kueller, A. Knauer, T. Wernicke, M. Weyers, and M. Kneissl. Strain management and growth morphology of UV-C lasers. *Journal of Physics D: Applied Physics*, 2018.

[23] J.-R. van Look, S. Einfeldt, O. Kruger, V. Hoffmann, A Knauer, M. Weyers, P. Vogt, and M. Kneissl. Laser scribing for facet fabrication of InGaN MQW diode lasers on sapphire substrates. *IEEE Photonics Technology Letters*, 22(6):416–418, 2010.

[24] O. Krüger, J.-H. Kang, M. Spevak, U. Zeimer, and S. Einfeldt. Precision UV laser scribing for cleaving mirror facets of GaN-based laser diodes. *Applied Physics A*, 122(4):396, 2016.

[25] J.-H. Kang, O. Krüger, U. Spengler, U. Zeimer, S. Einfeldt, and M. Kneissl. On the formation of cleaved mirror facets of GaN-based laser diodes - A comparative study of diamond-tip edge-scribing and laser scribing. *Journal of Vacuum Science & Technology B, Nanotechnology and Microelectronics: Materials, Processing, Measurement, and Phenomena*, 34(4):041222, 2016.

[26] Coherent Inc. www.coherent.com.

[27] K. L. Shaklee and R. F. Leheny. Direct determination of optical gain in semiconductor crystals. *Applied Physics Letters*, 18(11):475–477, 1971.

[28] K. Kyhm, R. A. Taylor, J. F. Ryan, T. Someya, and Y. Arakawa. Analysis of gain saturation in $In_{0.02}Ga_{0.98}N/In_{0.16}Ga_{0.84}N$ multiple quantum wells. *Applied Physics Letters*, 79(21):3434–3436, 2001.

[29] J. F. Muth, J. H. Lee, I. K. Shmagin, R. M. Kolbas, H. C. Casey, B. P. Keller, U. K. Mishra, and S. P. DenBaars. Absorption coefficient, energy gap, exciton binding energy, and recombination lifetime of GaN obtained from transmission measurements. *Applied Physics Letters*, 71(18):2572–2574, 1997.

[30] M. Martens, F. Mehnke, C. Kuhn, C. Reich, V. Kueller, A. Knauer, C. Netzel, C. Hartmann, J. Wollweber, J. Rass, T. Wernicke, M. Bickermann, M. Weyers, and M. Kneissl. Performance characteristics of UV-C AlGaN-based lasers grown on sapphire and bulk AlN substrates. *IEEE Photonics Technology Letters*, 26(4):342–345, 2014.

[31] T. Takano, Y. Narita, A. Horiuchi, and H. Kawanishi. Room-temperature deep-ultraviolet lasing at 241.5 nm of AlGaN multiple-quantum-well laser. *Applied Physics Letters*, 84(18):3567–3569, 2004.

[32] T. Takano, Y. Ohtaki, Y. Narita, and H. Kawanishi. Improvement of crystal quality of AlGaN multi quantum well structure by combination of flow-rate modulation epitaxy and AlN/GaN multi-buffer layer and resultant lasing at deep ultra-violet region. *Japanese Journal of Applied Physics*, 43(10A):L1258, 2004.

[33] H. Kawanishi, M. Senuma, and T. Nukui. Anisotropic polarization characteristics of lasing and spontaneous surface and edge emissions from deep-ultraviolet ($\lambda \approx$240nm) AlGaN multiple-quantum-well lasers. *Applied Physics Letters*, 89(4):041126, 2006.

[34] V. N. Jmerik, E. V. Lutsenko, and S. V. Ivanov. Plasma-assisted molecular beam epitaxy of AlGaN heterostructures for deep-ultraviolet optically pumped lasers. *physica status solidi (a)*, 210(3):439–450, 2013.

[35] M. Kneissl and J. Rass. *III-Nitride Ultraviolet Emitters*. Springer, 1 edition, 2016.

[36] V. Hoffmann, A. Mogilatenko, C. Netzel, U. Zeimer, S. Einfeldt, M. Weyers, and M. Kneissl. Influence of barrier growth schemes on the structural properties and thresholds of InGaN quantum well laser diodes. *Journal of Crystal Growth*, 391(Supplement C):46 – 51, 2014.

[37] S. Yamaguchi, M. Kosaki, Y. Watanabe, Y. Yukawa, S. Nitta, H. Amano, and I. Akasaki. Metalorganic vapor phase epitaxy growth of crack-free AlN on GaN and its application to high-mobility AlN/GaN superlattices. *Applied Physics Letters*, 79(19):3062–3064, 2001.

[38] C. Hartmann, J. Wollweber, A. Dittmar, K. Irmscher, A. Kwasniewski, F. Langhans, T. Neugut, and M. Bickermann. Preparation of bulk AlN seeds by sponta-

neous nucleation of freestanding crystals. *Japanese Journal of Applied Physics*, 52(8S):08JA06, 2013.

[39] O. Reentilä, F. Brunner, A. Knauer, A. Mogilatenko, W. Neumann, H. Protzmann, M. Heuken, M. Kneissl, M. Weyers, and G. Tränkle. Effect of the AiN nucleation layer growth on AlN material quality. *Journal of Crystal Growth*, 310(23):4932 – 4934, 2008.

[40] V. Kueller, A. Knauer, F. Brunner, U. Zeimer, H. Rodriguez, M. Kneissl, and M. Weyers. Growth of AlGaN and AlN on patterned AlN/sapphire templates. *Journal of Crystal Growth*, 315(1):200 – 203, 2011.

[41] V. Kueller, A. Knauer, C. Reich, A. Mogilatenko, M. Weyers, J. Stellmach, T. Wernicke, M. Kneissl, Z. Yang, C. L. Chua, and N. M. Johnson. Modulated epitaxial lateral overgrowth of AlN for efficient UV LEDs. *IEEE Photonics Technology Letters*, 24(18):1603–1605, 2012.

[42] M. Reich, M. Feneberg, V. Kueller, A. Knauer, T. Wernicke, J. Schlegel, M. Frentrup, R. Goldhahn, M. Weyers, and M. Kneissl. Excitonic recombination in epitaxial lateral overgrown AlN on sapphire. *Applied Physics Letters*, 103(21):212108, 2013.

[43] U. Zeimer, Z. Kueller, A. Knauer, A. Mogilatenko, W. Weyers, and M. Kneissl. High quality AlGaN grown on ELO AlN/sapphire templates. *Journal of Crystal Growth*, 377(Supplement C):32 – 36, 2013.

[44] V. Kueller. *Versetzungsreduzierte AlN- und AlGaN-Schichten als Basis für UV LEDs*. PhD thesis, Technische Universität Berlin, 2014.

[45] V. Kueller, A. Knauer, U. Zeimer, H. Rodriguez, A. Mogilatenko, M. Kneissl, and M. Weyers. (Al,Ga)N overgrowth over AlN ridges oriented in [1120] and [1100] direction. *physica status solidi (c)*, 8(7-8):2022–2024, 2011.

[46] M. Kneissl, Z. Yang, M. Teepe, C. Knollenberg, O. Schmidt, P. Kiesel, N. Johnson, S Schujman, and L. Schowalter. Ultraviolet semiconductor laser diodes on bulk AlN. *Journal of Applied Physics*, 101(12):123103, 2007.

[47] U. Zeimer, J. Jeschke, A. Mogilatenko, A. Knauer, V. Kueller, V. Hoffmann, C. Kuhn, T. Simoneit, M. Martens, T. Wernicke, M. Kneissl, and M. Weyers. Spatial inhomogeneities in $Al_xGa_{1-x}N$ quantum wells induced by the surface morphology of AlN/sapphire templates. *Semiconductor Science and Technology*, 30(11):114008, 2015.

[48] A. Mogilatenko, V. Küller, A. Knauer, J. Jeschke, U. Zeimer, M. Weyers, and G. Tränkle. Defect analysis in AlGaN layers on AlN templates obtained by epitaxial lateral overgrowth. *Journal of Crystal Growth*, 402(Supplement C):222 – 229, 2014.

[49] A. Knauer, A. Mogilatenko, S. Hagedorn, J. Enslin, T. Wernicke, M. Kneissl, and M. Weyers. Correlation of sapphire off-cut and reduction of defect density in MOVPE grown AlN. *physica status solidi (b)*, 253(5):809–813, 2016.

[50] H. K. Cho, J. Y. Lee, and G. M. Yang. Characterization of pit formation in III-nitrides grown by metalorganic chemical vapor deposition. *Applied Physics Letters*, 80(8):1370–1372, 2002.

[51] L. Huang, F. Liu, F. Zhu, R. Kamaladasa, E. Preble, T. Paskova, K. Evans, L. Porter, Y. Picard, and R. Davis. Microstructure of epitaxial GaN films grown on chemomechanically polished GaN(0001) substrates. *Journal of Crystal Growth*, 347(1):88 – 94, 2012.

[52] J. Enslin, A. Knauer, A. Mogilatenko, F. Mehnke, M. Martens, C. Kuhn, K. Bellmann, T. Wernicke, M. Weyers, and M. Kneissl. Determination and influence of sapphire off-cut on the morphology and local defect distribution in epitaxially laterally overgrown AlN. *to be published*, 2018.

[53] K. Shima, K. Segi, H. Imai, T. Fujiwara, and M. Takusagawa. Effect of growth terraces on threshold current density of (GaAl)As double-heterostructure laser. *Applied Physics Letters*, 37(4):341–343, 1980.

[54] J. Jeschke, M. Martens, S. Hagedorn, A. Knauer, A. Mogilatenko, H. Wenzel, U. Zeimer, J. Enslin, T. Wernicke, M. Kneissl, and M. Weyers. Influence of template properties and quantum well number on stimulated emission from $Al_{0.7}Ga_{0.3}N/Al_{0.8}Ga_{0.2}N$ quantum wells. *Semiconductor Science and Technology*, 33(3):035015, 2018.

[55] H. Wang, J. Zhang, C. Chen, Q. Fareed, J. Yang, and Khan A. AlN/AlGaN superlattices as dislocation filter for low-threading-dislocation thick AlGaN layers on sapphire. *Applied Physics Letters*, 81(4):604–606, 2002.

[56] T. Wang, Y. Liu, Y. Lee, Y. Izumi, J. Ao, J. Bai, H. Li, and S. Sakai. Fabrication of high performance of AlGaN/GaN-based UV light-emitting diodes. *Journal of Crystal Growth*, 235(1):177 – 182, 2002.

[57] N. Nakada, H. Ishikawa, T. Egawa, and J. Jimbo. Suppression of crack generation in GaN/AlGaN distributed bragg reflector on sapphire by the insertion of GaN/AlGaN superlattice grown by metal-organic chemical vapor deposition. *Japanese Journal of Applied Physics*, 42(2B):L144, 2003.

[58] C. Kuhn, T. Simoneit, M. Martens, T. Markurt, J. Enslin, F. Mehnke, K. Bellmann, T. Schulz, M. Albrecht, T. Wernicke, and M. Kneissl. MOVPE growth of smooth and homogeneous $Al_{0.8}Ga_{0.2}N$:Si superlattices as UVC laser cladding layers. *physica status solidi (a)*, 215(13):1800005.

[59] T. Kolbe, T. Sembdner, A. Knauer, V. Kueller, H. Rodriguez, S. Einfeldt, P. Vogt, M. Weyers, and M. Kneissl. (In)AlGaN deep ultraviolet light emitting diodes with optimized quantum well width. *physica status solidi (a)*, 207(9):2198–2200, 2010.

[60] K. B. Nam, J. Li, M. L. Nakarmi, J. Y. Lin, and B. X. Jiang. Unique optical properties of AlGaN alloys and related ultraviolet emitters. *Applied Physics Letters*, 84(25):5264–5266, 2004.

[61] T. Kolbe, A. Knauer, C. Chua, Z. Yang, S. Einfeldt, P. Vogt, N. M. Johnson, M. Weyers, and M. Kneissl. Optical polarization characteristics of ultraviolet (In)(Al)GaN multiple quantum well light emitting diodes. *Applied Physics Letters*, 97(17):171105, 2010.

[62] T. Kolbe, A. Knauer, C. Chua, Z. Yang, V. Kueller, S. Einfeldt, P. Vogt, N. M. Johnson, M. Weyers, and M. Kneissl. Effect of temperature and strain on the optical polarization of (In)(Al)GaN ultraviolet light emitting diodes. *Applied Physics Letters*, 99(26):261105, 2011.

[63] J. E. Northrup, C. L. Chua, Z. Yang, T. Wunderer, M. Kneissl, N. M. Johnson, and T. Kolbe. Effect of strain and barrier composition on the polarization of light emission from AlGaN/AlN quantum wells. *Applied Physics Letters*, 100(2):021101, 2012.

[64] B. Neuschl, J. Helbing, M. Knab, H. Lauer, M. Madel, K. Thonke, T. Meisch, K. Forghani, F. Scholz, and M. Feneberg. Composition dependent valence band order in c-oriented wurtzite AlGaN layers. *Journal of Applied Physics*, 116(11):113506, 2014.

[65] C. Reich, M. Guttmann, M. Feneberg, T. Wernicke, F. Mehnke, C. Kuhn, J. Rass, M. Lapeyrade, S. Einfeldt, A. Knauer, V. Kueller, M. Weyers, R. Gold-

hahn, and M. Kneissl. Strongly transverse-electric-polarized emission from deep ultraviolet AlGaN quantum well light emitting diodes. *Applied Physics Letters*, 107(14):142101, 2015.

[66] R. Ishii, A. Kaneta, M. Funato, Y. Kawakami, and A. A. Yamaguchi. All deformation potentials in GaN determined by reflectance spectroscopy under uniaxial stress: Definite breakdown of the quasicubic approximation. *Phys. Rev. B*, 81:155202, 2010.

[67] M. Feneberg, M. F. Romero, M. Röppischer, C. Cobet, N. Esser, B. Neuschl, K. Thonke, M. Bickermann, and R. Goldhahn. Anisotropic absorption and emission of bulk $(1\bar{1}00)$ AlN. *Phys. Rev. B*, 87:235209, 2013.

[68] B. Monemar. Fundamental energy gap of GaN from photoluminescence excitation spectra. *Phys. Rev. B*, 10:676–681, 1974.

[69] G. Bastard, E. E. Mendez, L. L. Chang, and L. Esaki. Exciton binding energy in quantum wells. *Phys. Rev. B*, 26:1974–1979, 1982.

[70] R. P. Leavitt and J. W. Little. Simple method for calculating exciton binding energies in quantum-confined semiconductor structures. *Phys. Rev. B*, 42:11774–11783, 1990.

[71] L. Q. Zhang, D. S. Jiang, J. J. Zhu, D. G. Zhao, Z. S. Liu, S. M. Zhang, and H. Yang. Confinement factor and absorption loss of AlInGaN based laser diodes emitting from ultraviolet to green. *Journal of Applied Physics*, 105(2):023104, 2009.

[72] E. F. Schubert, E. O. Göbel, Y. Horikoshi, K. Ploog, and H. J. Queisser. Alloy broadening in photoluminescence spectra of $Al_xGa_{1-x}As$. *Phys. Rev. B*, 30:813–820, 1984.

[73] B.K. Meyer, G. Steude, A. Göldner, A. Hoffmann, H. Amano, and I. Akasaki. Photoluminescence investigations of AlGaN on GaN epitaxial films. *physica status solidi (b)*, 216(1):187–191, 1999.

[74] K. Kojima, M. Funato, Y. Kawakami, H. Braun, U. Schwarz, S. Nagahama, and T. Mukai. Inhomogeneously broadened optical gain spectra of InGaN quantum well laser diodes. *physica status solidi (c)*, 5(6):2126–2128, 2008.

[75] J. Müller, U. Strauß, T. Lermer, G. Brüderl, C. Eichler, A. Avramescu, and S. Lutgen. Investigation of long wavelength green InGaN lasers on c-plane

GaN up to 529 nm continuous wave operation. *physica status solidi (a)*, 208(7):1590–1592, 2011.

[76] D. Brunner, H. Angerer, E. Bustarret, F. Freudenberg, R. Höpler, R. Dimitrov, O. Ambacher, and M. Stutzmann. Optical constants of epitaxial AlGaN films and their temperature dependence. *Journal of Applied Physics*, 82(10):5090–5096, 1997.

[77] C.-K. Sun, T.-L. Chiu, S. Keller, G. Wang, M. S. Minsky, S. P. DenBaars, and J. E. Bowers. Time-resolved photoluminescence studies of InGaN/GaN single-quantum-wells at room temperature. *Applied Physics Letters*, 71(4):425–427, 1997.

[78] D. L. Becerra, D. A. Cohen, R. M. Farrell, S. P. DenBaars, and S. Nakamura. Effects of active region design on gain and carrier injection and transport of cw $(20\bar{2}\bar{1})$ semipolar InGaN laser diodes. *Applied Physics Express*, 9(9):092104, 2016.

[79] M. Leroux, F. Semond, F. Natali, D. Byrne, F. Cadoret, B. Damilano, A. Dussaigne, N. Grandjean, A. Le Louarn, S. Vézian, and J. Massies. About some optical properties of $Al_xGa_{1-x}N$/GaN quantum wells grown by molecular beam epitaxy. *Superlattices and Microstructures*, 36(4):659 – 674, 2004.

[80] M. Zhang, P. Bhattacharya, J. Singh, and J. Hinckley. Direct measurement of auger recombination in $In_{0.1}Ga_{0.9}N$/GaN quantum wells and its impact on the efficiency of $In_{0.1}Ga_{0.9}N$/GaN multiple quantum well light emitting diodes. *Applied Physics Letters*, 95(20):201108, 2009.

[81] G. A. Garrett, A. V. Sampath, H. Shen, M. Wraback, W. Sun, M. Shatalov, X. Hu, J. Yang, Y. Bilenko, A. Lunev, M. S. Shur, R. Gaska, J. R. Grandusky, and L. J. Schowalter. Evaluation of AlGaN-based deep ultraviolet emitter active regions by temperature dependent time-resolved photoluminescence. *physica status solidi (c)*, 7(10):2390–2393, 2010.

[82] S. F. Chichibu, H. Miyake, Y. Ishikawa, M. Tashiro, T. Ohtomo, K. Furusawa, K. Hazu, K. Hiramatsu, and A. Uedono. Impacts of si-doping and resultant cation vacancy formation on the luminescence dynamics for the near-band-edge emission of $Al_{0.6}Ga_{0.4}N$ films grown on AlN templates by metalorganic vapor phase epitaxy. *Journal of Applied Physics*, 113(21):213506, 2013.

[83] P. Scajev, S. Miasojedovas, K. Jarašiunas, K. Hiramatsu, H. Miyake, and B. Gil. Excitation-dependent carrier dynamics in Al-rich AlGaN layers and multiple quantum wells. *physica status solidi (b)*, 252(5):1043–1049, 2015.

[84] W. W. Chow, H. Amano, T. Takeuchi, and J. Han. Quantum-well width dependence of threshold current density in InGaN lasers. *Applied Physics Letters*, 75(2):244–246, 1999.

[85] J. Mickevicius, G. Tamulaitis, E. Kuokstis, K. Liu, M. S. Shur, J. P. Zhang, and R. Gaska. Well-width-dependent carrier lifetime in AlGaN/AlGaN quantum wells. *Applied Physics Letters*, 90(13):131907, 2007.

[86] P. B. Johnson and R. W. Christy. Optical constants of transition metals: Ti, V, Cr, Mn, Fe, Co, Ni, and Pd. *Phys. Rev. B*, 9:5056–5070, 1974.

[87] F. Mehnke, C. Kuhn, M. Guttmann, C. Reich, T. Kolbe, V. Kueller, A. Knauer, M. Lapeyrade, S. Einfeldt, J. Rass, T. Wernicke, M Weyers, and M. Kneissl. Efficient charge carrier injection into sub-250 nm AlGaN multiple quantum well light emitting diodes. *Applied Physics Letters*, 105(5):051113, 2014.

[88] F. Mehnke, C Kuhn, J. Stellmach, T. Kolbe, N. Lobo-Ploch, J. Rass, M. Rothe, C. Reich, N. Ledentsov, M. Pristovsek, T. Wernicke, and M. Kneissl. Effect of heterostructure design on carrier injection and emission characteristics of 295 nm light emitting diodes. *Journal of Applied Physics*, 117(19):195704, 2015.

[89] T. Kolbe, F. Mehnke, M. Guttmann, C. Kuhn, J. Rass, T. Wernicke, and M. Kneissl. Improved injection efficiency in 290 nm light emitting diodes with Al(Ga)N electron blocking heterostructure. *Applied Physics Letters*, 103(3):031109, 2013.

[90] M. Martens, C. Kuhn, E. Ziffer, T. Simoneit, V. Kueller, A. Knauer, J. Rass, T. Wernicke, S. Einfeldt, M. Weyers, and M. Kneissl. Low absorption loss p-AlGaN superlattice cladding layer for current-injection deep ultraviolet laser diodes. *Applied Physics Letters*, 108(15):151108, 2016.

[91] R. Collazo, S. Mita, J. Xie, A. Rice, J. Tweedie, R. Dalmau, and Z. Sitar. Progress on n-type doping of AlGaN alloys on AlN single crystal substrates for UV optoelectronic applications. *physica status solidi (c)*, 8(7-8):2031–2033, 2011.

[92] F. Mehnke, T. Wernicke, H. Pingel, C. Kuhn, C. Reich, V. Kueller, A. Knauer, M. Lapeyrade, M. Weyers, and M. Kneissl. Highly conductive n-$Al_xGa_{1-x}N$ layers with aluminum mole fractions above 80%. *Applied Physics Letters*, 103(21):212109, 2013.

[93] T. Tanaka, A. Watanabe, H. Amano, Y. Kobayashi, I. Akasaki, S. Yamazaki, and M. Koike. p-type conduction in Mg-doped GaN and $Al_{0.08}Ga_{0.92}N$ grown by metalorganic vapor phase epitaxy. *Applied Physics Letters*, 65(5):593–594, 1994.

[94] W. Götz, N. M. Johnson, J. Walker, D. P. Bour, and R. A. Street. Activation of acceptors in Mg-doped GaN grown by metalorganic chemical vapor deposition. *Applied Physics Letters*, 68(5):667–669, 1996.

[95] H. Nakayama, P. Hacke, M. R. H. Khan, T. Detchprohm, K. Hiramatsu, and N. Sawaki. Electrical transport properties of p-GaN. *Japanese Journal of Applied Physics*, 35(3A):L282, 1996.

[96] M. Suzuki, J. Nishio, M. Onomura, and C. Hongo. Doping characteristics and electrical properties of Mg-doped AlGaN grown by atmospheric-pressure MOCVD. *Journal of Crystal Growth*, 189–190:511 – 515, 1998.

[97] J. Li, T. N. Oder, M. L. Nakarmi, J. Y. Lin, and H. X. Jiang. Optical and electrical properties of Mg-doped p-type $Al_xGa_{1-x}N$. *Applied Physics Letters*, 80(7):1210–1212, 2002.

[98] K. B. Nam, M. L. Nakarmi, J. Li, J. Y. Lin, and H. X. Jiang. Mg acceptor level in AlN probed by deep ultraviolet photoluminescence. *Applied Physics Letters*, 83(5):878–880, 2003.

[99] M. L. Nakarmi, K. H. Kim, M. Khizar, Z. Y. Fan, J. Y. Lin, and H. X. Jiang. Electrical and optical properties of Mg-doped $Al_{0.7}Ga_{0.3}N$ alloys. *Applied Physics Letters*, 86(9):092108, 2005.

[100] M. L. Nakarmi, N. Nepal, C. Ugolini, T. M. Altahtamouni, J. Y. Lin, and H. X. Jiang. Correlation between optical and electrical properties of Mg-doped AlN epilayers. *Applied Physics Letters*, 89(15):152120, 2006.

[101] T. Taniyasu, M. Kasu, and T. Makimoto. An aluminium nitride light-emitting diode with a wavelength of 210 nanometres. *Nature*, 441:325–328, 2006.

[102] E. F. Schubert, W. Grieshaber, and I. D. Goepfert. Enhancement of deep acceptor activation in semiconductors by superlattice doping. *Applied Physics Letters*, 69(24):3737–3739, 1996.

[103] A. Saxler, W. C. Mitchel, P. Kung, and M. Razeghi. Aluminum gallium nitride short-period superlattices doped with magnesium. *Applied Physics Letters*, 74(14):2023–2025, 1999.

[104] P. Kozodoy, M. Hansen, S. P. DenBaars, and U. K. Mishra. Enhanced Mg doping efficiency in $Al_{0.2}Ga_{0.8}N$/GaN superlattices. *Applied Physics Letters*, 74(24):3681–3683, 1999.

[105] I. D. Goepfert, E. F. Schubert, A. Osinsky, and P. E. Norris. Demonstration of efficient p-type doping in $Al_xGa_{1-x}N$/GaN superlattice structures. *Electronics Letters*, 35:1109–1111(2), 1999.

[106] A. A. Allerman, M. H. Crawford, M. A. Miller, and S. R. Lee. Growth and characterization of Mg-doped AlGaN–AlN short-period superlattices for deep-UV optoelectronic devices. *Journal of Crystal Growth*, 312(6):756 – 761, 2010.

[107] B. Cheng, S. Choi, J. E. Northrup, Z. Yang, C. Knollenberg, M. Teepe, T. Wunderer, C. L. Chua, and N. M. Johnson. Enhanced vertical and lateral hole transport in high aluminum-containing AlGaN for deep ultraviolet light emitters. *Applied Physics Letters*, 102(23):231106, 2013.

[108] F. Bernardini, V. Fiorentini, and D. Vanderbilt. Spontaneous polarization and piezoelectric constants of III-V nitrides. *Phys. Rev. B*, 56:R10024–R10027, Oct 1997.

[109] D. A. B. Miller. *Quantum Mechanics for Scientists and Engineers*. Cambridge University Press, 2012.

[110] M. Kuramoto, C. Sasaoka, N. Futagawa, M. Nido, and A. A. Yamaguchi. Reduction of internal loss and threshold current in a laser diode with a ridge by selective re-growth (RiS-LD). *physica status solidi (a)*, 192(2):329–334, 2002.

[111] D. Sizov, B. Rajaram, and C. Zah. Optical absorption of Mg-doped layers and InGaN quantum wells on c-plane and semipolar GaN structures. *Journal of Applied Physics*, 113(20):203108, 2013.

[112] J. Nishinaka, M. Funato, R. Kido, and Y. Kawakami. InGaN/AlGaN stress compensated superlattices coherently grown on semipolar (11-22) GaN substrates. *physica status solidi (b)*, 253(1):78–83, 2016.

[113] C. J. Deatcher, K. Bejtka, R. W. Martin, S. Romani, H. Kheyrandish, L. M. Smith, S. A. Rushworth, C. Liu, M. G. Cheong, and I. M. Watson. Wavelength-dispersive x-ray microanalysis as a novel method for studying magnesium doping in gallium nitride epitaxial films. *Semiconductor Science and Technology*, 21(9):1287, 2006.

[114] T. Kolbe. *Einfluss des Heterostrukturdesigns auf die Effizienz und die optische Polarisation von (In)AlGaN-basierten Leuchtdioden im ultravioletten Spektralbereich*. PhD thesis, Technische Universität Berlin, 2012.

[115] D. K. Schroder. *semiconductor material and device characterization*. Wiley, 3 edition, 2006.

[116] M. Lapeyrade, Muhin A., Einfeldt S., U. Zeimer, A. Mogilatenko, M. Weyers, and M. Kneissl. Electrical properties and microstructure of vanadium-based contacts on ICP plasma etched n-type AlGaN:Si and GaN:Si surfaces. *Semiconductor Science and Technology*, 28(12):125015, 2013.

[117] Picosecond Pulse Labs, Inc. https://www.tek.com/picosecond-pulse-labs-now-part-tektronix.

[118] A. A. Efremov, D. V. Tarkhin, N. I. Bochkareva, R. I. Gorbunov, Yu. T. Rebane, and Yu. G. Shreter. Determination of the coefficient of light attenuation in thin layers of light-emitting diodes. *Semiconductors*, 40(3):375–378, 2006.

[119] M. Martens, C. Kuhn, T. Simoneit, S. Hagedorn, A. Knauer, T. Wernicke, M. Weyers, and M Kneissl. The effects of magnesium doping on the modal loss in AlGaN-based deep UV lasers. *Applied Physics Letters*, 110(8):081103, 2017.

[120] L. T. Romano, J. E. Northrup, A. J. Ptak, and T. H. Myers. Faceted inversion domain boundary in GaN films doped with Mg. *Applied Physics Letters*, 77(16):2479, 2000.

[121] L. T. Romano, M. Kneissl, J. E. Northrup, C. G. Van de Walle, and D. W. Treat. Influence of microstructure on the carrier concentration of Mg-doped GaN films. *Applied Physics Letters*, 79(17):2734–2736, 2001.

[122] D. Sizov, R. Bhat, A. Heberle, K. Song, and C. Zah. Internal optical waveguide loss and p-type absorption in blue and green ingan quantum well laser diodes. *Applied Physics Express*, 3(12):122104, 2010.

[123] E. Kioupakis, P. Rinke, A. Schleife, F. Bechstedt, and C. G. Van de Walle. Free-carrier absorption in nitrides from first principles. *Phys. Rev. B*, 81:241201, 2010.

List of publications

Parts of this work have been published as listed below:

Articles

- C. Kuhn, **M. Martens**, F. Mehnke, J. Enslin, P. Schneider, C. Reiche, F. Krueger, J. Rass, J. Park, V. Kueller, A. Knauer, T. Wernicke, M. Weyers, and M. Kneissl. Strain Management and Growth Morphology of UV-C Lasers. *accepted for publication in Journal of Physics D: Applied Physics*, 2018.

- C. Kuhn, T. Simoneit, **M. Martens**, T. Markurt, J. Enslin, F. Mehnke, K. Bellmann, T. Schulz, M. Albrecht, T. Wernicke, and M. Kneissl. MOVPE growth of smooth and homogeneous $Al_{0.8}Ga_{0.2}N$:Si superlattices as UVC laser cladding layers. *accepted for publication in physica status solidi (a)*, 2018.

- J. Jeschke, **M. Martens**, S. Hagedorn, A. Knauer, A. Mogilatenko, H. Wenzel, U. Zeimer, J. Enslin, T. Wernicke, M. Kneissl, and M. Weyers. Influence of template properties and quantum well thickness on stimulated emission from $Al_{0.7}Ga_{0.3}N/Al_{0.8}Ga_{0.2}N$ quantum wells. *Semiconductor Science and Technology*, 33(3):035015, 2018.

- **M. Martens**, C. Kuhn, T. Simoneit, S. Hagedorn, A. Knauer, T. Wernicke, M. Weyers, and Michael Kneissl. The effects of magnesium doping on the modal loss in AlGaN-based deep UV lasers. *Applied Physics Letters*, 110(8):081103, 2017.

- **M. Martens**, C. Kuhn, E. Zifferm T. Simoneit, V. Kueller, A. Knauer, J. Rass, T. Wernicke, S. Einfldt, M. Weyers, and M. Kneissl. Low absorption loss p-AlGaN superlattice cladding layer for current-injection deep ultraviolet laser diodes, *Applied Physics Letters* 108(15):151108, 2016.

- U. Zeimer, J. Jeschke, A. Mogilatenko, A. Knauer, V. Kueller, V. Hoffmann, C. Kuhn, T. Simoneit, **M. Martens**, T. Wernicke, M. Kneissl, and M. Weyers. Spatial inhomogeneities in $Al_xGa_{1-x}N$ quantum wells induced by the surface morphology of AlN/sapphire templates. *Semiconductor Science and Technology*, 30(11):114008, 2015

- J. Jeschke, **M. Martens**, A. Knauer, V. Kueller, U. Zeimer, C. Netzel, C. Kuhn, F. Krueger, C. Reich, T. wernicke, M. Kneissl, and M. Weyers. UV-C lasing from AlGaN multiple quantum wells on different types of AlN/sapphire templates. *IEEE Photonics Technology Letters*, 27(18):1969-1972, 2015.

- **M. Martens**, F. Mehnke, C. Kuhn, C. Reich, V. Kueller, A. Knauer, C. Netzel, C. Hartmann, J. Wollweber, J. Rass, T. Wernicke, M. Bickermann, M. Weyers, and M. Kneissl. Performance characteristics of UV-C AlGaN-based lasers grown on sapphire and bulk AlN substrates. *IEEE Photonics Technology Letters*, 26(4):342-345, 2014.

International conferences

- M. Martens, P. Schneider, C. Kuhn, F. Mehnke, J. Jeschke, C. Reich, F. Krüger, U. Zeimer, V. Kueller, A. Knauer, C. Netzel, J. Rass, T. Wernicke, M. Weyers, and M. Kneissl. Optically pumped deep UV AlGaN quantum well lasers grown on epitaxially laterally overgrown AlN/sapphire. *International Workshop on Nitride Semiconductors 2014*, 2014, Wroclaw, Poland (poster presentation)

- M. Martens, F. Mehnke, C. Kuhn, C. Reich, U. Zeimer, V. Kueller, A. Knauer, C. Netzel, C. Hartmann, J. Wollweber, J. Rass, T. Wernicke, M. Bickermann, M. Weyers, and M. Kneissl. UV-C AlGaN quantum well lasers grown on sapphire and bulk AlN substrates. *International Conference on Nitride Semiconductors (ICNS-10)*, 2013, Washington DC, USA (oral presentation)

List of samples

Fig. 2.3	TS1637-3, TS1696, TS2669
Fig. 2.4	TS2669
Fig. 2.8(a)	TS2736
Fig. 2.8(b)	TS2736
Fig. 2.9(a)	TS2783-1
Fig. 2.9(b)	TS2783-1
Fig. 2.17(a)	TS4048-2V
Fig. 2.17(b)	TS4048-2V
Fig. 2.18	TS2688
Fig. 2.19	TS2688
Fig. 2.20	TS2688
Fig. 2.21(b)	TS4045-2V
Fig. 2.22(a)	TS4045-2V
Fig. 2.22(b)	TS4045-2V
Fig. 2.24(a)	TS2783-2
Fig. 2.24(b)	TS2783-2
Fig. 2.27(a)	B6180
Fig. 2.27(b)	B6180
Fig. 2.28	B6170
Fig. 3.3(a)	TS1892-2
Fig. 3.3(a)	TS1892-2, TS1908-3, TS1941
Fig. 3.4(a)	TS1908-3
Fig. 3.4(b)	TS1892-2
Fig. 3.5	TS1892-2, TS2167
Fig. 3.7	TS1892-2, TS2167
Fig. 3.9	TS2167, TS2783
Fig. 3.10(a)	TS2783-1
Fig. 3.10(b)	TS3184
Fig. 3.11(a)	TS2669, TS3473
Fig. 3.11(b)	TS2669, TS3473
Fig. 3.12	TS3218-1, TS3620-1

Fig. 3.13	TS4045-2H, TS4048-2H
Fig. 4.1(a)	TS2672, TS2675, TS2783-2, TS2789
Fig. 4.1(b)	TS4061, TS4063, TS4067
Fig. 4.2	TS2669, TS2672, TS2675, TS2684, TS2736, TS2783-2, TS2789, TS2793, TS2800, TS4061, TS4063, TS4067
Fig. 4.3(a)	E4422-11, TS2672
Fig. 4.3(b)	E4422-11, TS2152, TS2672, TS2675, TS2684
Fig. 4.4	E4422-2, E4422-11, TS1892-2, TS2152, TS2167, TS2672, TS2675
Fig. 4.6(a)	TS2669, TS2672, TS2675, TS2684
Fig. 4.6(b)	TS2152, TS2669, TS2672, TS2675, TS2684, TS2688
Fig. 4.7(a)	TS2669, TS2675
Fig. 4.7(b)	TS2669, TS2672, TS2675
Fig. 4.8(a)	TS2691, TS2698
Fig. 4.8(b)	TS2669, TS2691, TS2698, TS2699
Fig. 4.10	TS2669, TS2691, TS2698, TS2699
Fig. 4.11(a)	TS2736, TS2793
Fig. 4.11(b)	TS2736, TS2783-2, TS2789, TS2793
Fig. 4.13	TS2736, TS2783-2, TS2793
Fig. 4.14	E4891-5, E4891-11, E4892-5,E4892-11, E4893-5, E4891-12
Fig. 5.8	TS3418-2, TS3420-2, TS3432-2, TS3426-2
Fig. 5.9(a)	TS2729
Fig. 5.9(b)	TS2729
Fig. 5.10	TS2726, TS2729, TS2737, TS2801, TS2810
Fig. 5.11(a)	TS2726, TS2729, TS2737, TS2801, TS2810
Fig. 5.11(b)	TS2726, TS2729, TS2737, TS2800
Fig. 5.12(b)	TS2737
Fig. 5.13	TS3420-2, TS3418-2, TS3489-2, TS3497-2
Fig. 5.15	TS3559, TS3563, TS3568, TS3571
Fig. 5.16(a)	TS3559, TS3563, TS3568, TS3571
Fig. 5.16(a)	TS3559, TS3563, TS3568, TS3571
Fig. 5.17(a)	TS3571
Fig. 5.17(b)	TS3571
Fig. 5.18	TS3559, TS3563, TS3568, TS3571
Fig. 5.19	TS3559, TS3563, TS3568, TS3571
Fig. 5.20(a)	TS3473, TS3477
Fig. 5.20(a)	TS3473, TS3477